九州大学学術情報リポジトリ
Kyushu University Institutional Repository

Atomic Structures and Chemical States of Active and Inactive Dopant Sites in GaN

湯, 京敏

https://hdl.handle.net/2324/6787572

出版情報：九州大学, 2022, 博士（工学）, 課程博士
バージョン：
権利関係：

Atomic Structures and Chemical States of Active and Inactive Dopant Sites in GaN

TANG JINGMIN

Kyushu University

2022 / 10 / 27

Table of contents

Chapter 1 Introduction 4
1.1 Background......4
1.1.1 General introduction......4
1.1.2 Structures of GaN......6
1.1.3 The preparation methods for GaN 7
1.1.3.1 Metal-organic Chemical Vapor Deposition......7
1.1.3.2 Molecular-beam Epitaxy......8
1.1.3.3 Hydride Vapor Phase Epitaxy......8
1.2 N-and P-type GaN. 9
1.2.1 Dopants for N-type GaN......10
1.2.2 Dopants for P-type GaN......11
1.3 Present issues for Si/Mg-doped GaN......12
1.4 The purpose of the thesis. 13
1.5 Content summary......13
1.6 References......15
Chapter 2 Research Methods 23
2.1 Samples of Si and Mg-doped GaN. 23
2.1.1 Si-doped GaN. 23
2.1.2 Mg-doped GaN......23
2.2 Characterization Methods. 24
2.2.1 X-ray Photoelectron spectroscopy......24
2.2.1.1 PES apparatus in the laboratory. 24
2.2.1.2 Principe of XPS Principle. 25
2.2.1.3 Energy resolution of electron analyzer......27
2.2.1.4. PES apparatus in Synchrotron Radiation Center. 27
2.2.1.5 PES for chemical components and chemical shift detection......29
2.2.1.6 PES for depth profile. 30
2.2.2. Photoelectron diffraction......31
2.2.2.1 Photoelectron hologram......35
2.2.2.2 PEH simulation......38
2.2.3 Auger electron spectroscopy......39
2.2.3.1 Auger transition probability and fluorescence probability......40
2.2.4 X-ray absorption. 40
2.2.4.1 Transmission mode. 42

2.2.4.2 Fluorescence mode. 43
2.2.4.3 Electron yield mode. 44
2.2.4.4 X-ray absorption near-edge structure....45
2.2.4.5 XANES....47
2.2.4.6 XANES measurements....49
2.2.4.6.1 FEFF....49
2.2.5 Secondary-ion mass spectrometry....54
2.2.6 Hall effect measurements....56
2.2.7 Cathodoluminescence....59
2.3 References....60
Chapter 3 Direct Observation of Atomic Structure and Chemical State for Active and inactive Dopant Site in Mg-Doped GaN....67
3.1 Introduction. 67
3.2 Experimental section. 69
3.3 Results and discussion....72
3.4 Conclusion 87
3.5 References. 88
Chapter 4 Atomic Structures and Chemical States of Active and Inactive Dopant Sites in Si-Doped GaN 92
4.1 Introduction....92
4.2 Experimental....94
4.3 Results and discussion....96
4.4 Conclusion....112
4.5 References....113
Chapter 5 Conclusions 118
5.1 Summary of the important conclusions....118
5.2 The outlook of the thesis....119
Supplementary Information 120
S.1 Aichi Synchrotron Radiation Center....120
S.2 Super photon ring 8 GeV (SPring-8) 121
S.3 Reference....124
Acknowledgment 125

Chapter 1 Introduction

1.1 Background

1.1.1 General introduction of GaN

Gallium Nitride (GaN) is highly regarded as a third-generation semiconductor. It has a lot of unique properties, such as wide direct bandgap, high breakdown electric field, radiation resistance, thermal stability, etc.[1-15] Especially since the 1990s, GaN has been well known because it has been used in light-emitting diodes. GaN is also widely used for high-power and high-speed optoelectronic devices.[16-29] In addition, compared with silicon, GaN has the advantages of low switching loss, good heat dissipation, large breakdown field strength, etc. Therefore, GaN has great potential for application in power devices.

	Si	GaAs	4H-SiC	GaN	Diamond	β-Ga_2O_3
Breakdown Electric Field [MV/cm]	0.3	0.4	2.0	3.8	10	8
Thermal conductivity [W/cm. K]	1.5	0.46	3.7	2.5	23	0.13-0.21
Electron saturation velocity [x 10^7 cm/s]	1.0	1.2	2.0	2.7	2.5	2
Energy Bandgap [eV]	1.1	1.4	3.3	3.4	5.5	4.5-4.9
Mobility (cm^2/V. s)	1350	8500	850	1900	2000	300
Relative dielectric constant (ε)	11.8	13.1	10	9.5	5.5	10

Table 1.1: Specific properties of Si, GaAs, SiC, GaN, diamond, and Ga_2O_3.[30-34]

For example, in order to enhance block voltage, semiconductor devices with higher breakdown electric fields are necessary. [33,34] The relationship between the breakdown electric field and block voltage is given by:

$$V_B \approx \frac{\varepsilon.E_C^2}{2.q.N_D} \qquad (1)$$

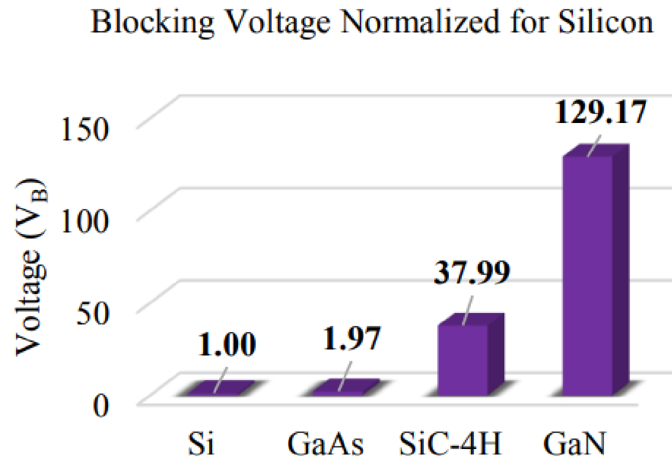

Figure 1.1. Blocking voltage normalized for Si common semiconductors.[34]

where V_B represents breakdown voltage, ε is the dielectric constant, E_C is the breakdown electric field, q stands for electron charge, and N_D is semiconductor material doping density. According to equation 1 and table 1.1, assuming the same doping density of semiconductors, the blocking voltage for commonly used semiconductors materials (Si, GaAs, SiC, and GaN) can be calculated, and the results are shown in Fig. 1.1. As can be seen, GaN has great potential in the field of high-voltage devices. The properties of Si, GaAs, SiC, GaN, diamond, and Ga_2O_3 are summarized in table 1.1.[30-34]

1.1.2 Structures of GaN

GaN has three polytypes: wurtzite, sphalerite and rock salt. In general, the wurtzite structure is the most stable among the polytypes. For the wurtzite structure, the space group is $P6_3mc$, where lattice parameters in the unit cell are a = b = 3.2 Å, c = 5.2 Å; $\alpha = \beta = 90°$, $\gamma = 120°$.[35, 36] The atomic structures of Ga and N-polar GaN are shown in Fig.

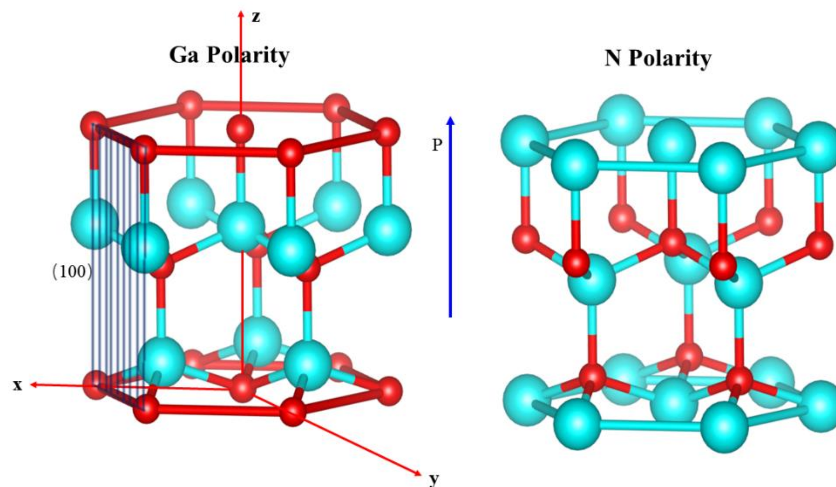

Figure 1.2: The atomic structures of Ga and N polar GaN.

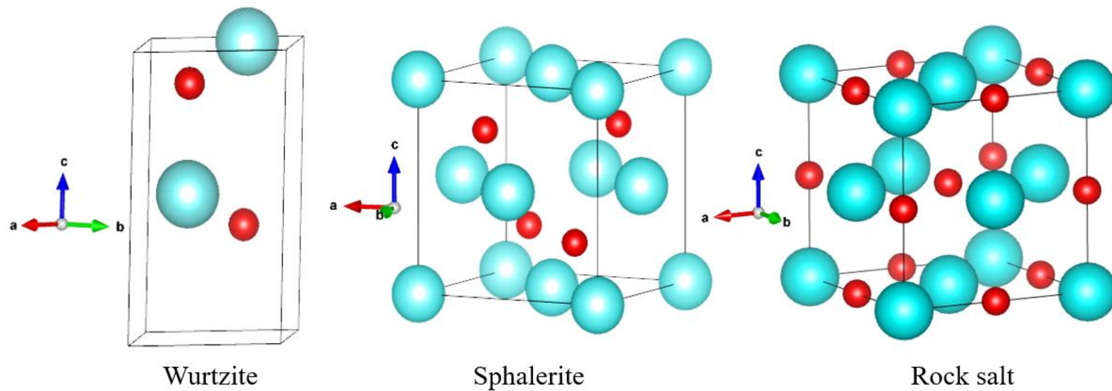

Figure 1.3: GaN unit cells of wurtzite, sphalerite, and rock salt structures.

1.2. [37-40] Two other structures are sphalerite and rock salt. Sphalerite GaN exhibits the space group of $F\bar{4}3m$. The sphalerite structure can convert to the wurtzite structure. [41,42] The rock salt presents a space group of $Fm\bar{3}m$, which can be produced by phase transformation from wurtzite GaN under high pressure. [43-46] Figure 1.3 shows the GaN

unit cells, and table 1.2 presents the GaN lattice parameters.

Table 1.2: The lattice parameters of the unit cells for wurtzite, sphalerite, and rock salt of GaN.[47]

	Space group	Crystal System	a	b	c	α	β	γ
wurtzite	P63mc	hexagonal	3.2Å	3.2Å	5.2Å	60°	60°	120°
sphalerite	$F\bar{4}3m$	cubic	3.2Å	3.2Å	3.2Å	60°	60°	60°
rock salt	$Fm\bar{3}m$	cubic	3.0Å	3.0Å	3.0Å	60°	60°	60°

1.1.3 The usual methods to prepare GaN

In nature, GaN cannot exist as a single crystal. For the preparation of GaN single crystal, metal-organic chemical vapor deposition (MOCVD), molecular-beam epitaxy (MBE), and hydride vapor phase epitaxy (HVPE) methods are usually used.

1.1.3.1 Metal-organic Chemical Vapor Deposition (MOCVD)

For the MOCVD method,[48-55] sapphire is often used as the substrate. Trimethylgallium (TMGa) is usually used as the Ga source while ammonia gas is the nitrogen source. Hydrogen gas (or/and N_2) is utilized as a carrier gas to transport the

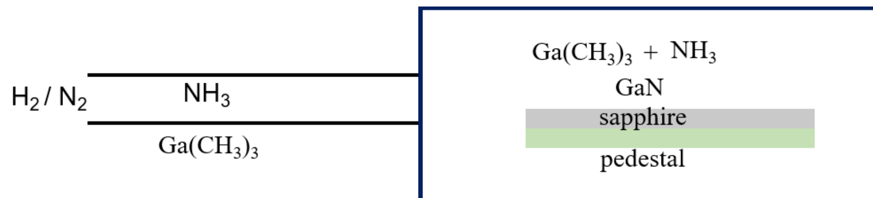

Figure 1.4: GaN growth of MOCVD method.

reactants to a reaction chamber. The temperature in the reactor chamber is set at 1200°C, and GaN single crystal forms on the substrate in the reactor chamber. The advantages of MOCVD are low cost, large-scale growth, easy control, etc. Figure 1.4 shows the schematic of GaN growth by the MOCVD method.

1.1.3.2 Molecular-beam epitaxy (MBE)

For the MBE method, [56-58] metal Ga is working as a Ga source, nitrogen gas is used as the nitrogen source. Sapphire is commonly used as a substrate. The Ga molecular beam and nitrogen gas are sprayed onto the substrate. Then, GaN is formed on the substrate. Compared with the high-temperature reaction of MOCVD (~1200 ℃), MBE has a lower reaction temperature (~700 ℃) to prepare the single crystal. The advantage of the MBE method is not to require an ultra-high reaction temperature.

1.1.3.3 Hydride Vapor Phase Epitaxy (HVPE)

The HVPE method was reported by Maruska and Tietjen in 1969.[59-62] The setup of the HVPE system is simple. For the HVPE method, larger and fairly uniform GaN films can be produced in comparison to other methods. Figure 1.5 shows a schematic of GaN preparation by the HVPE method. HVPE systems include two parts, the left part is the low-temperature region (~800℃), and the right is the high-temperature region (~1000℃). In the case of the low-temperature region, HCl gas is carried by N_2 (or /and H_2) to react with Ga under 800℃, then the generated GaCl is carried to the high-temperature region, and finally, it reacts with NH_3 under 1000 ℃ to form single crystal GaN.

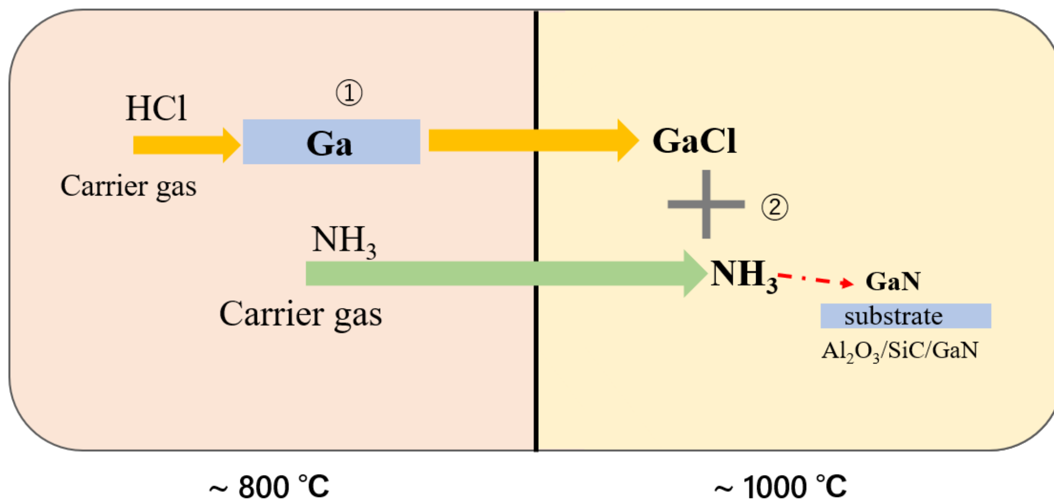

Figure 1.5: GaN growth by the HVPE method.

Generally, sapphire, SiC, and GaN are used as substrates. Sapphire is not expensive, easy to obtain, and has good thermal stability. As a result, sapphire is widely used. However, there are large differences in lattice constant and linear expansion coefficient between sapphire and GaN. These lead to the appearance of defects in GaN, affecting the quality of the GaN crystal. In contrast, SiC and GaN are more suitable as the substrates for the preparation of GaN, because their lattice constants and linear expansion coefficients are similar.

1.2 N-and P-type GaN.

Intrinsic GaN has few carriers for practical applications, thus doping with other elements to increase carriers is crucial. The carrier concentration increases significantly with the amounts of dopants. Donor impurities are necessary to obtain N-type GaN or acceptor impurities are required to form P-type GaN.

1.2.1 Dopants for N-type GaN

For N-type GaN,[63] Si is usually used as the dopant because it can form a shallow donor energy level with ionization energy of ~30 meV.[64,65] There are some common methods used to form Si dopants in GaN. The first one is the MOCVD method.[64, 66-68] It is based on the MOCVD growth of GaN described above, and Si sources (e.g., SiH_4, Si_2H_6) are introduced into the progress of GaN growth. The great advantage of this method is easy to control and this method does not require additional equipment. The second method is pulsed sputtering deposition (PSD).[69-72] This method does not introduce other elements, Therefore, the doped GaN grown by this method has few impurities. The lightly and heavily Si-doped GaN can be prepared by varying Si vapor flux.[70] The third one is physical vapor deposition (PVD). Magnetron sputtering is one of PVD.[73] The input ionized Ar impacts the target of Si, and then the excited Si is positively charged (Si^+).

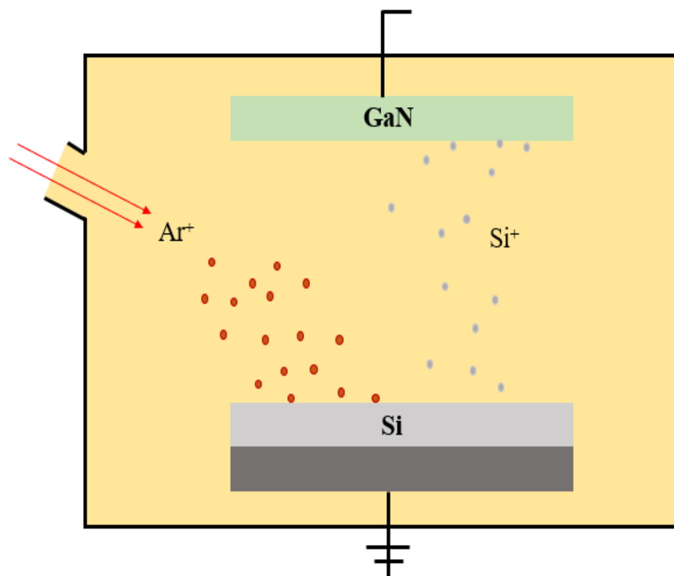

Figure 1.6: Magnetron sputtering method for Si-doped GaN.[73]

Finally, the Si ions are to bombard the Ga substrate, then implant into GaN. Figure 1.6 shows the schematic of magnetron sputtering of Si-doped GaN. The fourth is the HVPE

method.[74-76] As mentioned HVPE method above, the Si source (e.g., SiClx, Dichlorosilane) is introduced during the growth of GaN in the HVPE process. Other methods such as MBE are also used to grow Si-doped GaN.

1.2.2 Dopants for P-type GaN

For P-type GaN, Mg is usually used as the dopant because it can form a shallow

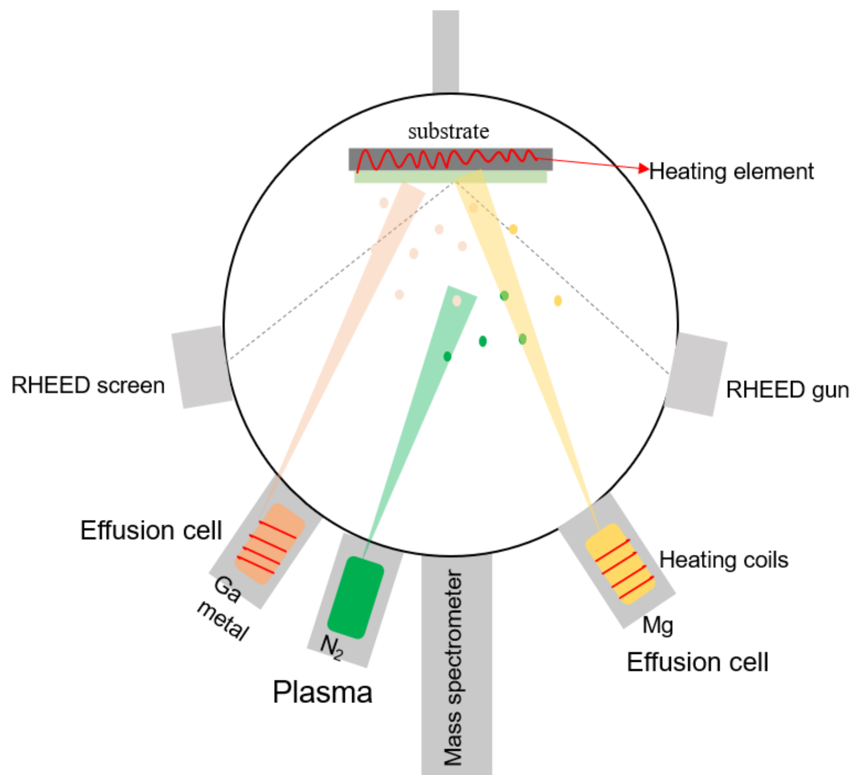

Figure 1.7: MBE method for Mg-doped GaN.

accepter energy level. [77,78] The following are several common doping methods for Mg-doped GaN. The first one is the MOCVD method.[66,79-83] Bis-cyclopentadienyl magnesium (Cp2Mg) is used as an Mg source while trimethylgallium and ammonia are the sources of Ga, and N, respectively. H_2 (or/and N_2) is used as carrier gas. The reaction process is basically similar to that described in chapter 1.2.1. The second one is the MBE

method.[84,85] Solid Mg is used as the dopant source. High-purity Ga metal is used as the source of Ga. The schematic of MBE is shown in Fig. 1.7. The third is PSD, [86,87] this method can largely eliminate the doping of hydrogen atoms. The fourth one is the HVBE method,[88-91] where Mg/MgO/ Cp2Mg is used as the source of Mg dopant source, and HCl and NH_3 are worked as gaseous reagents. This method is simple and effective for the preparation of Mg-doped GaN.

1.3 Present issues for Si/Mg-doped GaN

For GaN-based devices, Si and Mg are commonly used as n-type and p-type dopants, respectively. These dopants are mainly ascribed to the shallow dopant property. However, the carrier concentration is much lower than the number of dopants. According to previous studies, the carrier concentration is about a few orders of magnitude less than the dopant concentration. [75,92] In spite of many studies on dopants in GaN, there are few methods directly to investigate the atomic structures and chemical states of dopants in GaN. Kumar et al. investigated chemical states and atomic structures in dopants for Mg-doped GaN using scanning transmission electron microscopy and atom probe tomography.[93] Renault et al. investigated atomic structures and chemical states of dopants for Si-doped GaN using X-ray photoelectron spectroscopy and scanning Auger microscopy.[94] However, they could not clarify atomic structures and chemical states in active sites of the dopants. Thus, one requires a method that probes the chemical states and atomic structures of the active and inactive dopants in GaN. In addition, to gain knowledge about the carrier control in metal−oxide−semiconductor field effect transistors, it is crucial to clarify the atomic structures and the chemical states of the active and inactive dopant sites in GaN.

1.4 The purpose of the thesis.

The purpose of this thesis is to clarify the atomic structures and chemical states of active and inactive dopant states of Si / Mg-doped GaN. Once the atomic structures and chemical states of active and inactive dopant states are clarified, it is possible to suggest fabrication methods to reduce and vanish inactive dopant states. For the purpose of the present thesis, Auger electron spectroscopy (AES), photoelectron spectroscopy (PES), X-ray absorption near-edge structure (XANES), and photoelectron holography (PEH) were employed to clarify the atomic structures and chemical states of active and inactive dopant states of Si / Mg-doped GaN.

1.5 Content summary

Chapter 1 introduces the introduction and general background of GaN, the preparation method of GaN, and the preparation method of N and P-type GaN. Chapter 1 also includes issues that should be solved and the purpose of this doctoral thesis.

Chapter 2 presents the sample preparation methods and experimental procedures used in the present thesis. The principle of the characterization methods (PES, AES, XANES, PEH, etc) used in the present thesis is also explained.

Chapter 3 describes the results on the use of chemical state-discriminated PEH, PES, and AES to clarify the local atomic structures and the chemical states of active and inactive dopant states for Mg dopants in Mg-doped GaN.

Chapter 4 presents the clarification of the atomic structures and chemical states of active and inactive dopant sites in Si-doped GaN using XANES and the XANES simulations.

Chapter 5 describes the conclusions and the outlook of the thesis. The conclusions

subchapter summarizes the most important results.

The supplementary chapter is included in this thesis. The chapter describes the beamlines of Aichi synchrotron radiation and SPring-8.

1.6 References

1. Pankove, J. I. *Materials Science and Engineering: B*. *61*, 305-309 (1999).

2. Morkoc, B. H., Strite, S., Gao, G. B., Lin, M. E., Sverdlov, B., & Burns, M. *Journal of Applied physics*. *76*, 1363-1398 (1994).

3. Kawashima, T., Yoshikawa, H., Adachi, S., Fuke, S., & Ohtsuka, K. *Journal of applied physics*. *82*, 3528-3535 (1997).

4. Manna, S., Ashok, V. D., & De, S. K. *ACS Applied Materials & Interfaces*. 2, 3539-3543(2010).

5. Mohammad, S. N., Salvador, A. A., & Morkoc, H. *Proceedings of the IEEE*. 83, 1306-1355 (1995).

6. Pearton, S. J., Zolper, J. C., Shul, R. J., & Ren, F. *Journal of applied physics*. 86, 1-78 (1999).

7. Huang, X., Liu, Z., Li, Q., & Lee, F. C. *IEEE Transactions on Power Electronics*. 29, 2453-2461 (2013).

8. Leszczynski, M., Teisseyre, H., Suski, T., Grzegory, I., Bockowski, M., Jun, J., Porowski, S., Pakula, K., Baranowski, J. M., Foxon, C. T., & Cheng, T. S. *Applied Physics Letters*, 69, 73-75(1996).

9. Pearton, S. J., Ren, F., Zhang, A. P., Dang, G., Cao, X. A., Lee, K. P., Cho, H., Gila, B. P., Johnson, J. W., Monier, C., Abernathy, C. R., Han, J., Baca, A. G., Chyi, J.-I., Lee, C.-M., Nee, T.-E., Chuo, C.-C., & Chu, S. N. G. *Materials Science and Engineering: B*. 82, 227-231 (2001).

10. Liu, L., & Edgar, J. H. *Materials Science and Engineering: R: Reports*. 37, 61-127 (2002).

11. Cheng, Z. J.; Chen, X. Y.; San, H. S.; Feng, Z. H.; Liu, B. J. Micromech. Microeng.

2012, 22, 074011−074016.

12. Margalith, T., Buchinsky, O., Cohen, D. A., Abare, A. C., Hansen, M., DenBaars, S. P., & Coldren, L. A. *Applied Physics Letters*. 74, 3930-3932 (1999).

13. Krost, A., & Dadgar, A. *Materials Science and Engineering: B*. 93, 77-84 (2002).

14. Arakawa, Y., Ueno, K., Imabeppu, H., Kobayashi, A., Ohta, J., & Fujioka, H. *Applied Physics Letters*. 110, 042103 (2017).

15. Margalith, T., Buchinsky, O., Cohen, D. A., Abare, A. C., Hansen, M., DenBaars, S. P., & Coldren, L. A. *Applied Physics Letters*. 74, 3930-3932 (1999).

16. Yan, Z., Liu, G., Khan, J. M., & Balandin, A. A. *Nature communications*. 3, 1-8 (2012).

17. Mashiko, H., Oguri, K., Yamaguchi, T., Suda, A., & Gotoh, H. *Nature physics*, 12, 741-745 (2016).

18. Meneghini, M., Trevisanello, L. R., Meneghesso, G., & Zanoni, E. *IEEE Transactions on Device and Materials Reliability*. 8, 323-331 (2008).

19. Chung, K., Lee, C. H., & Yi, G. C. *Science*. 330, 655-657 (2010).

20. Davis, R. F. *Proceedings of the IEEE*. 79, 702-712 (1991).

21. Denbaars, S. P. *Proceedings of the IEEE.* 85, 1740-1749 (1997).

22. Zhou, S., Liu, X., Yan, H., Chen, Z., Liu, Y., & Liu, S. *Optics express*. *27*, A669-A692 (2019).

23. Tojyo, T., Asano, T., Takeya, M., Hino, T., Kijima, S., Goto, S., Uchida, S., & Ikeda, M. *Japanese Journal of Applied Physics*. *40*, 3206 (2001).

24. Shur, M. S. *Solid-State Electronics*. 42, 2131-2138 (1998).

25. Liao, C. L., Chang, Y. F., Ho, C. L., & Wu, M. C. *IEEE Electron Device Letters*. 34, 611-613 (2013).

26. Ujita, S., Kinoshita, Y., Umeda, H., Morita, T., Tamura, S., Ishida, M., & Ueda, T. In *2014 IEEE 26th International Symposium on Power Semiconductor Devices & IC's (ISPSD)* (pp. 51-54). IEEE (2014, June).

27. Jones, E. A., Wang, F., & Ozpineci, B. In *2014 IEEE Workshop on Wide Bandgap Power Devices and Applications* (pp. 24-29). IEEE (2014, October).

28. Huang, X., Liu, Z., Li, Q., & Lee, F. C. *IEEE Transactions on Power Electronics*. 29, 2453-2461 (2013).

29. Ohno, Y., & Kuzuhara, M. *IEEE Transactions on Electron Devices*. 48, 517-523 (2001).

30. 東脇正高，佐々木公平，倉又朗人，増井建和，山腰茂伸，"酸化ガリウムパワーデバイスの研究開発"，第 27 回フジサンケイビジネスアイ 先端技術大賞 特別賞，2013 年 7 月 **http://www.fbi-award.jp/sentan/jusyou/2013/10.pdf**

31. Chow, T. P., Omura, I., Higashiwaki, M., Kawarada, H., & Pala, V. *IEEE Transactions on Electron Devices*, *64*(3), 856-873 (2017).

32. Sun, Y., Kang, X., Zheng, Y., Lu, J., Tian, X., Wei, K., ... & Zhang, G. *Electronics*, *8*(5), 575 (2019).

33. Zhang, Y. In *IOP Conference Series: Materials Science and Engineering* (Vol. 738, No. 1, p. 012004). IOP Publishing (2020).

34. Mengatto, A., Diesel,J. A. D. P., de França H. T. and Heerdt, J. A. *2019 IEEE 15th Brazilian Power Electronics Conference and 5th IEEE Southern Power Electronics Conference (COBEP/SPEC)*, 2019, pp. 1-6.3.

35. Schulz, H., & Thiemann, K. H. *Solid State Communications*. 23, 815-819 (1977).

36. Lagerstedt, O., & Monemar, B. *Physical Review B*. 19, 3064 (1979).

37. Sumiya, M., & Fuke, S. *Materials Research Society Internet Journal of Nitride Semiconductor Research*. 9, (2004).

38. Keller, S., Li, H., Laurent, M., Hu, Y., Pfaff, N., Lu, J., Brown, D. F., Fichtenbaum, N. A., Speck, J. S., DenBaars, S. P., & Mishra, U. K. *Semiconductor Science and Technology*. 29, 113001(2014).

39. Hellman, E. S. *Materials Research Society Internet Journal of Nitride Semiconductor Research*. *3* (1998).

40. Arbouche, O., Belgoumène, B., Soudini, B., & Driz, M. *Computational Materials Science*. 47, 432-438 (2009).

41. Vennegues, P., Beaumont, B., Vaille, M., & Gibart, P. *Journal of crystal growth*. 173, 249-259 (1997).

42. Degave, F., Ruterana, P., Nouet, G., Je, J. H., & Kim, C. C. *Materials Science and Engineering: B*. *93*(1-3), 177-180 (2002).

43. Xia, H., Xia, Q., & Ruoff, A. L. *Physical Review B*. *47*(19), 12925 (1993).

44. Limpijumnong, S., & Lambrecht, W. R. *Physical review letters*. *86*(1), 91(2001).

45. Xiao, H. Y., Gao, F., Wang, L. M., Zu, X. T., Zhang, Y., & Weber, W. J. *Applied Physics Letters*, *92*(24). 241909 (2008).

46. Halsall, M. P., Harmer, P., Parbrook, P. J., & Henley, S. J. (2004). *Physical Review B*, *69*(23), 235207.

47. https://materialsproject.org/.

48. Weyher, J. L., Brown, P. D., Zauner, A. R. A., Müller, S., Boothroyd, C. B., Foord, D. T., Hageman, P. R., Humphreys, C.J., Larsen, P. K., Grzegory, I., & Porowski, S. *Journal of crystal growth*. 204, 419-428 (1999).

49. Wickenden, A. E., Koleske, D. D., Henry, R. L., Twigg, M. E., & Fatemi,

M. *Journal of crystal growth*. 260, 54-62 (2004).

50. Ishikawa, H., Shimanaka, K., Tokura, F., Hayashi, Y., Hara, Y., & Nakanishi, M. *Journal of Crystal Growth*. 310, 4900-4903 (2008).

51. Nakamura, S., Harada, Y., & Seno, M. *Applied physics letters*. 58, 2021-2023 (1991).

52. Porowski, S. *Materials Science and Engineering: B*. 44, 407-413 (1997).

53. Marchand, H., Ibbetson, J. P., Fini, P. T., Kozodoy, P., Keller, S., DenBaars, S., Speck, J. S., & Mishra, U. K. *Materials Research Society Internet Journal of Nitride Semiconductor Research*. 3 (1998).

54. Wickenden, D. K., Kistenmacher, T. J., Bryden, W. A., Morgan, J. S., & Wickenden, A. E. *MRS Online Proceedings Library (OPL)*, *221*(1991).

55. Xu, K., Xu, J., Deng, P., Qiu, R., & Fang, Z. *physica status solidi (a)*. 176, 589-593 (1999).

56. Moustakas, T. D., Lei, T., & Molnar, R. J. *Physica B: Condensed Matter*, *185*, 36-49 (1993).

57. Okumura, H., Balakrishnan, K., Hamaguchi, H., Koizumi, T., Chichibu, S., Nakanishi, H., ... & Yoshida, S. *Journal of crystal growth*, *189*, 364-369 (1998).

58. Hughes, W. C., Rowland Jr, W. H., Johnson, M. A. L., Fujita, S., Cook Jr, J. W., Schetzina, J. F., ... & Edmond, J. A. *Journal of Vacuum Science & Technology B: Microelectronics and Nanometer Structures Processing, Measurement, and Phenomena*, *13*(4), 1571-1577(1995).

59. Maruska, H. P., & Tietjen, J. J. *Applied Physics Letters*. *15*, 327-329 (1969).

60. Fujito, K., Kubo, S., Nagaoka, H., Mochizuki, T., Namita, H., & Nagao, S. *Journal of Crystal Growth*. *311*, 3011-3014 (2009).

61. Fujito, K., Kiyomi, K., Mochizuki, T., Oota, H., Namita, H., Nagao, S., & Fujimura, I. *physica status solidi (a)*. *205*, 1056-1059 (2008).

62. Fujito, K., Kubo, S., & Fujimura, I. *MRS bulletin*. 34, 313-317 (2009).

63. Nakamura, S., Mukai, T. M. T., & Senoh, M. S. M. *Japanese Journal of Applied Physics*. 31, 2883 (1992).

64. Halidou, I.; Benzarti, Z.; Chine, Z.; Boufaden, T.; El Jani, B. *Microelectron. J.* 32, 137−142 (2001).

65. Irokawa, Y.; Fujishima, O.; Kachi, T.; Nakano, Y. *J. Appl. Phys.* 97, 083505 (2005).

66. Ramaiah, K. S., Su, Y. K., Chang, S. J., Juang, F. S., & Chen, C. H. *Journal of crystal growth*. *220*, 405-412 (2000).

67. Li, S., Mo, C., Wang, L., Xiong, C., Peng, X., Jiang, F., ... & Gong, D. *Journal of luminescence*. 93, 321-326 (2001).

68. Li, D., Ma, B., Miyagawa, R., Hu, W., Narukawa, M., Miyake, H., & Hiramatsu, K. *Journal of crystal growth*. 311, 2906-2909 (2009).

69. Ueno, K., Taiga, F., Kobayashi, A., & Fujioka, H. *Scientific Reports*, *9*(1), 1-5 (2019).

70. Arakawa, Y., Ueno, K., Imabeppu, H., Kobayashi, A., Ohta, J., & Fujioka, H. *Applied Physics Letters*. 110, 042103 (2017).

71. Fudetani, T., Ueno, K., Kobayashi, A., & Fujioka, H. *Applied Physics Letters*. 118, 072101(2021).

72. Ueno, K., Fudetani, T., Arakawa, Y., Kobayashi, A., Ohta, J., & Fujioka, H. *APL Materials*. 5, 126102 (2017).

73. Mantarcı, A., & Kundakçi, M. *Journal of the Australian Ceramic Society*, *56*(3), 905-914 (2020); Shi, F. In *Magnetron Sputtering*. IntechOpen (2018).

74. Fomin, A. V., Nikolaev, A. E., Nikitina, I. P., Zubrilov, A. S., Mynbaeva, M. G., Kuznetsov, N. I., Kovarsky, A. P., Ber, B. Ja., & Tsvetkov, D. V. *physica status solidi (a)*. 188, 433-437 (2001).

75. Iwinska, M., Sochacki, T., Amilusik, M., Kempisty, P., Lucznik, B., Fijalkowski, M., Litwin-Staszewska, E., Smalc-Koziorowska, J., Khapuridze, A., Staszczak, G., Grzegory, I., & Bockowski, M. *Journal of Crystal Growth*, *456*, 91-96 (2016).

76. Richter, E., Stoica, T., Zeimer, U., Netzel, C., Weyers, M., & Tränkle, G. *Journal of electronic materials*. 42, 820-825 (2013).

77. Reshchikov, M. A., Ghimire, P., & Demchenko, D. O. *Physical Review B*, *97*(20), 205204 (2018).

78. Götz, W., Johnson, N. M., & Bour, D. P. *Applied Physics Letters*, *68*(24), 3470-3472. (1996).

79. Ohba, Y., & Hatano, A. *Journal of Crystal growth*. *145*, 214-218 (1994).

80. Obloh, H., Bachem, K. H., Kaufmann, U., Kunzer, M., Maier, M., Ramakrishnan, A., & Schlotter, P. *Journal of crystal growth*. *195*, 270-273 (1998).

81. Kozodoy, P., Keller, S., DenBaars, S. P., & Mishra, U. K. *Journal of crystal growth*.195, 265-269 (1998).

82. Amano, H., Kitoh, M., Hiramatsu, K., & Akasaki, I. *Journal of the Electrochemical Society*. 137, 1639 (1990).

83. Kozodoy, P., Xing, H., DenBaars, S. P., Mishra, U. K., Saxler, A., Perrin, R., Elhamri, S., & Mitchel, W. C. Heavy doping effects in Mg-doped GaN. *Journal of Applied Physics*. 87, 1832-1835 (2000).

84. Smorchkova, I. P., Haus, E., Heying, B., Kozodoy, P., Fini, P., Ibbetson, J. P., ... & Mishra, U. K. *Applied Physics Letters*, *76*(6), 718-720 (2000).

85. Dussaigne, A., Damilano, B., Brault, J., Massies, J., Feltin, E., & Grandjean, N. *Journal of Applied Physics*. *103*, 013110 (2008).

86. Arakawa, Y., Ueno, K., Kobayashi, A., Ohta, J., & Fujioka, H. *APL Materials*. 4, 086103 (2016).

87. Narita, T., Kachi, T., Kataoka, K., & Uesugi, T. *Applied Physics Express*. 10, 016501 (2016).

88. Usikov, A., Kovalenkov, O., Ivantsov, V., Sukhoveev, V., Dmitriev, V., Shmidt, N., Poloskin, D., Petrov, V., & Ratnikov, V. *MRS Online Proceedings Library*. *831*, 637-641(2004).

89. Kimura, T., Ohnishi, K., Amano, Y., Fujimoto, N., Araidai, M., Nitta, S., ... & Shiraishi, K. *Japanese Journal of Applied Physics*. 59, 088001(2020).

90. Monemar, B., Paskov, P. P., Bergman, J. P., Paskova, T., Figge, S., Dennemarck, J., & Hommel, D. *physica status solidi (b)*, *243*(7), 1604-1608) (2006).

91. Usikov, A., Soukhoveev, V., Kovalenkov, O., Syrkin, A., Shapovalov, L., Volkova, A., & Ivantsov, V. *Japanese Journal of Applied Physics*, *52*(8S), 08JB22 (2013).

92. Romano, L. T., Kneissl, M., Northrup, J. E., Van de Walle, C. G., & Treat, D. W. *Applied Physics Letters*, *79*(17), 2734-2736 (2001).

93. Kumar, A., Uzuhashi, J., Ohkubo, T., Tanaka, R., Takashima, S., Edo, M., & Hono, K. (2019). *Journal of Applied Physics*, *126*(23), 235704.

94. Renault, O., Morin, J., Tchoulfian, P., Chevalier, N., Feyer, V., Pernot, J., & Schneider, C. M. (2015). *Ultramicroscopy*, *159*, 476-481.

Chapter 2 Research methods.

2.1 Samples of Si and Mg-doped GaN.

2.1.1 Si-doped GaN.

Si-doped GaN (0001) substrates were prepared by the HVPE method,[1-3] which were made by the ETA research company. The typical schematic diagram of the reaction is shown in Fig. 2.1. The sample preparation consists of the source and the deposition zones. The temperature of the source zone was 700 to 900 °C, and the temperature in the deposition zone was around 1000 °C.

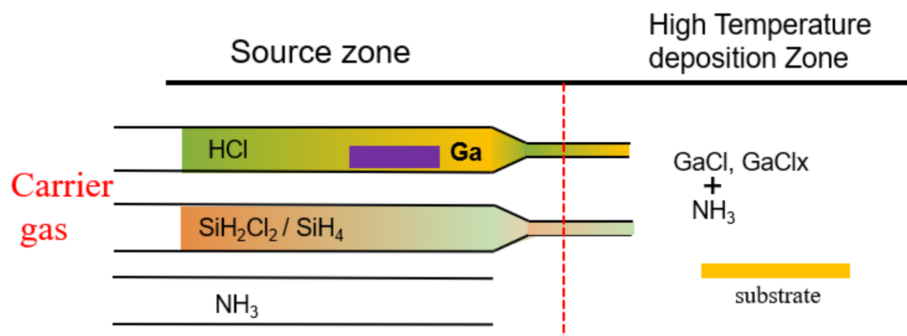

Figure 2.1: Preparation of Si-doped GaN by HVPE.

2.1.2 Mg-doped GaN.

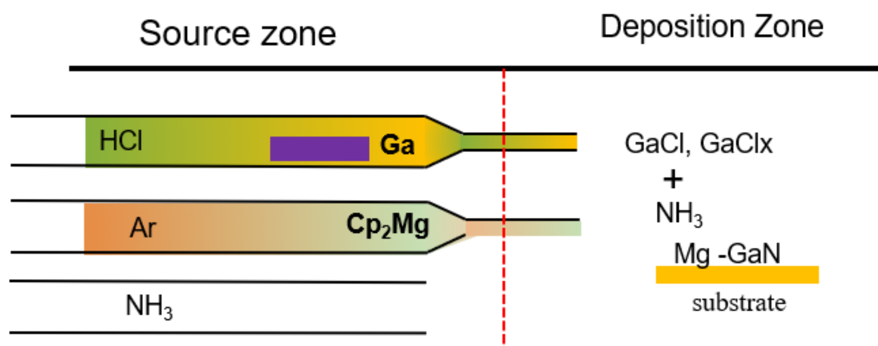

Figure 2.2: Preparation of Mg-doped GaN by HVPE.

The samples of Mg-doped GaN were also purchased from the ETA research company. The Mg-doped GaN (0001) was prepared by the HVPE method,[3] which is shown in Fig. 2.2.

2. 2 Characterization Methods.

2.2.1 X-ray Photoelectron spectroscopy (XPS).

2.2.1.1 XPS apparatus in the laboratory.

XPS was first developed by K. Siegbahn in the early1960s. Since the qualitative analysis of chemical elements is possible using XPS, it is known as electron spectroscopy for chemical analysis (ESCA).[4-8] From the initial qualitative analysis of chemical

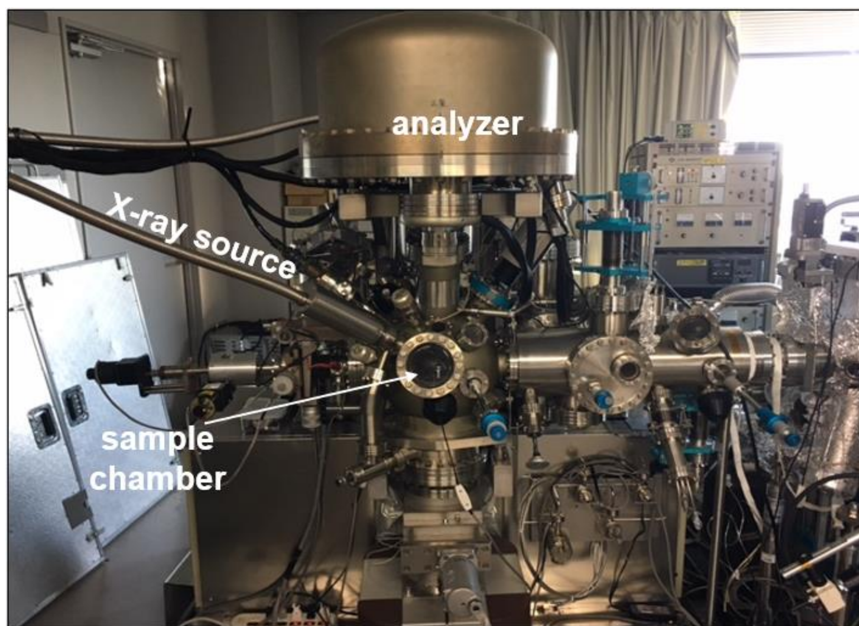

Figure 2.3: XPS apparatus in laboratory.

elements, it has become a vital analysis tool for the qualitative analysis of elements, chemical states, and depth distribution. XPS apparatus mainly consists of three parts: an X-ray source, an ultra-high vacuum chamber, and an electron energy analyzer, which is shown in Fig. 2.3. The typical X-ray sources are Al Kα and Mg Kα, whose energies are 1486 and 1253 eV, respectively.

2.2.1.2 Principe of XPS Principle.

X-rays excite the inner electrons of materials, and thus the excited electrons are called as photoelectrons. When the photon energy of the X-ray is greater than the binding energy (BE) + work function, photoelectrons are excited. The process is shown in Fig.

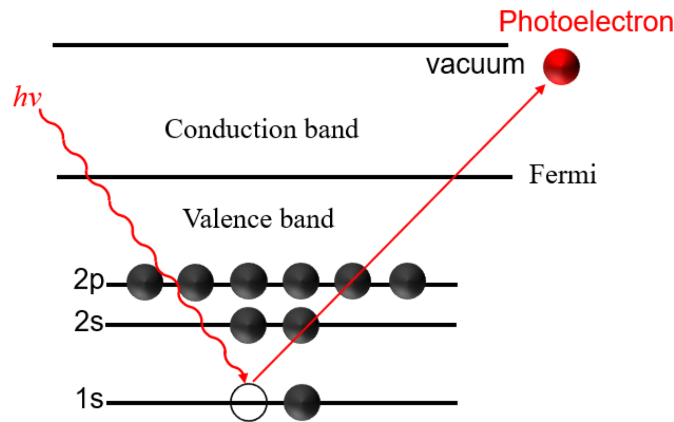

Figure 2.4: Photoelectron excitation process.

2.4. Applying Einstein's photoelectric equation, kinetic energy (KE) and Eb of the emitted photoelectrons can be given by following:

$$E_b = h\nu - E_k - W. \quad h\nu > E_b + W \tag{3}$$

where E_b is BE of electrons, E_k is the kinetic energy of photoelectrons, hv represents photon energy, and W is the work function.[9-12] The energy levels are shown in Fig. 2.5.

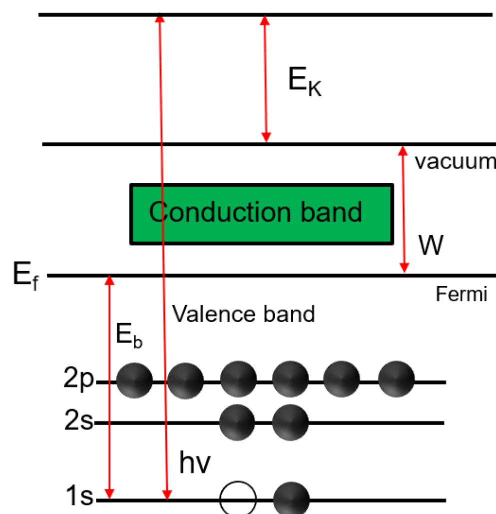

Figure 2.5: Energy level of photoelectron excitation process.

Hemispherical electron energy analyzer (HEA) and cylindrical mirror analyzer are usually used as electron analyzers. HEA is shown in Fig. 2.6, and the principle of HEA is

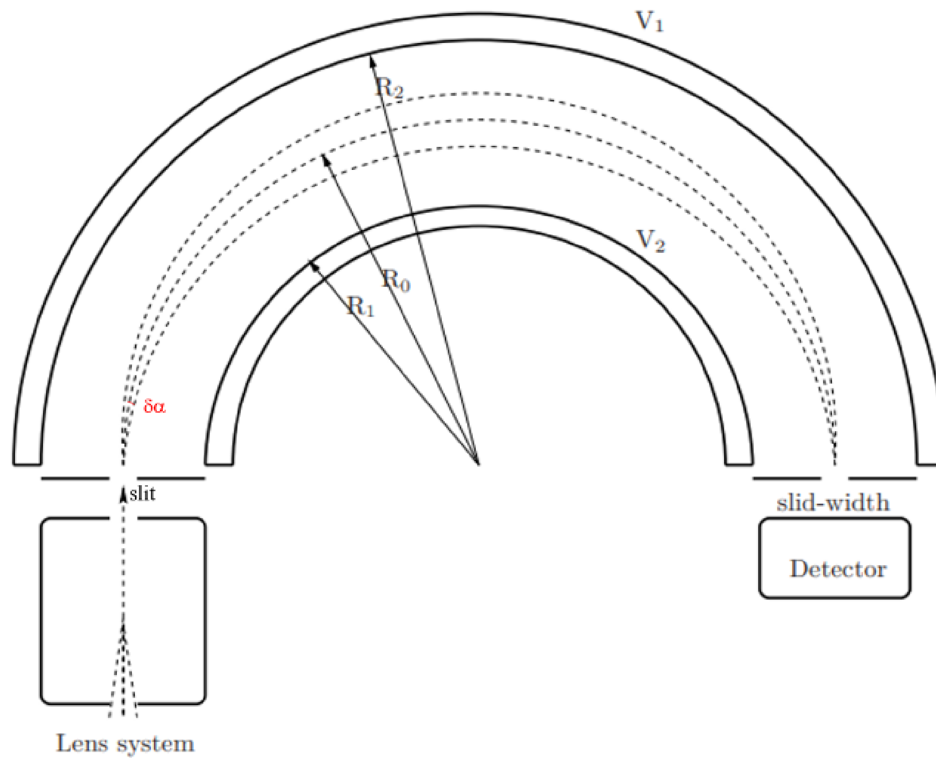

Figure 2.6: Hemispherical electron energy analyzer. [13]

explained as follows: photoelectrons are slowed down at the entrance slit using the electrostatic lens. In order to pass photoelectrons through the HEA, [13] the negative voltage is used ($V_2 < V_1$). For the middle radius R_0, the potential V_0 is as follows:

$$V_0 = (V_2 R_2 + V_1 R_1) / 2 R_0 \tag{4}$$

where R_1 and R_2 are the respective inner and outer radius, R_0 is the average radius. By changing V_1 and V_2, the photoelectrons with the corresponding kinetic energy with eV_0 travel to the detector. Finally, the kinetic energies of the photoelectrons are analyzed. Because the detected electrons are very weak, electron multipliers are often used to amplify the gain.

2.2.1.3 Energy resolution of electron analyzer.

The energy resolution is an important parameter for chemical analysis. The small energy resolution indicates a smaller distinguishable energy difference. The energy resolution of the analyzer, ΔE, is expressed by the following formula.

$$\Delta E = E_p \left(\frac{W}{2R} + \frac{\alpha^2}{2}\right) \quad (5)$$

W is the slit width, R is the mean radius of the analyzer, E_p is the pass energy, and the acceptance angle of α at the entrance slit.[14] It can be seen from the above equation that reducing the pass energy, reducing the slit width, reducing the acceptance angle, and increasing the radius of the analyzer are effective for obtaining higher energy resolution.

2.2.1.4. PES apparatus in Synchrotron Radiation Center.

Electromagnetic radiation is emitted when an electron cluster accelerated to close to the speed of light moves along an arc-shaped orbit in a magnetic field, as shown in Fig. 2.7.[15-19] It was first observed in the synchrotron, so it is called synchrotron radiation (SR). Compared to laboratory X-ray sources, SR source has advantages such as extremely high brightness, wide wavelength, etc. The light irradiated from the SR is a continuous

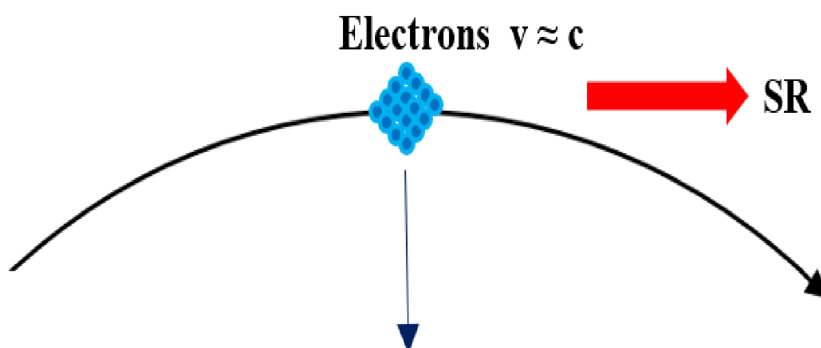

Figure 2.7: Principle of X-ray generation at SR center.

spectrum from far infrared to hard X-rays. According to the experimental needs,

monochromators are used to adjust wavelengths based on the Bragg equation [20,21]:

$$2d \sin \theta = n \lambda \quad , n=1, 2, 3\ldots\ldots \tag{6}$$

The monochromatic photon energy one wants can be obtained by adjusting the angle of the monochromator. [22,23]

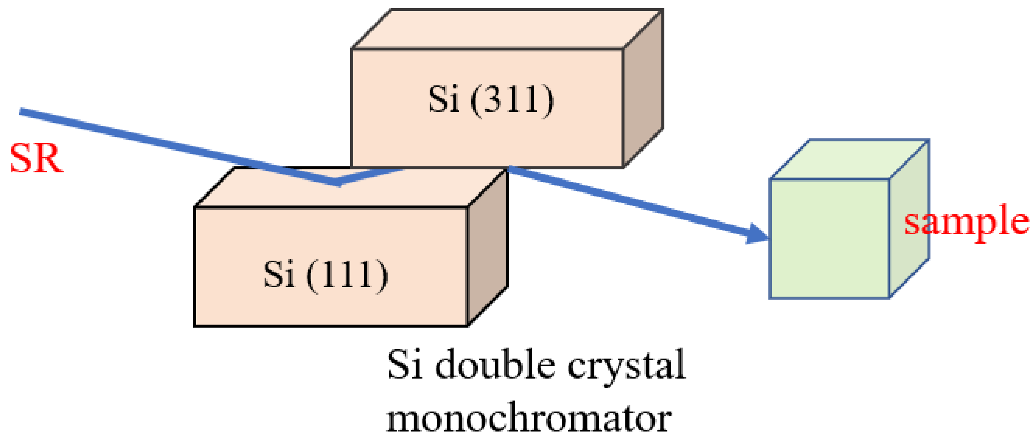

Figure 2.8: Monochromator of Si double crystal.

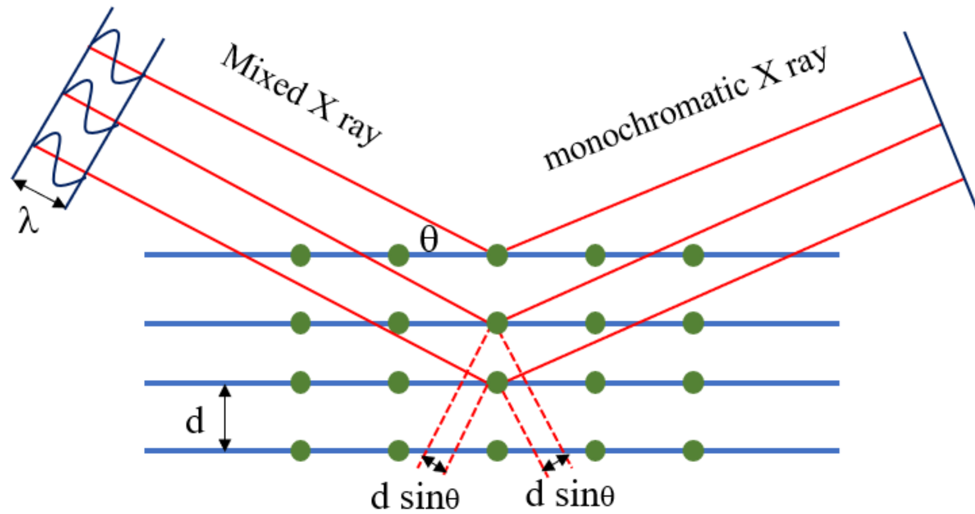

Figure 2.9: Bragg condition.

2.2.1.5 XPS for chemical analysis.

As shown in Fig. 2.10 (a), the XPS survey spectrum of GaN shows many peaks, which is corresponding to Ga, N, C, Al, and O. Figure 2.10 (b) shows the spectra of Ga 3d. There are several peaks in which the energy difference is based on different chemical states. The energy shift is called as a chemical shift.

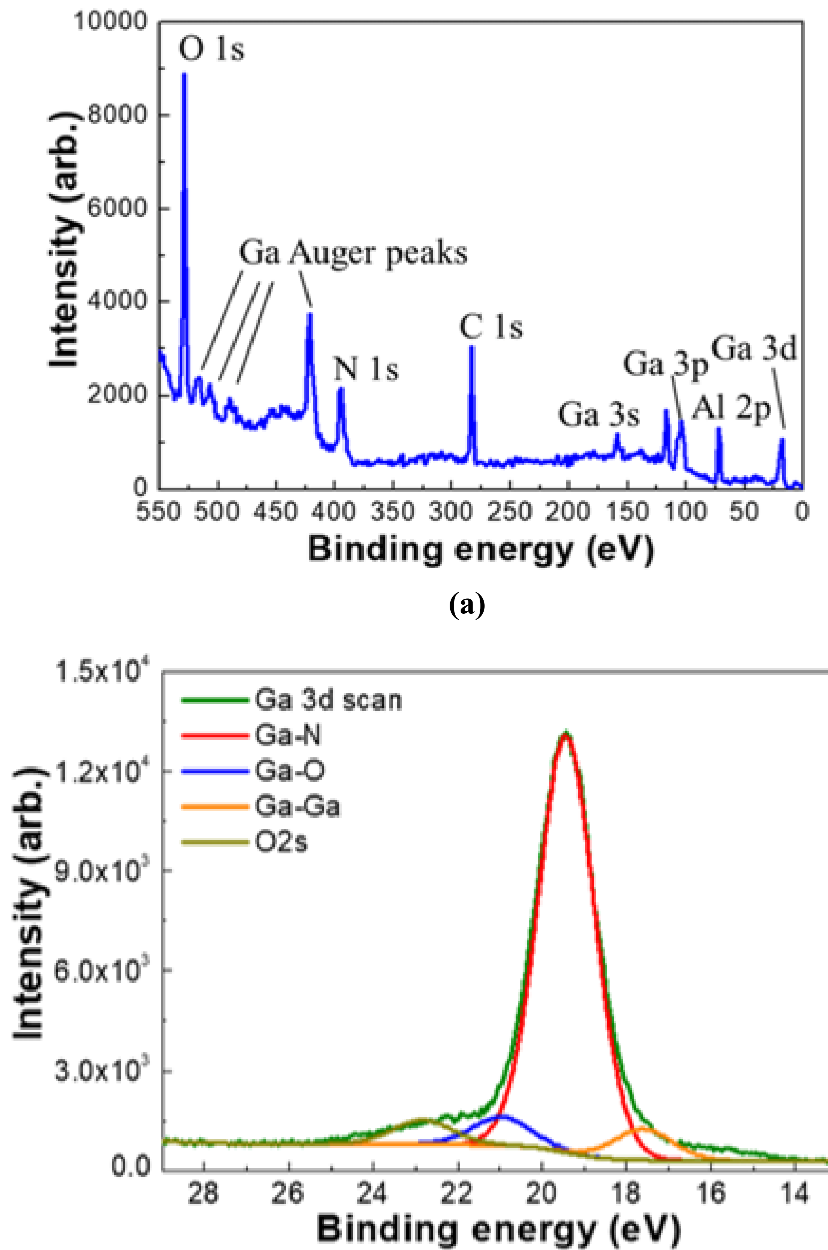

Figure 2.10: (a) survey XPS spectrum of GaN; (b) Ga 3d core level spectrum of GaN.[24]

2.2.1.6 XPS for depth profile.

XPS can be also used to obtain the chemical states of materials at different depths, according to the different kinetic energy of photoelectrons and electron detection angle at

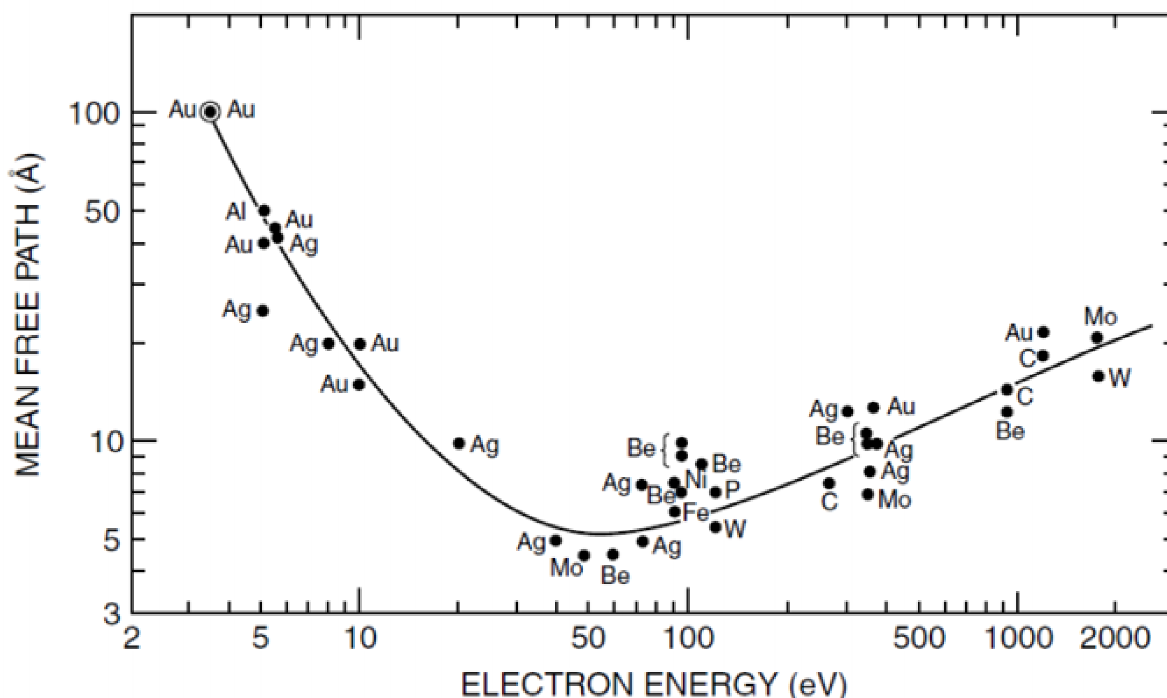

Figure 2.11: IMFPs of electron energy. [25]

the surface of the samples. Figure 2.11 shows the inelastic mean free path (IMFP) as a function of electron energy. IMFP exhibits a minimum for electrons of around 50 -100 eV because the energy loss of electrons occurs by plasmon.[26] The relationship between electron energy and IMFP can be described by the following semi-empirical formula [25]:

$$\lambda = \frac{538a}{E^2} + 0.41a^{3/2}(\text{elements});$$

$$\lambda = \frac{2170a}{E^2} + 0.72a^{3/2}E^{1/2} \;\; (\text{Inorganic compounds}). \qquad (7)$$

where a is the monolayer thickness.

The TPP-2M formula developed by Tanuma et al. is now widely used to calculate IMFP.[27] Information depth is defined as three times of the IMFP (d =3 λ, d is information depth) with the percentage of detected electrons is 95%. According to the Beer-Lambert

law, the intensity I_0 (at the surface) and the intensity I (at depth of d) are described as the following equation:

$$I_0 = I\ e^{-d/\lambda} \quad , \tag{8}$$

As shown in Fig. 2.12, the intensities of 1λ, 2λ, and 3λ exhibit 37, 14, and 5% of I_0, respectively.

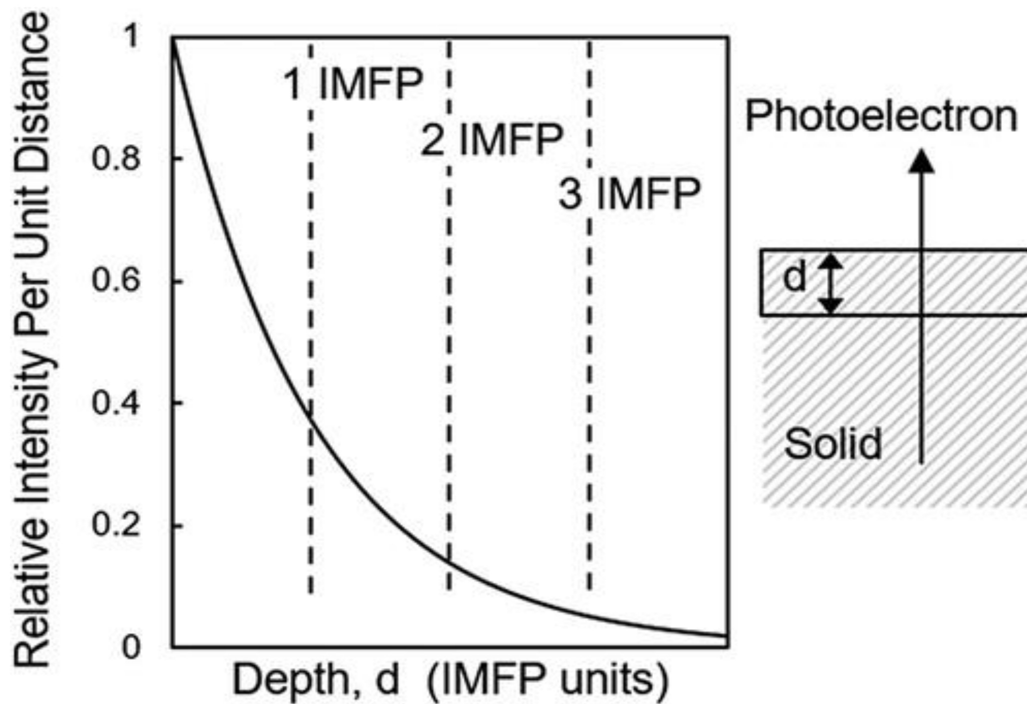

Figure 2.12: IMFP as a function of information depth. [28]

2.2.2. Photoelectron diffraction (PED).

Siegbahn et al. observed clear photoelectron diffraction on single-crystal surfaces in 1970. [29] After decades of experimental and theoretical developments, PED has become a powerful method in the fields of adsorption surfaces, doped structures, epitaxial surfaces, etc. PED principle is explained as follows [30,31]: the electrons of the atoms are excited to form photoelectrons, and then the photoelectron waves are scattered by surrounding atoms in the process of propagation. After that, the original photoelectron waves and the

scattered photoelectron waves interfere to form patterns with modulated intensity. By analyzing the photoelectron intensity as a function of emission angle, or different photoelectron energies, PED patterns can be obtained. Since PED is based on PES, PED is a chemical state-specific method, which is very useful for the atomic structure of adsorption surfaces, doped structures, epitaxial surfaces, etc. The diffraction patterns formed by PED reflect the local atomic structures around the excited atoms because the IMFP of the excited photoelectrons exhibits a few nanometers.

For photoelectrons with kinetic energy less than 500 eV, multi-scattering, forward scattering, and backscattering are dominant. For photoelectrons with kinetic energy greater than 500 eV, forward scattering is dominant. The multi-scattering, backscattering, and forward scattering are shown in Fig. 2.13.

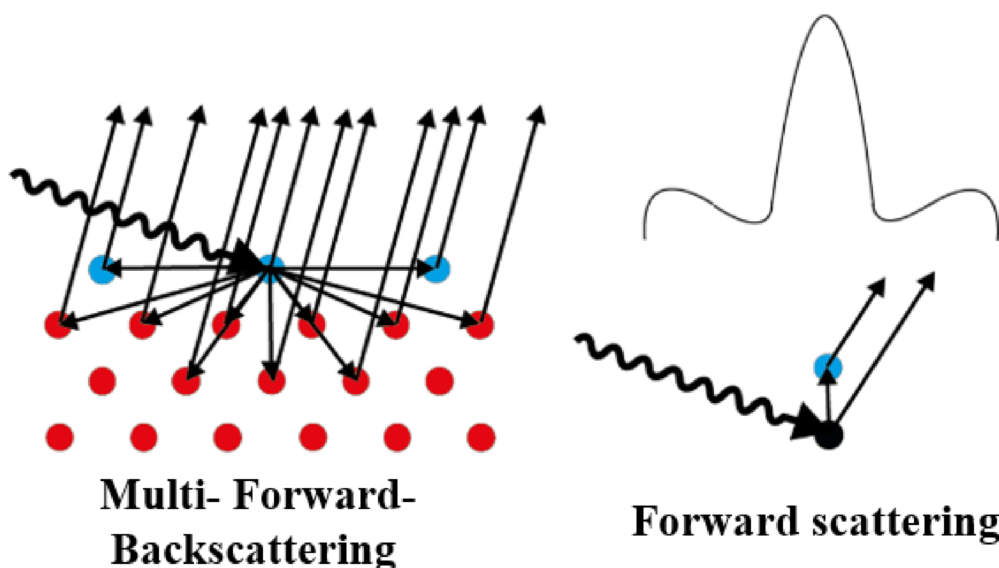

Figure 2.13: Scattering models corresponding to the multi-scattering, backscattering, and forward scattering. [32]

There are many theories to explain PED. Here, the single scattering cluster (SSC)

model is first introduced, and then the multi-scattering (MS) model is introduced. The SSC theory with plane wave approximation (SSC-PW) for the single scattering is shown in Fig. 2.14.

In the photo-excitation process, photoelectron intensities are described by the following equation: [33]

$$I(\mathbf{k}) \propto |\langle \Psi(\boldsymbol{r},\boldsymbol{k})|\hat{\varepsilon}\,\boldsymbol{r}|\Psi_c(\boldsymbol{r})\rangle|^2 \quad (9)$$

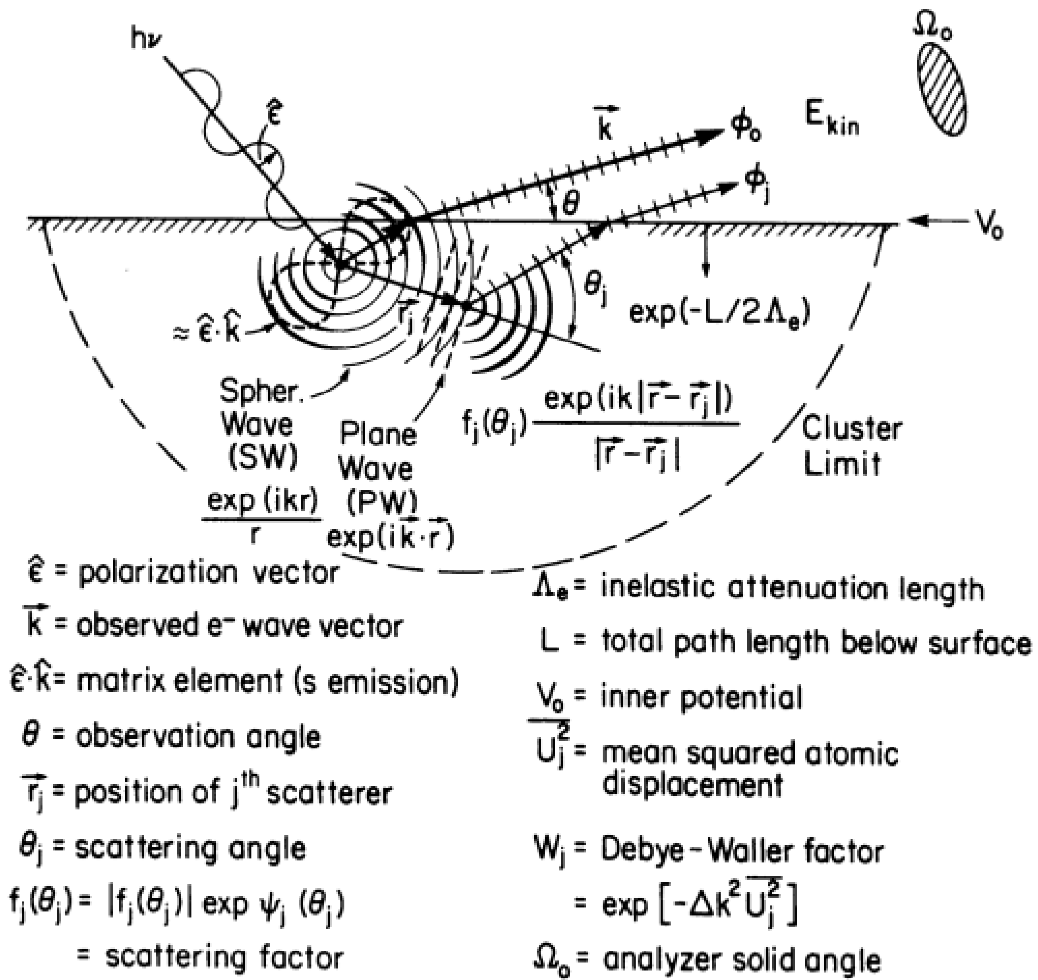

Figure 2.14: Principle of Single Scattering Cluster (SSC) in PED process [33,34].

where $\Psi_c(\mathbf{r})$ is the initial core-electron wave function with wave vector **r**, the $\Psi(\mathbf{r},\mathbf{k})$ is the final photoelectron wave function. In SCC, photoelectrons are scattered by surrounding atoms *j*, the scattered atoms act as new scattering grids $\mathbf{r}_j$ to surface with

wave vector **k**. Thus, the final state wave function is the sum of the individual scattering grid points:

$$\Psi_j\ (\boldsymbol{r},\boldsymbol{k}) = \Phi_0\ (\boldsymbol{r},\boldsymbol{k})\ +\ \sum_j \Phi_j\ (\boldsymbol{r},\boldsymbol{r_j},\rightarrow \boldsymbol{k}) \quad (10)$$

where Φ_0 is the superposition of the original wave (unshattered), Φ_j represents all the singly scatter waves. The initial emission Φ_0, arrives at $\mathbf{r_j}$ to a scatterer j. Finally, it is

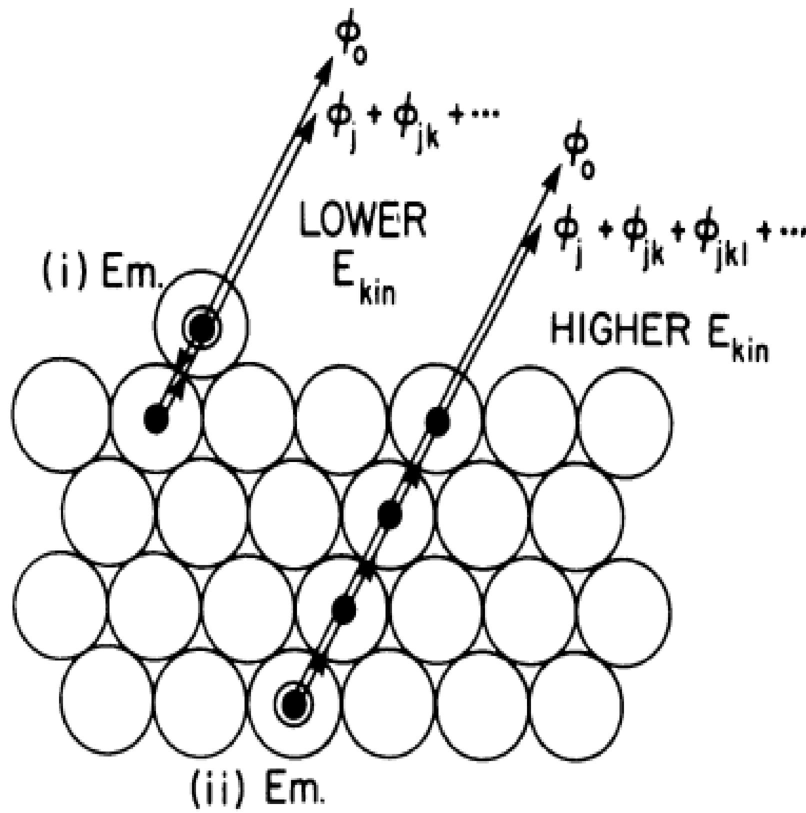

Figure 2.15: Two types of multiple-scattering corrections to the SSC model in PED process. [33]

emitted from the direction of the surface **K**. Φ_0 is related to $e^{ikr/r}$,[33] Φ_j is associated with $e^{ik(r-r_j)/(r-r_j)}$. It is worth noting that, photoelectrons decay is ignored in Eq.10. MS models (Fig. 2.15) explain experimental results more than SSC.

In the case of energy higher than 500 eV, multiple forward scattering is dominant.

For the MS model, it can be described by the following equation:

$$\Psi_j\ (\boldsymbol{r},\boldsymbol{k}) = \Phi_0\ (\boldsymbol{r},\boldsymbol{k})\ +\ \sum_j \Phi_j\ (\boldsymbol{r},\boldsymbol{r_j},\rightarrow \boldsymbol{k})\ +\ \sum_j \sum_k \Phi_j\ (\boldsymbol{r},\boldsymbol{r_j},\rightarrow \boldsymbol{r_k} \rightarrow \boldsymbol{k})$$
$$+\ \sum_j \sum_k \sum_l \Phi_j\ (\boldsymbol{r},\boldsymbol{r_j},\rightarrow \boldsymbol{r_k} \rightarrow \boldsymbol{r_r} \rightarrow \boldsymbol{k}\ldots\ldots \qquad (11)$$

2.2.2.1 Photoelectron hologram (PEH).

The angle-scan PED is one of PEH. When a photon (e.g., X-ray) irradiates the matter, the photoelectrons are excited. Then they are scattered by the surrounding atoms, forming interference patterns in the angular distribution of photoelectrons. Thus, a photoelectron hologram can be formed, which can reveal local atomic structure around a specific atom. [35-37] Figure 2.16 shows the experimental setup and schematic diagram of PEH. Figure 2.17(a) shows sample holder in PED and (b) PED process.

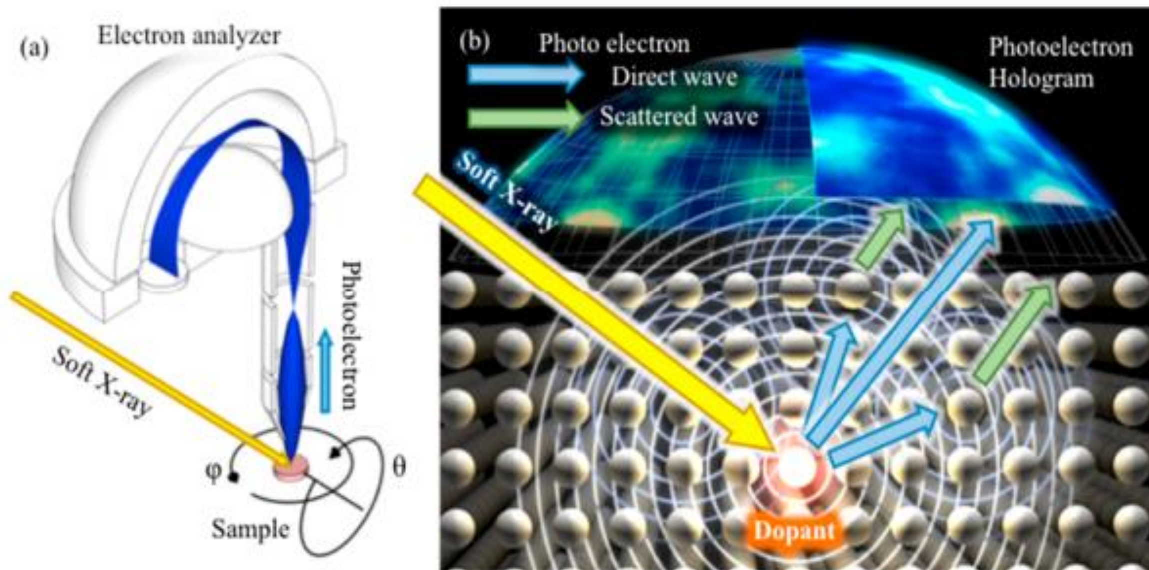

Figure 2.16. (a) The experimental setup of PEH in BL25SU at SPring-8;
(b) Interfere patterns of PEH. [36]

Figure 2.18 shows Si 2p and As 3d PEHs for As-doped Si (001). Three chemical states of the dopant (As) are observed in As 3d PES spectrum [See Fig. 2.18 (c)], and the corresponding PEHs are shown in Fig. 2.18 (b). As can be seen, the chemical state discriminated PEHs are observed. [36]

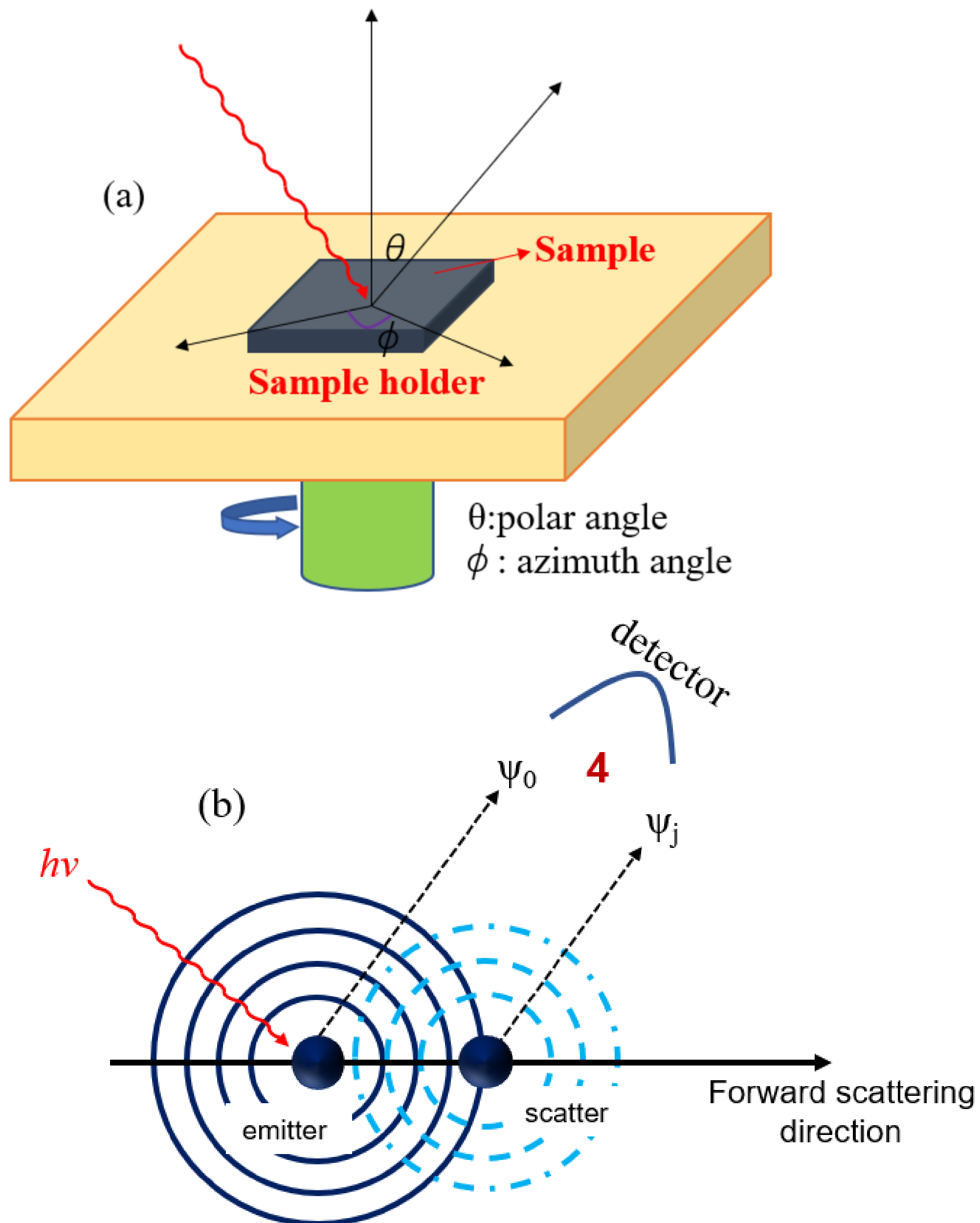

Figure 2.17. (a) Sample holder in PED experiments can adjust with polar and azimuth angles; (b) PED process and photoelectron interferometry detection.

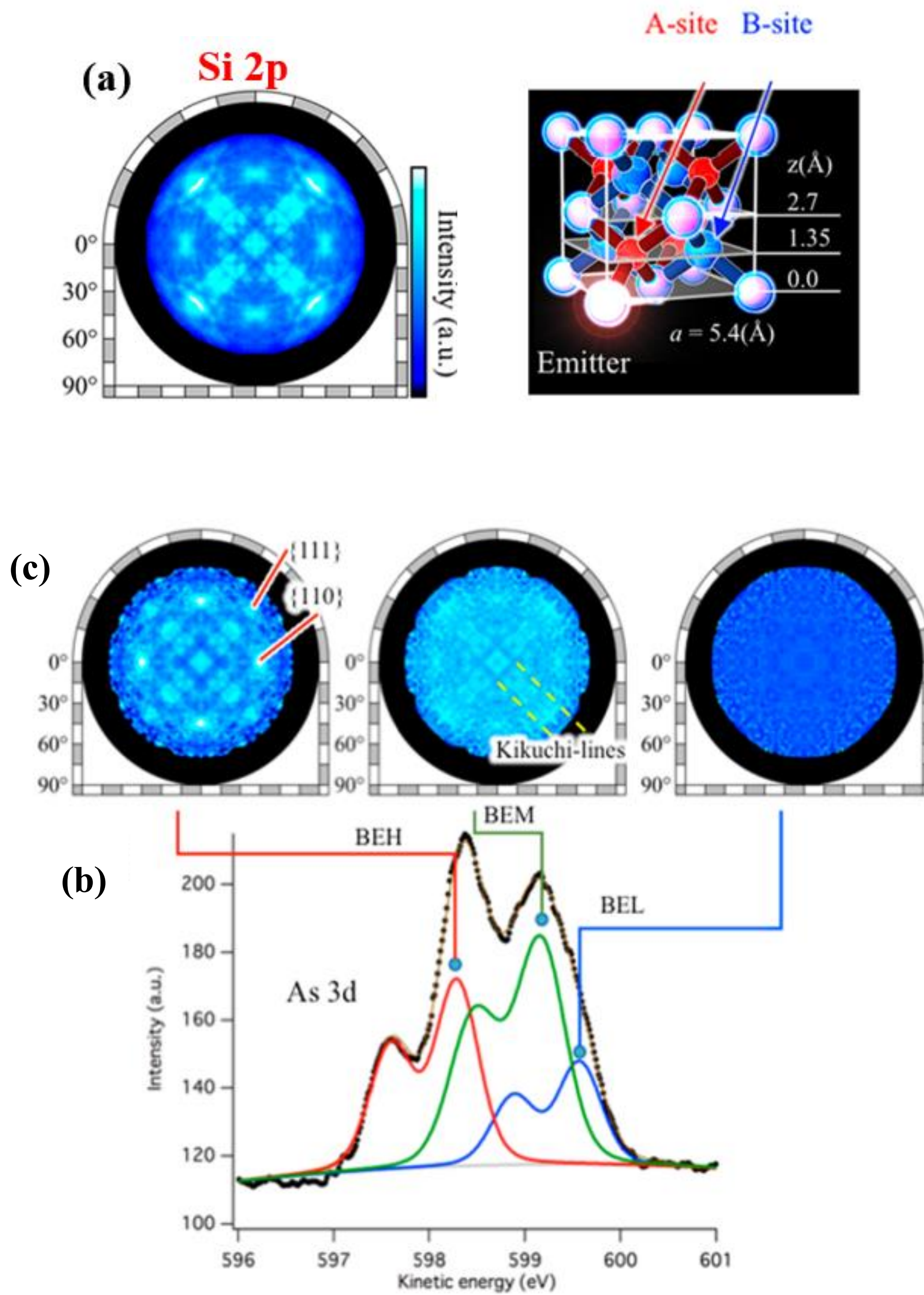

Figure 2.18. (a) Si 2p PEH and the corresponding structure;
(b) PES of As 3d and (c)the corresponding PEHs in As doped in Si. [36]

2.2.2.2 PEH of simulation.

Simulated PEHs are useful and necessary to reproduce the local atomic structures. In the present thesis, SPEA-MEM/SPEA-L1 (scattering pattern extraction algorithm using the maximum entropy method/L1 regularization) developed by Matsushita et al was used to reproduce the reconstructed atomic images. The PEHs of C1s in a diamond is shown in the Fig. 2.19 (a): The left is the experimental result and the right is the simulation one. In this figure, the simulated PHE reproduces the experimental PEH quite well. The reconstructed atomic images based on varied cross sections (z = 0, 0.89, 1.78, and 2.67 Å) are shown in Fig. 2.19 (b).

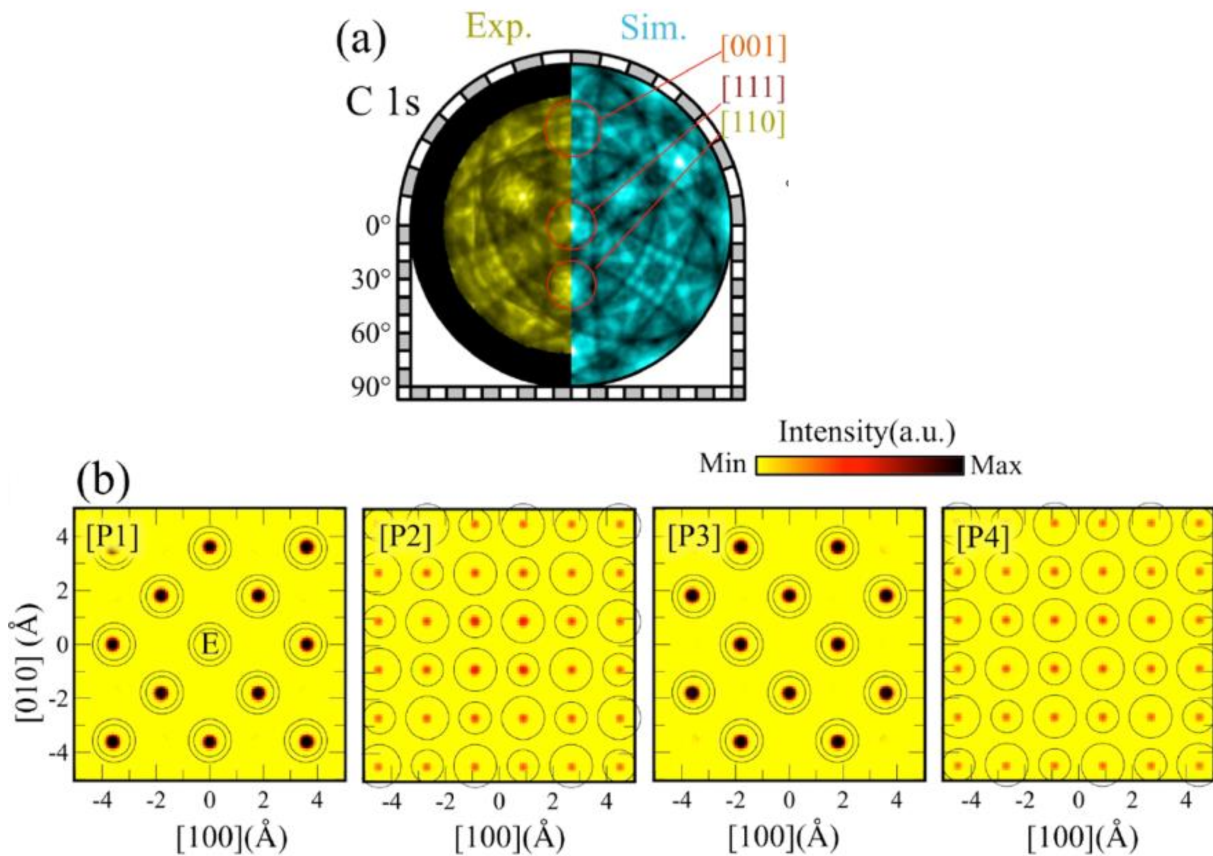

Figure 2.19. (a) Experimental and simulated C1s PEH in diamond; (b) Reconstructed atomic images. [37]

2.2.3 Auger electron spectroscopy (AES).

AES is a surface-sensitive method of materials. Auger electrons are generated from the Auger effect. [38-40] The kinetic energies of the Auger electrons are independent of the energy of the incident photon, meaning that it depends only on the energy difference between the energy levels, as shown in Fig. 2.20. [41] AES probes elements near the surface because information depth is usually below 2nm.[42] Thus, AES is widely used in catalysis, adsorption, corrosion, and other fields.

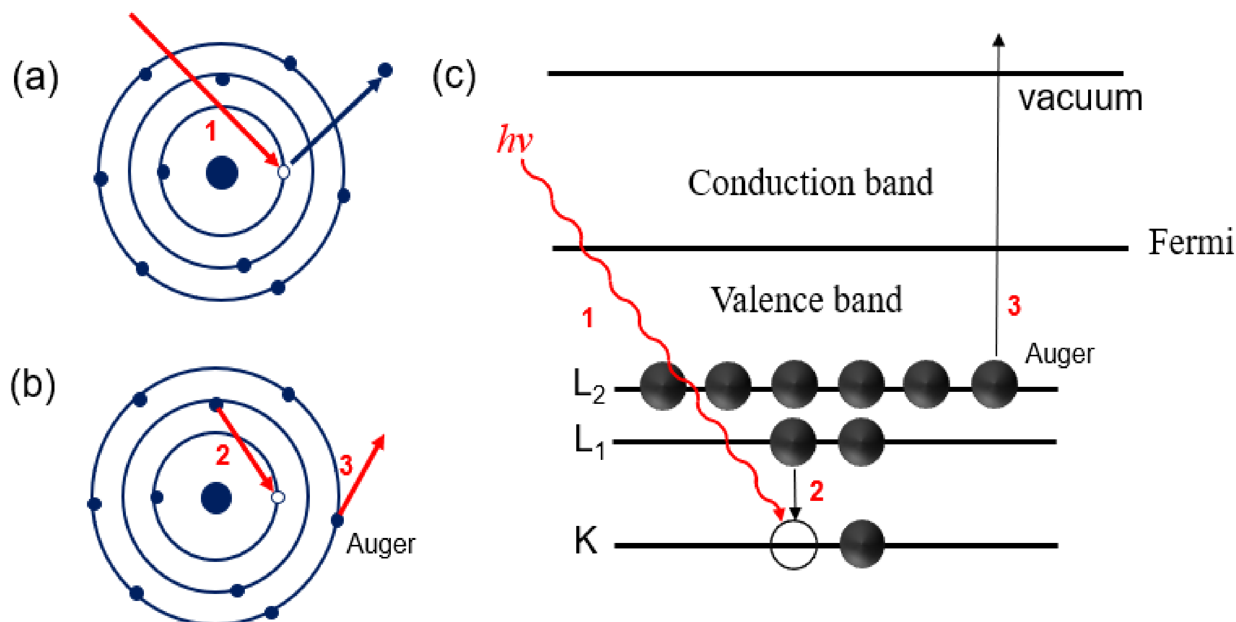

Figure 2.20: (a) Photoelectron is excited; (b) the outer electron fills the hole; (c) energy level of Auger excitation process.[41]

In the Auger process, the electron from an inner core level is excited with photo-irradiation, forming a core hole at the core level. Then, the outer electron fills the core holes and an electron (Auger electron) at the outer core level is excited above the vacuum level.

2.2.3.1 Auger transition probability and fluorescence probability

The decay process of Auger transition and fluorescence emission is shown in Fig. 2.21. Auger transitions dominate when atomic numbers are low, while fluorescence emission is more likely to occur when atomic numbers are higher. Thus, AES is particularly effective for the detection of light elements.

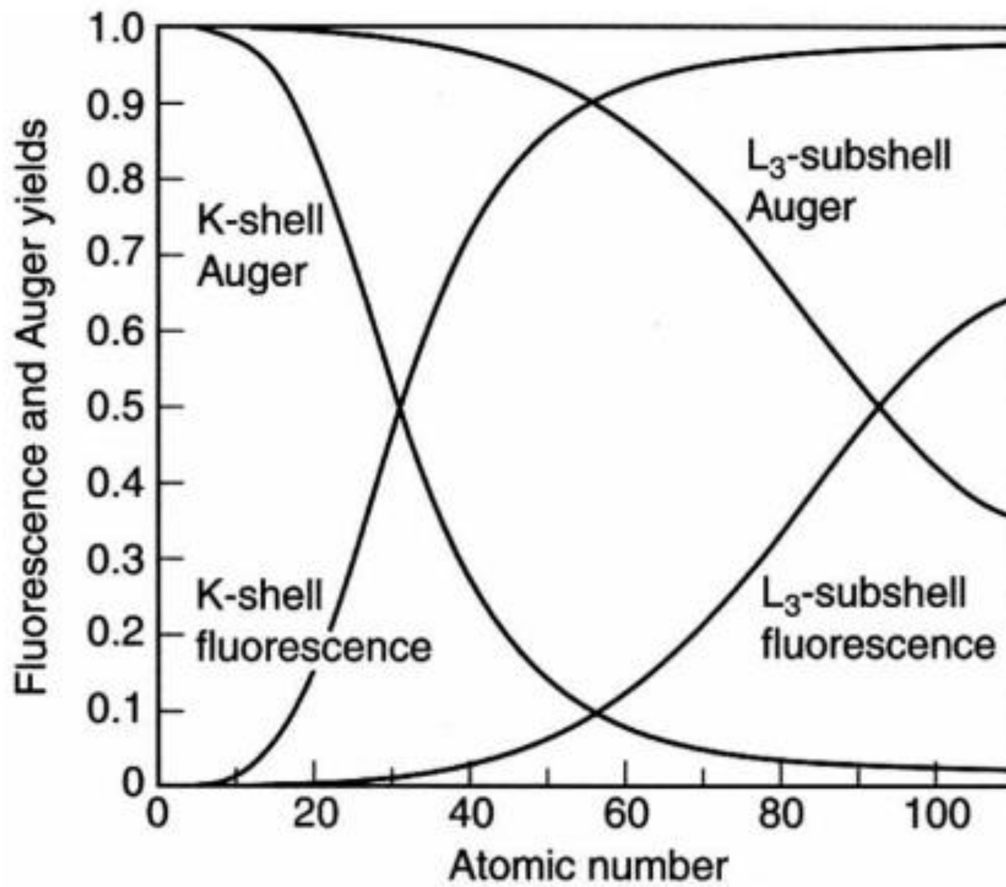

Figure 2.21: Florescence and Auger yield as a function as atomic number. [43]

2.2.4 X-ray absorption

When an X-ray with initial intensity I_0 penetrates the sample, the x-ray intensity decays exponentially. According to Beer-Lambert law, the intensity after penetration I_t, and the initial intensity I_0 are described by the following [44-50]:

$$I_t = I_0 \ e^{-\mu(E)d} \tag{12}$$

where μ is absorption coefficient, d is thickness of the sample. μ is described as following equation[50]:

$$\mu\,(E) \approx \frac{\rho Z^4}{AE^3} \tag{13}$$

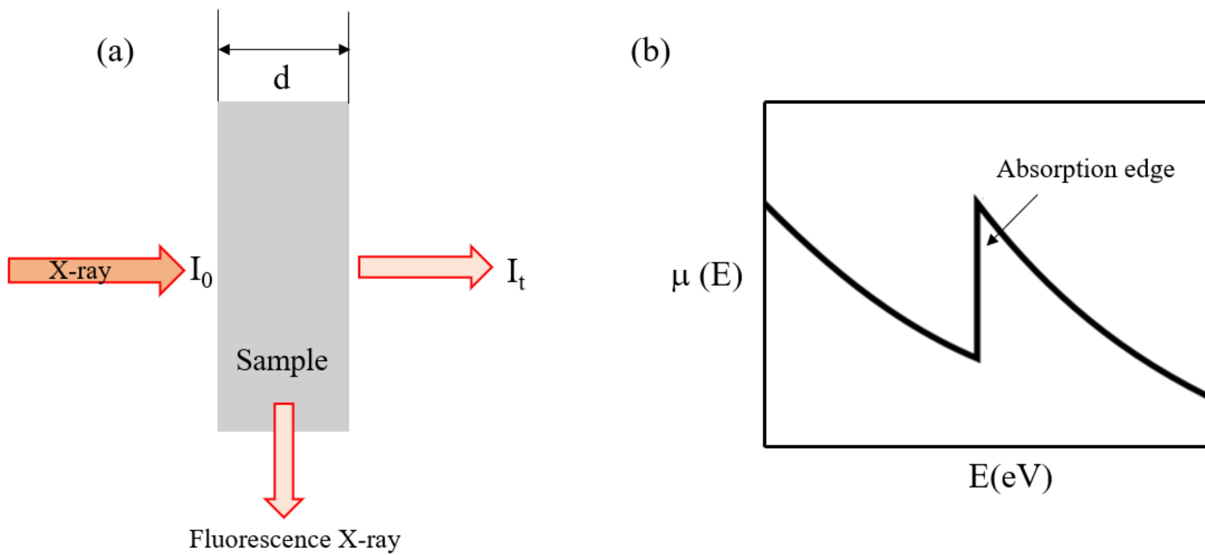

Figure 2.22: (a) Schematic of X-ray incidence and absorption.
(b) absorption coefficient changes as the energy.

where ρ is electron density, Z is atomic number and A is atomic mass. When photon energy is equal to energy difference between the core level and unoccupied level, the absorption coefficient is suddenly increase.[51] For x-ray absorption, there are three methods to measure the absorption; transmission method, fluorescence method, and electron yield method.

2.2.4.1 Transmission method.

The transmission method is generally used when an incident x-ray is a high energy.[46,52] Figure 2.23 shows the schematic of transmission method where I_0 and I_t represent the initial intensity of X-ray and transmitted density of X-rays, respectively. The

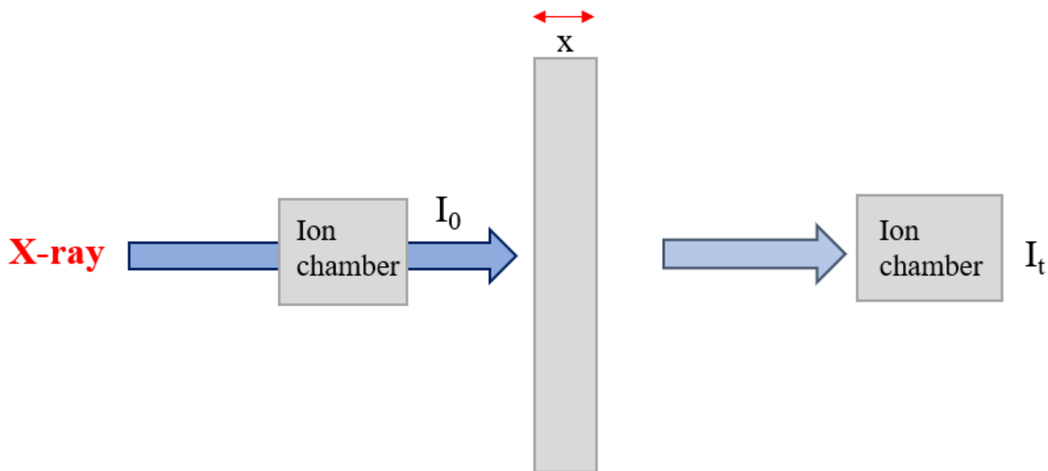

Figure 2.23: Transmission mode.

ionizing radiation intensity of X-rays is detected by an ion chamber. He gas is usually used in the ion chamber to avoid attenuation of the intensity of X-rays.[53] When X-rays reach to the ion chamber, the X-rays interact with gas molecules, generating electrons and positive ion pairs. They are separated under the voltage at the upper and lower ends. The ionized current is proportional to X-ray intensity. Thus, X-rays absorption measurements can be possibly performed.

The relationship between the absorption coefficient, thickness, and intensity can be expressed as following equation:

$$\mu = \frac{1}{x} \ln \left(\frac{I_0(E)}{I_t(E)} \right) \quad (14)$$

2.2.4.2 Fluorescence method.

Fluorescence method is a powerful method to measure low concentration elements and ultra-thin layers. The detection concentration limit is several orders of magnitude lower than transmission method. However, fluorescence method is not suitable for light elements.[54] Fluorescence mode has two yields for measurements: total fluorescence yield (TFY) and partial fluorescence yield (PFY).[55] Under the excitation of X-rays, the electrons in the inner layers are excited, and then the electrons in the outer layer occupy the holes, that is fluorescence. This method is widely used in elemental and chemical analysis. Typical PFY is shown in Fig. 2.24. The relationship between the absorption coefficient and intensity of the measured intensity can be expressed as:

$$\mu \propto \frac{I_f(E)}{I_0(E)} \tag{15}$$

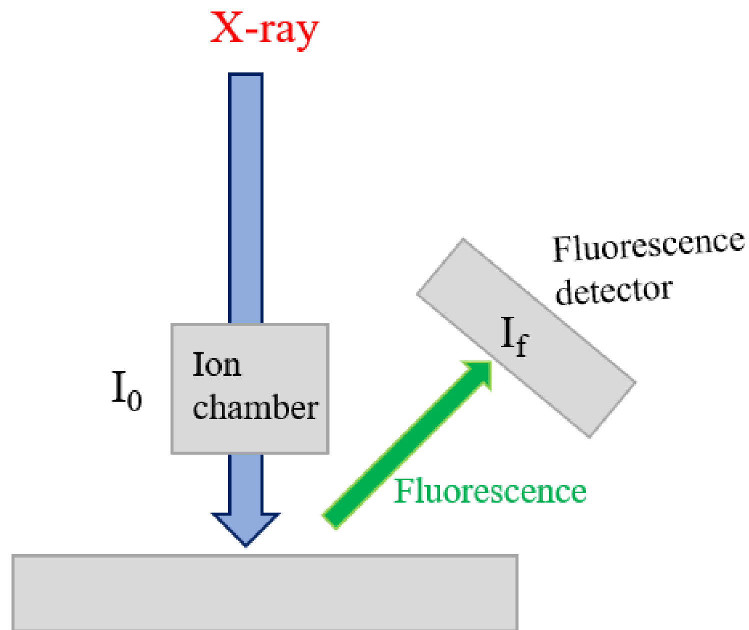

Figure 2.24: PFY model.

2.2.4.3. Electron yield method.

Electron yield method is often used to probe surface because the information depth of the electron yield is around a few nm.[56] For the electron yield, total electron yield (TEY) and partial electron yield (PEY) are usually used.[57,58] TEY is measured by drain current of the sample. PEY is detected with the electron yield at a particular energy region. Note that AEY is a method for detecting Auger electrons in PEY. AEY is detected with the Auger electron of a particular Auger energy. Compared to the fluorescence mode, the escape depth of the electrons is shorter, so it is surface sensitive. [56-60] TEY and PEY are shown in the Fig. 2.25. The relationship between the absorption coefficient μ, the initial intensity I_0, and the intensity absorption I_e, can be expressed as:

$$\mu \propto \frac{I_e(E)}{I_0(E)} \text{ (PEY) or } \mu \propto \frac{I_t(E)}{I_0(E)} \text{ (TEY)} \tag{16}$$

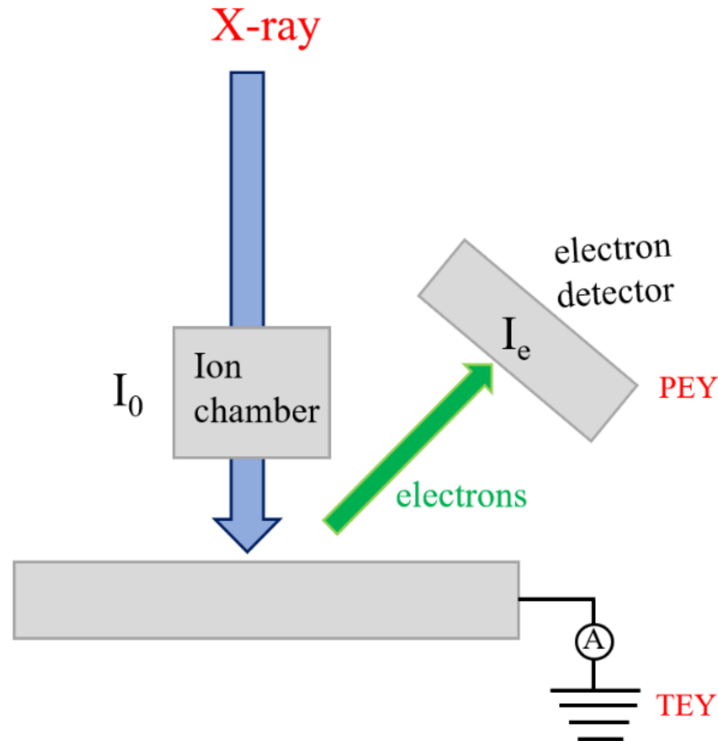

Figure 2.25: PEY and TEY models of XAS.

2.2.4.4 X-ray absorption near-edge structure (XAFS).

XAFS is a powerful method to measure the local atomic structures. When the energy of X-ray energy resonates with the inner electron shell (K or L, M shell) of the element, the inner electrons of the atom absorb the X-ray, resulting in a sudden rise in the continuous spectrum (absorption edge). XAFS consists of two parts: spectrum in the low-energy region within 50-60 eV above the threshold is called as X-ray absorption near-edge structure (XANES) while the energy region about 50 eV to 1000 eV above the threshold is called as extended X-ray absorption fine structure (EXAFS). [61,62]

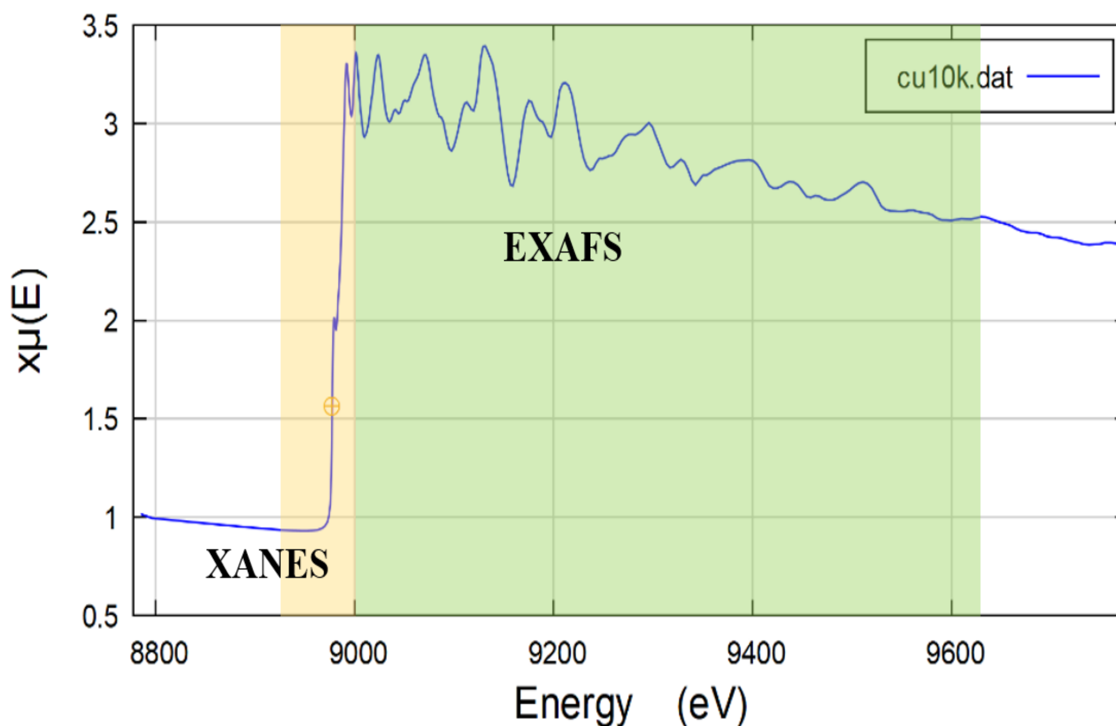

Figure 2.26: XAFS spectrum of Cu at 10K.

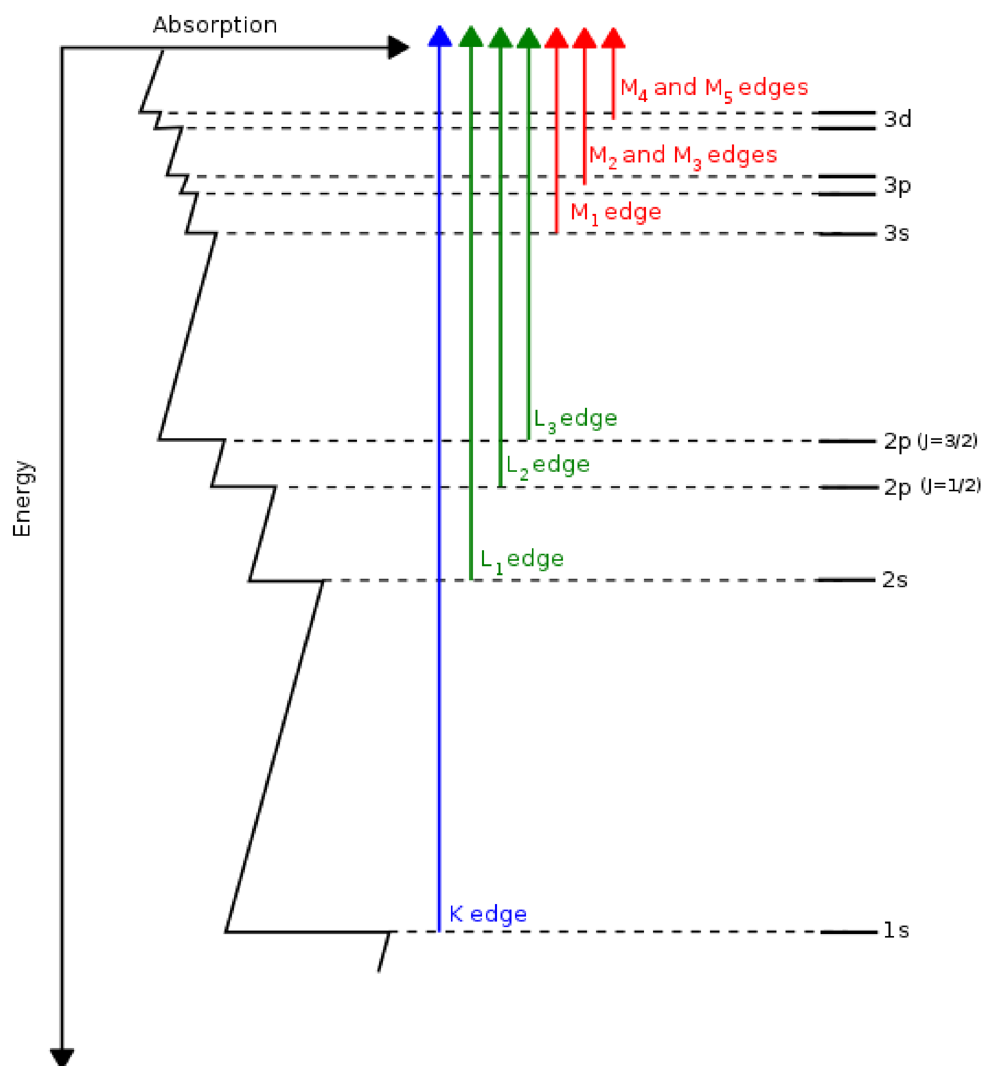

Figure 2.27: XAFS adsorption edges according to their core energy levels. [63]

The shells of K, L, and M absorption edges are shown in Fig. 2.27. XANES and EXAFS principles are shown in Fig. 2.28. XANES spectra exhibit the unoccupied states while the coordination number of the atom and bond length of neighbor atoms are obtained from analysis of EXAFS.

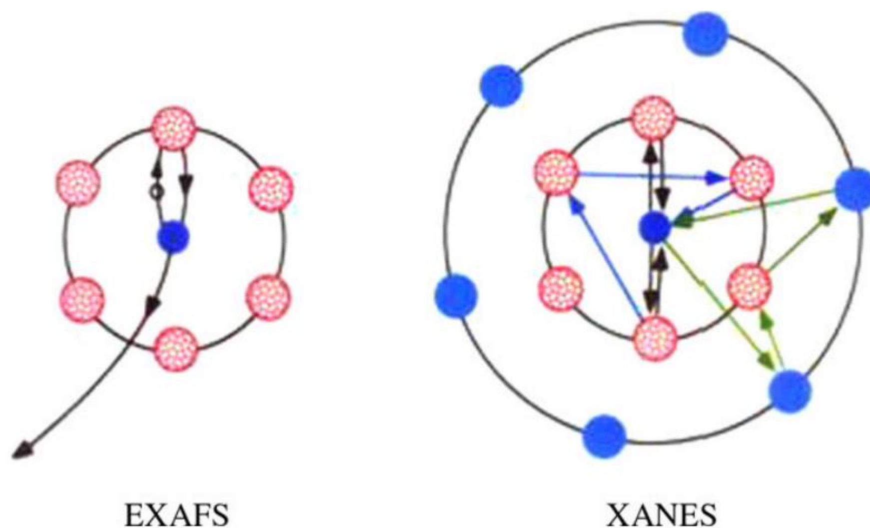

Figure 2.28: Scattering types of XANES and EXAFS. [64]

2.2.4.5 XANES.

For XANES, it has a wide range of applications in the fields of catalysis, adsorption, doping, etc. For example, when studying compounds with similar structures, the main peak of the spectral line moves to the high-energy region with the increase of the oxidation state. Figure 2.29 shows XANES of different oxidation states of V.[65] The main peak of the spectral line moves to the high-energy region. This is because the effective charge of the central atom increases, resulting in a greater attraction for electrons. XANES spectrum and XANES simulations have been successfully used to reveal local atomic structure.[66-68]

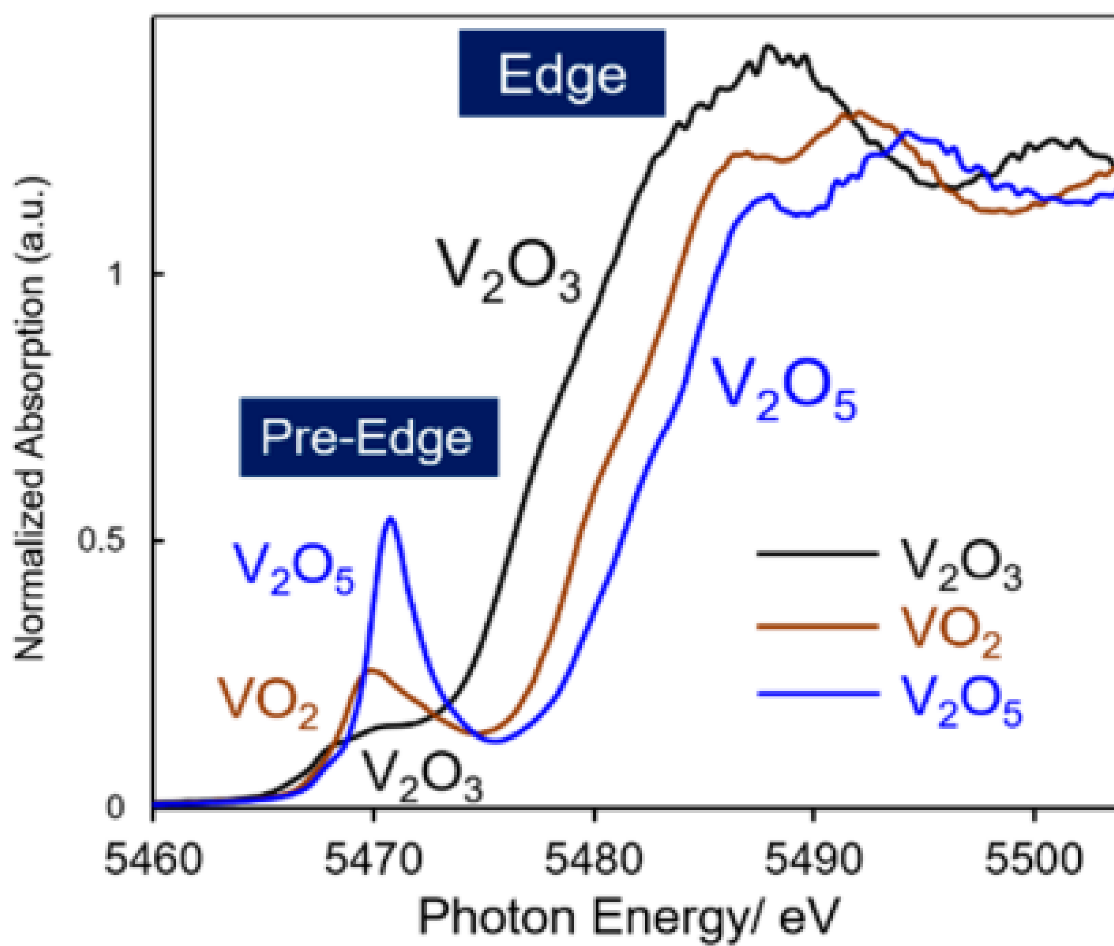

Figure 2.29: V K-edge XANES spectra of V compounds. [65]

2.2.4.6 XANES simulation.

2.2.4.6.1 FEFF.

FEFF is a commonly used simulation software of XANES, EXAFS, XMCD, etc. It is an automated program based on ab initio multiple scatting path-expansion developed by John. J. Rehr et al. [69-72] The name FEFF comes from the effective curved wave scattering amplitude (f_{eff}). The program is based on real-space Green's function approach including the self-consistent spherical muffin-tin (MT) scattering potential. MT scattering potential is schematically shown in Fig. 2.30. The schematic diagram of the XANES simulation process based on f_{eff} is shown in Fig. 2.31.[73] This process mainly consists of 4 parts: input structural data of (feff. Inp) file (1); set calculation parameters (2); select the spectrum setting (3); output the spectrum (4).

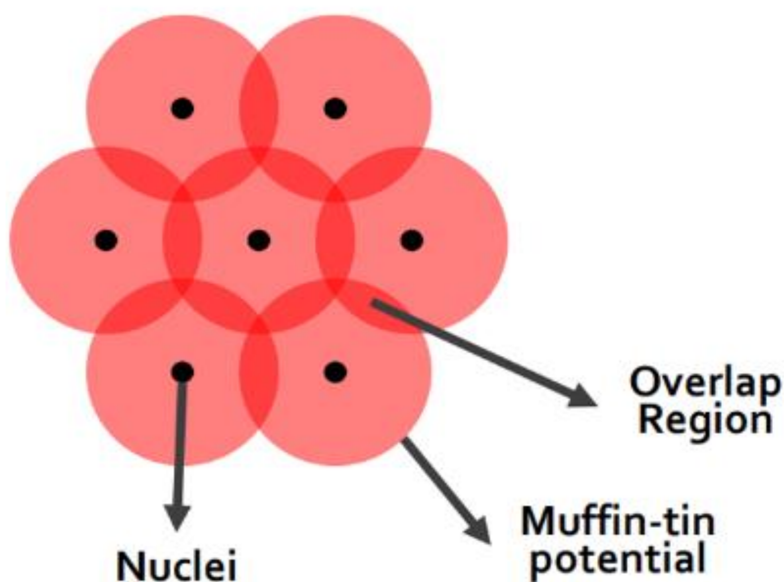

Figure 2.30: Schematic of MT scattering potential. [69(b)]

Here, XANES simulated spectrum is calculated using copper as an example. Firstly, import the cif file of Cu in the website page of web atoms or database (see Fig. 2.32)[74], then set the parameters you need, and finally output the inp file (Fig. 2.33).

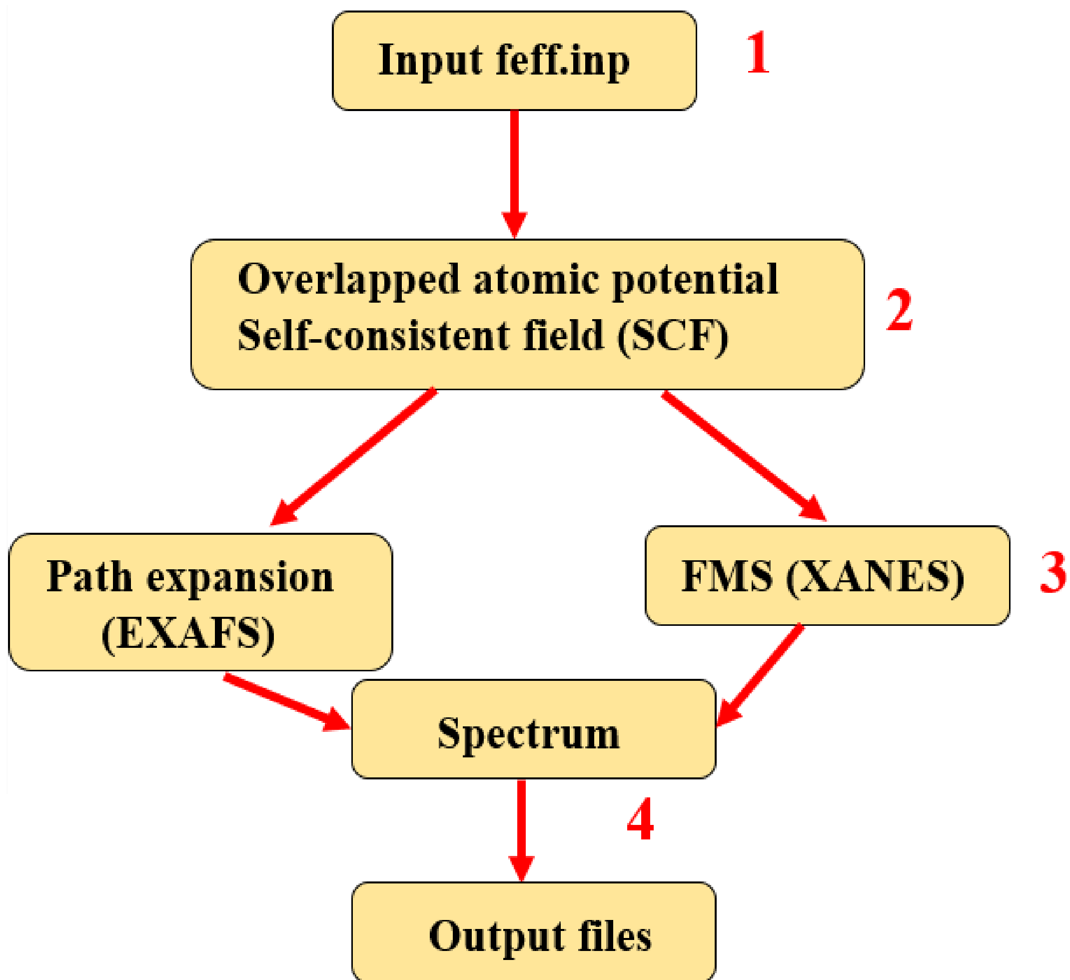

Figure 2.31: Flow chart of FEFF program.[73]

Secondly: import the file (feff.inp), and select the spectrum setting (XANES). Then set parameters of FMS, LDOS, SCF, S_0^2, etc. After that, click run (see Fig. 2.34). Finally, click plot bottom, and then XANES spectrum of Cu is obtained (see Fig. 2.35).

Space group: fcc Output: feff.inp

Edge: K ipot style: Feff8 / elements

A: 3.61 B: 3.61 C: 3.61

α: 90 β: 90 γ: 90

Cluster size: 6.5 Longest path: 5.0

SCF radius: 5.0

Shift vector: 0 0 0

Figure 2.32: Preparation inp file in web atoms.

```
* --*--*--*--*--*--*--*--*--*--*--*--*--*--*--*--*--*--*--*--*--*--*--*--*--
* title = Copper example
* space = fcc
* a     =   3.61000    b     =   3.61000    c     =   3.61000
* alpha =  90.00000    beta =  90.00000    gamma =  90.00000
* rmax  =   6.50000    core  = cu
* polarization = 0  0  0
* shift =   0  0  0
* atoms
* # el.     x           y           z         tag
*   Cu     0.00000     0.00000     0.00000   Cu
* --*--*--*--*--*--*--*--*--*--*--*--*--*--*--*--*--*--*--*--*--*--*--*--*--

* --*--*--*--*--*--*--*--*--*--*--*--*--*--*--*--*--*--*--*--*--*--*--*--*--
*  total mu*x=1:  4.057 microns,  unit edge step:  4.726 microns
*  specific gravity:  8.971
* --*--*--*--*--*--*--*--*--*--*--*--*--*--*--*--*--*--*--*--*--*--*--*--*--
*  normalization correction:    0.00046 ang^2
* --*--*--*--*--*--*--*--*--*--*--*--*--*--*--*--*--*--*--*--*--*--*--*--*--

TITLE Copper example

HOLE      1   1.0   * FYI: (Cu K edge @ 8979 eV, 2nd number is S0^2)
*         mphase,mpath,mfeff,mchi
CONTROL   1      1      1      1
PRINT     1      0      0      0

RMAX      5.0
 * POLARIZATION  0   0   0

POTENTIALS
 * ipot   Z      tag
    0     29     Cu
    1     29     Cu


ATOMS                     * this list contains 87 atoms
*    x          y          z      ipot tag             distance
   0.00000    0.00000    0.00000   0   Cu              0.00000
   1.80500    1.80500    0.00000   1   Cu.1            2.55266
  -1.80500    1.80500    0.00000   1   Cu.1            2.55266
   1.80500   -1.80500    0.00000   1   Cu.1            2.55266
  -1.80500   -1.80500    0.00000   1   Cu.1            2.55266
   1.80500    0.00000    1.80500   1   Cu.1            2.55266
  -1.80500    0.00000    1.80500   1   Cu.1            2.55266
   0.00000    1.80500    1.80500   1   Cu.1            2.55266
   0.00000   -1.80500    1.80500   1   Cu.1            2.55266
   1.80500    0.00000   -1.80500   1   Cu.1            2.55266
  -1.80500    0.00000   -1.80500   1   Cu.1            2.55266
   0.00000    1.80500   -1.80500   1   Cu.1            2.55266
   0.00000   -1.80500   -1.80500   1   Cu.1            2.55266
   3.61000    0.00000    0.00000   1   Cu.2            3.61000
  -3.61000    0.00000    0.00000   1   Cu.2            3.61000
   0.00000    3.61000    0.00000   1   Cu.2            3.61000
   0.00000   -3.61000    0.00000   1   Cu.2            3.61000
```

Figure 2.33: Inp file of Cu.

Figure 2.34: Import file in FEFF program and set parameters for calculation.

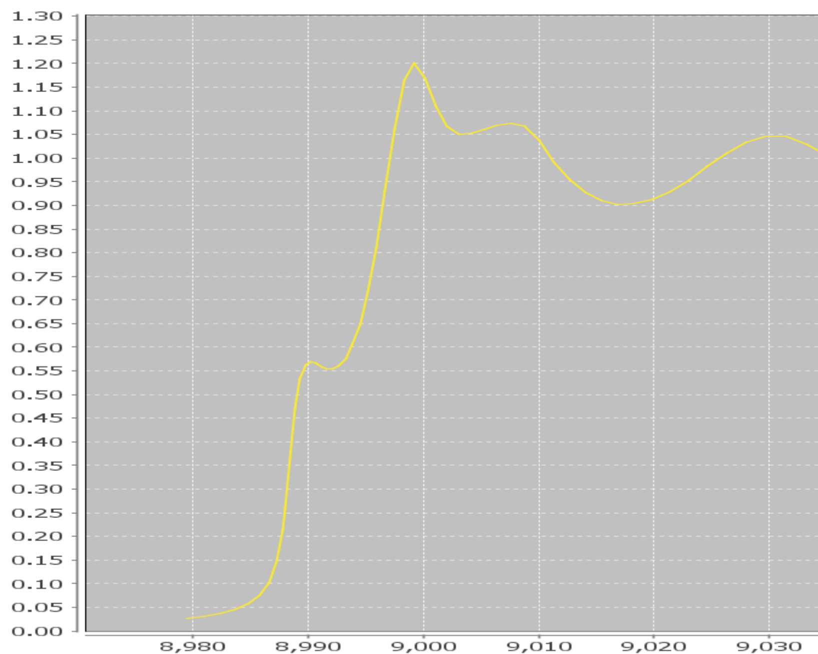

Figure 2.35: Simulated XANES spectrum of Cu K edge.

2.2.5 Secondary-ion mass spectrometry (SIMS)

SIMS is a useful and powerful technique to obtain information on the elemental depth distribution of the solid. The apparatus generally has 5 parts: ion gun, injection chamber, vacuum chamber, mass spectrometer, and mass detector, as shown in Fig. 2.36.[75] The most commonly used SIMS methods are: time-of-flight SIMS (ToF-SIMS), magnetic sector SIMS, and quadrupole mass spectrometry SIMS. Solid surface is sputtering with accelerated high-energy ions. Then sputtered and desorbed secondary ions are extracted

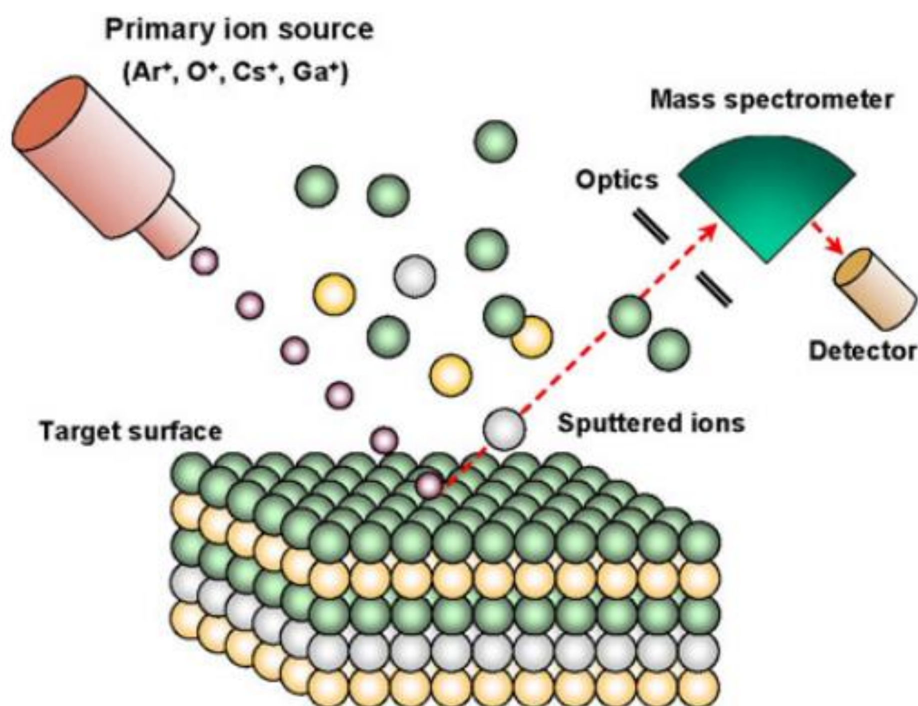

Figure 2.36: Schematic of SIMS. [75]

by the mass spectrometer. Finally, the detector detects the ions and analyzes the mass spectrum. Figure 2.37 shows the diagram of ToF-SIMS. [76,77] The sputtered secondary ions are accelerated through a distance of length L to reach the detector. According to Newton's

laws, the following formula is given by:

$$\frac{1}{2}mv^2 = qV \quad , \quad v = \sqrt{2qV/m} \tag{17}$$

$$t = \frac{L}{v} = \frac{L}{\sqrt{2qV/m}} \quad , \quad m/q = m/ze = \frac{2t^2V}{L^2}, m/z = \frac{2t^2V}{eL^2} \tag{18}$$

where m is ion mass, q is ionic charge, L is flying distance, v is flying speed, and V is accelerating voltage. Through the above formulas, the mass-to-charge ratio of the secondary ions, and the content of various components can be estimated.

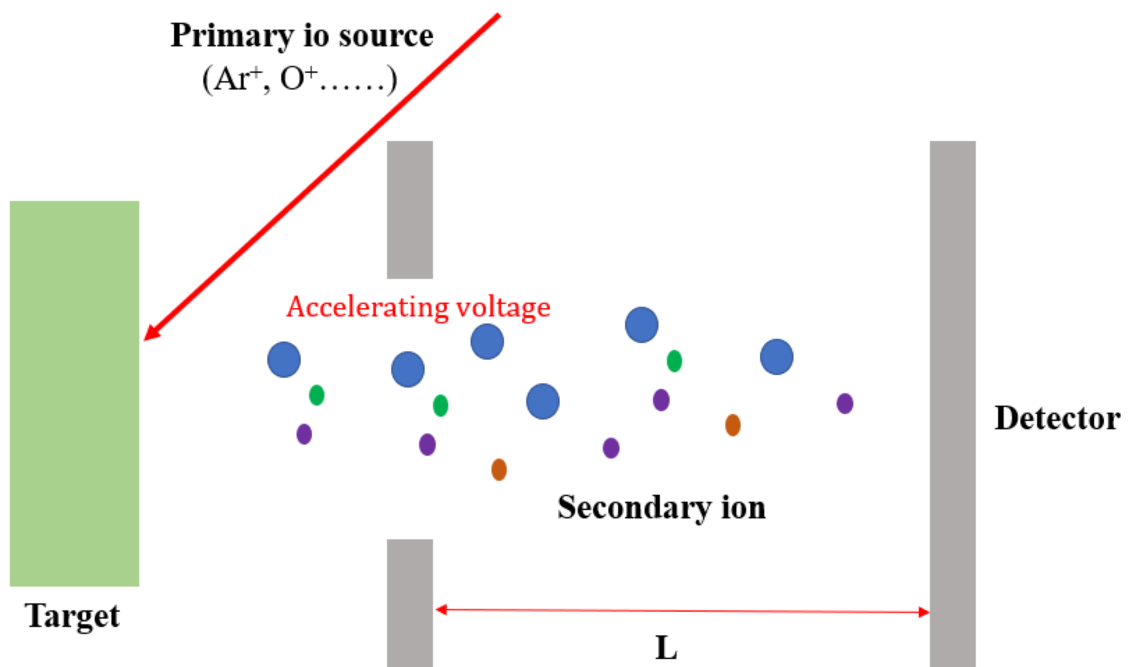

Figure 2.37: Diagram of ToF-SIMS.

2.2.6 Hall effect measurements.

Hall effect measurements with Van der Pauw method are used to measure the carrier concentration.[78-83] This method is useful for the measurement of carrier concentration in

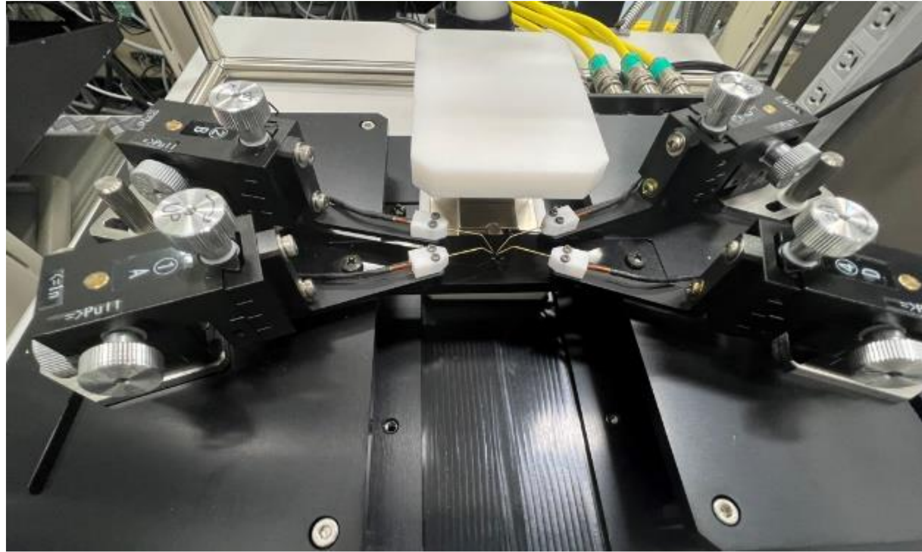

Figure 2.38: Apparatus of Hall effect measurements.

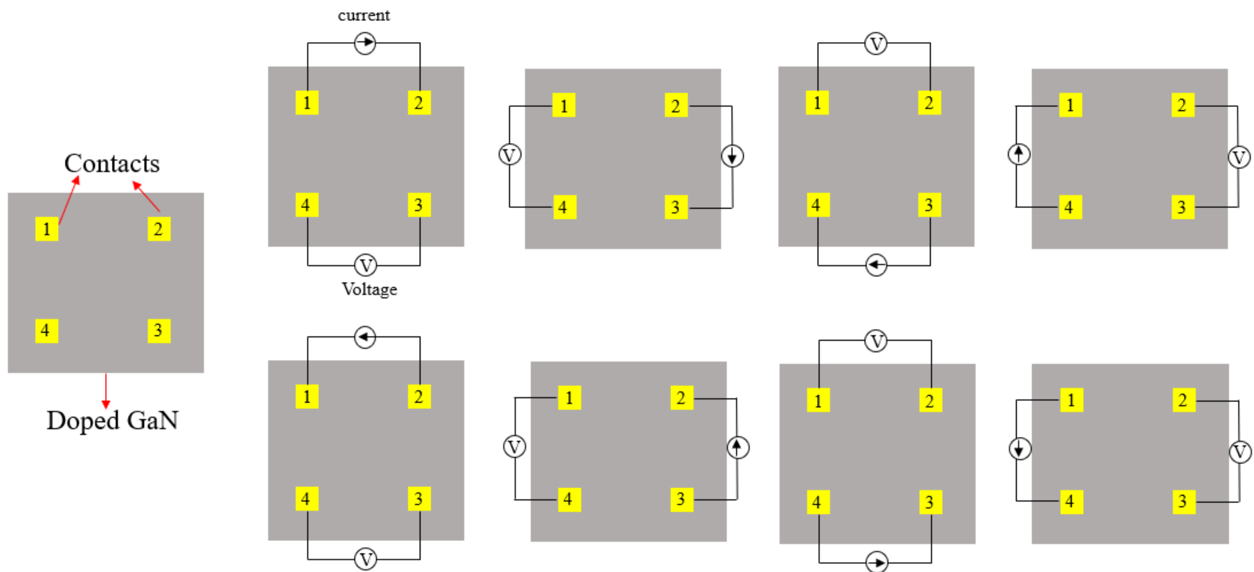

Figure 2.39: Van der Pauw Hall measurement.[79]

the film sample. For Hall effect measurements, the four electrodes are needed, which is shown in Fig. 2.38. Resistivity, polarity of carriers, and majority carrier concentration can be obtained by measuring the change in the current, voltage, and electric field. The Van der Pauw Hall measurement is defined as shown in Fig. 2.39. Sheet resistance (R_S) can be obtained by the Van der Pauw formula.[80]

$$e^{-\pi R_{verical}/R_s} + e^{-\pi R_{horizonal}/R_s} = 1 \quad (19)$$

R(horizonal) and R(vertical) are decided by following formula:

$$R_{\text{horizontal}} = \frac{\frac{V_{43}}{I_{12}}+\frac{V_{21}}{I_{34}}+\frac{V_{34}}{I_{21}}+\frac{V_{12}}{I_{43}}}{2}, \quad R_{\text{vertical}} = \frac{\frac{V_{14}}{I_{23}}+\frac{V_{23}}{I_{14}}+\frac{V_{41}}{32}+\frac{V_{32}}{I_{41}}}{2} \quad (20)$$

In the case of $R_{\text{vertical}} = R = R_{\text{horizontal}}$, $R_S = \frac{\pi R}{\ln 2}$.

The magnitude of the Hall voltage (V_H) is defined as the electric field strength:

$$V_H = d \in = \frac{IB}{enh} \quad (21)$$

V_H can be obtained from Eq. 22:

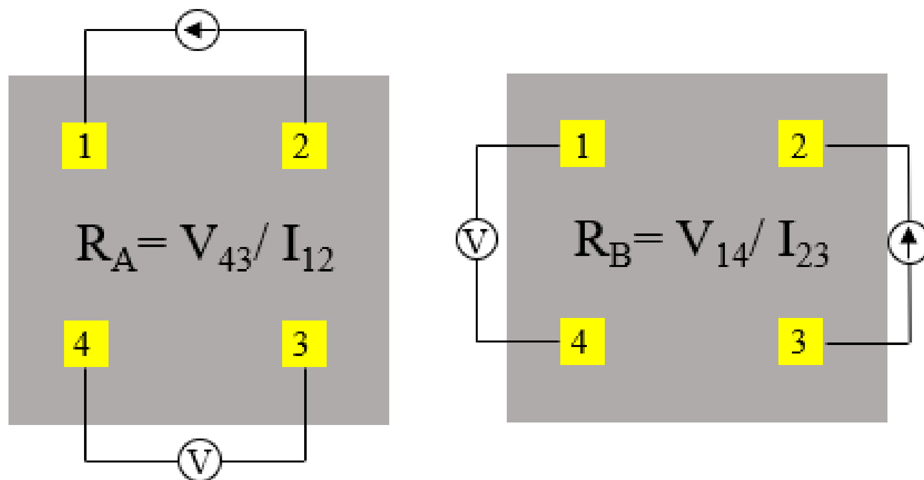

Figure 2.40: Van der Pauw method for measurements of sheet resistance.[81]

$$V_H = \frac{V_{13}+V_{24}+V_{31}+V_{42}}{8} \quad (22)$$

If V_H is positive, the polarity of carriers is positive, that is P-type. If it is negative, the polarity of carries is negative (N-type). Substituting the V_H into Eq.21, the carrier concentration can be determined.

The resistivity of a semiconductor is given by[83]

$$\rho = \frac{1}{q(n\mu_n+p\mu_p)}, \qquad R_s = \rho/h \quad (23)$$

where h is the thickness, n and p are the concentration of electrons and holes, respectively, and μ_n and μ_p are the mobility of the electrons and holes, respectively. Therefore, ρ is described as follows:

$\rho = \frac{1}{qp\mu_p}$ in the case of P type; N type, $\rho = \frac{1}{qn\mu_n}$ in the case of N-type

Since sheet resistance R_S is the resistivity divided by the thickness, R_S is given by

$$R_s = \frac{1}{qn_s\mu}, \mu = \frac{V_H}{R_S IB} \quad (24)$$

Therefore, sheet resistance the polarity, the carrier concentration, and the mobility can be obtained by Hall effect measurements.

2.2.7 Cathodoluminescence (CL)

CL is a powerful method to understand the electronic structure of materials. The principle of CL can be explained as follows: electron-beam is irradiated to solid materials, and then electrons in the valence band are excited to the conduction band. For bulk materials, the excited electrons in conduction band decay directly to the valence band emitting luminescence. In the case of dopants in semiconductor, the electron recombines hole between a bandgap (as shown in the figure below). Therefore, the bandgap electronic structure for doped semiconductors can be obtained using CL.

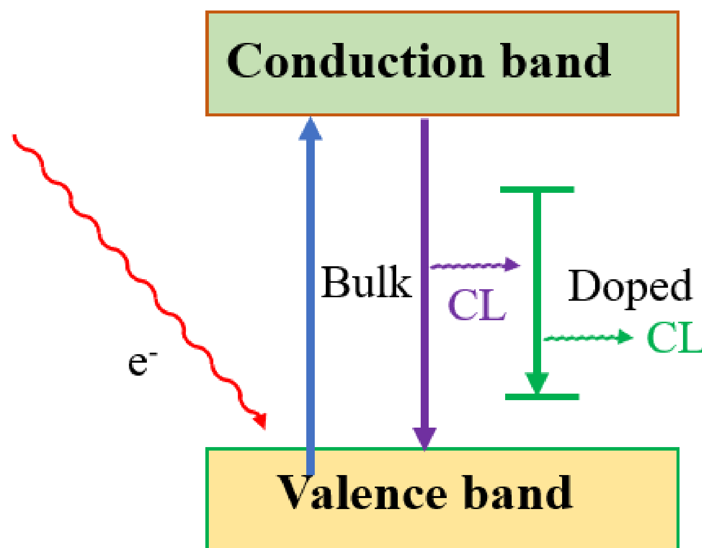

Figure 2.41. The principle of CL in bulk and doped materials. [84]

2.3 References:

1. Iwinska, M., Sochacki, T., Amilusik, M., Kempisty, P., Lucznik, B., Fijalkowski, M., Bockowski, M. *Journal of Crystal Growth*, *456*, 91-96 (2016).
2. Slomski, M., Paskov, P. P., Leach, J. H., Muth, J. F., & Paskova, T. *physica status solidi (b)*, *254*(8), 1600713 (2017).
3. Usikov, A., Soukhoveev, V., Kovalenkov, O., Syrkin, A., Shapovalov, L., Volkova, A., & Ivantsov, V. *Japanese Journal of Applied Physics*, *52*(8S), 08JB22 (2013).
4. K. Siegbahn, C. Nordling, A. Fahlman, R. Nordberg, K. Hamrin, J. Hedman, G. Johansson, T. Bergmark, S.-E. Karlsson, I. Lindgrenf, B. Lindberg, ESCA: Atomic, Molecular and Solid-State Structure Studied by Means of Electron Spectroscopy, Almqvist & Wiksells, Uppsala (1967).
5. K. Siegbahn, C. Nordling, G. Johansson, J. Hedman, P. F. Heden, K. Hamrin, U. Gelius, T. Bergmark, L. O. Werme, R. Manne, Y. Baer, ESCA Applied to Free Molecules, North Holland, Amsterdam (1969).
6. Margaritondo, G. *Physics Today*, *41*(4), 66-72. (1988).
7. Margaritondo, G. 100 years of photoemission. *Physics Today*, *41*(4), 66-72 (1988).
8. Siegbahn, K. to the Royal Society of Sciences of Uppsala, Dec. 3rd, 1965. *Nova Acta Regiae Societatis Scientiarum Upsaliensis* (1967).
9. Hollander, J. M., & Jolly, W. L. *Accounts of chemical research*, *3*(6), 193-200 (1970).
10. Chastain, J., & King Jr, R. C. *Perkin-Elmer Corporation*, *40*, 221 (1992).
11. Van der Heide, P. John Wiley & Sons. (2011).
12. Fadley, C. S. *Journal of Electron Spectroscopy and Related Phenomena*, *178*, 2-32 (2010).
13. Agnarsson, B. (Doctoral dissertation, KTH) (2009).

14. Tonner, B. P., Dunham, D., Droubay, T., & Pauli, M. *Journal of Electron Spectroscopy and Related Phenomena*, *84*(1-3), 211-229 (1997).
15. Sokolov, A. A., & Ternov, I. M. *Akademia Nauk SSSR* (1966).
16. Ternov, I. M. *Physics-Uspekhi*, *38*(4), 409(1995).
17. Wiedemann, H. In *Particle Accelerator Physics* (pp. 647-686). Springer, Berlin, Heidelberg (2003).
18. Willmott, P. *An introduction to synchrotron radiation: techniques and applications*. John Wiley & Sons (2019).
19. Hofmann, A. *The physics of synchrotron radiation* (Vol. 20). Cambridge university press (2004).
20. Pope, C. G. *Journal of chemical education*, *74*(1), 129(1997).
21. Klug, H. P., & Alexander, L. E. *X-ray diffraction procedures: for polycrystalline and amorphous materials* (p. 992) (1974).
22. Shiwaku, H., Mitsui, T., Tozawa, K., Kiriyama, K., Harami, T., & Mochizuki, T. In *AIP Conference Proceedings* (Vol. 705, No. 1, pp. 659-662). American Institute of Physics (2004, May).
23. Ueda, S., Katsuya, Y., Tanaka, M., Yoshikawa, H., Yamashita, Y., Ishimaru, S., ... & Kobayashi, K. In *AIP conference proceedings* (Vol. 1234, No. 1, pp. 403-406). American Institute of Physics (2010, June).
24. Lee, M., Lee, D., Baik, H., Kim, H., Jeong, Y., Yang, M., ... & Kim, J. *Scientific Reports*, *10*(1), 1-9 (2020).
25. Seah, M. P., & Dench, W. A. *Surface and interface analysis*, *1*(1), 2-11(1979).
26. Zöllner, Marvin Hartwig. *Microelectronics meets catalysis: An interdisciplinary approach on the structure-property relationship of single crystalline Ce1-xPrxO2-δ*

films on Si (111). Diss. BTU Cottbus-Senftenberg, 2014.

27. Tanuma, S., Powell, C. J., & Penn, D. R. *Surface and interface analysis*, *21*(3), 165-176(1994); Tanuma, S., Cedric J. Powell, and David R. Penn. *Surface and interface analysis* 35.3 (2003): 268-275.
28. Brundle, C. R., & Crist, B. V. *Journal of Vacuum Science & Technology A: Vacuum, Surfaces, and Films*, *38*(4), 041001 (2020).
29. Siegbahn, K., Gelius, U., Siegbahn, H., & Olson, E. Angular distribution of electrons in ESCA spectra from a single crystal. *Physica Scripta*, *1*(5-6), 272(1970).
30. Woodruff, D. P. *Journal of electron spectroscopy and related phenomena*, *126*(1-3), 55-65 (2002).
31. Fadley, C. S. *Physica Scripta*, *1987*(T17), 39 (1987).
32. Woodruff, D. P. *Journal of Electron Spectroscopy and Related Phenomena*, *256*, 147170 (2022).
33. Fadley, C. S. In *Synchrotron radiation research* (pp. 421-518). Springer, Boston, MA (1992).
34. Fadley, C. S. *Progress in Surface Science*, *16*(3), 275-388 (1984).
35. Yang, A. L., Yamashita, Y., Kobata, M., Matsushita, T., Yoshikawa, H., Píš, I., ... & Kobayashi, K. *Applied Physics Letters*, *102*(3), 031914 (2013).
36. Tsutsui, K., Matsushita, T., Natori, K., Muro, T., Morikawa, Y., Hoshii, T., ... & Kinoshita, T. *Nano Letters*, *17*(12), 7533-7538(2017).
37. Yokoya, T., Terashima, K., Takeda, A., Fukura, T., Fujiwara, H., Muro, T., ... & Matsushita, T. *Nano Letters*, *19*(9), 5915-5919 (2019).
38. Chang, C. C. *Surface Science*, *25*(1), 53-79(1971).
39. Riviere, J. C. *Contemporary Physics*, *14*(6), 513-539(1973).

40. Palmberg, P. W., Bohn, G. K., & Tracy, J. C. *Applied Physics Letters*, *15*(8), 254-255(1969).
41. Ilyin, A. M. In *Microscopy Methods in Nanomaterials Characterization* (pp. 363-381) (2017). Elsevier.
42. Liu, J., Hembree, G. G., Spinnler, G. E., & Venables, J. A. *Ultramicroscopy*, *52*(3-4), 369-376 (1993).
43. D. T. Attwood, Soft X-rays and extreme ultaviolett radiation principles and applications, Cambridge Univ. Press 2000; https://juser.fz-juelich.de/record/134957/files/F4_Baumgarten.pdf.
44. Jackson, Daphne F., and David J. Hawkes. *Physics Reports* 70.3 (1981): 169-233.
45. Bunker,G. Introduction to XAFS: A Practical Guide to X-ray Absorption Fine Structure Spectroscopy (Cambridge University Press, Cambridge, 2010).
46. Schnohr, C.S., Ridgway, M.C. X-ray Absorption Spectroscopy of Semiconductors, Springer Series in Optical Sciences (Springer, Berlin, 2015).
47. Koningsberger, D. C., Prins,R. X-ray Absorption: Principles, Applications, Techniques of EXAFS, SEXAFS, and XANES (Wiley, New York, 1988)
48. Wang, M., Árnadóttir, L., Xu, Z. J., & Feng, Z. *Nano-Micro Letters*, *11*(1), 1-18(2019).
49. Kelly, S. D., Hesterberg, D., & Ravel, B. *Methods of soil analysis. Part 5. Mineralogical methods*, *5*, 387-464 (2008).
50. Karthieka, R. R., Begum, R. N., & Prakash, T. *Chinese Journal of Physics*, *71*, 643-650 (2021).
51. B.K. Teo and D.C. Joy, EXAFS spectroscopy Techniques and Applications (Springer Science +Business Media, New York, 1981).

52. Falkenberg, G., Pepponi, G., Streli, C., & Wobrauschek, P. *Spectrochimica Acta Part B: Atomic Spectroscopy*, *58*(12), 2239-2244 (2003).
53. Honma, T., Oji, H., Hirayama, S., Taniguchi, Y., Ofuchi, H., & Takagaki, M. (2010, June). In *AIP Conference Proceedings* (Vol. 1234, No. 1, pp. 13-16). American Institute of Physics.
54. Tröger, L., Arvanitis, D., Baberschke, K., Michaelis, H., Grimm, U., & Zschech, E. *Physical Review B*, *46*(6), 3283 (1992).
55. Tamenori, Y., Morita, M., & Nakamura, T. *Journal of Synchrotron Radiation*, *18*(5), 747-752(2011).
56. Suzuki, Y. *Physical Review B*, *39*(5), 3393(1989); Isomura, N., Murai, T., Oji, H., Nomoto, T., Watanabe, Y., & Kimoto, Y. *Applied Physics Express*, *9*(10), 101301(2016).
57. Nakanishi, K., & Ohta, T. *Surface and interface analysis*, *44*(6), 784-788(2012).
58. Isomura, N., Murai, T., Nomoto, T., & Kimoto, Y. *Journal of synchrotron radiation*, *24*(2), 445-448 (2017).
59. Kasrai, M. W. N. R. W. G. M. J. A., Lennard, W. N., Brunner, R. W., Bancroft, G. M., Bardwell, J. A., & Tan, K. H. *Applied Surface Science*, *99*(4), 303-312(1996).
60. Abbate, M., Goedkoop, J. B., De Groot, F. M. F., Grioni, M., Fuggle, J. C., Hofmann, S., ... & Sacchi, M. *Surface and Interface Analysis*, *18*(1), 65-69(1992).
61. D'Angelo, P., Benfatto, M., Della Longa, S., & Pavel, N. V. *Physical Review B*, *66*(6), 064209 (2002).
62. Jutimoosik, J., Sirisathitkul, C., Limmun, W., Yimnirun, R., & Noonsuk, W. *X‐Ray Spectrometry*, *46*(6), 492-496 (2017).
63. https://en.wikipedia.org/wiki/X-ray_absorption_spectroscopy.

64. Cheng, J., Chu, W., Liu, S., Dong, P., & Wu, Z. *Journal of Superconductivity and Novel Magnetism*, *27*(1), 9-15(2014).

65. Nomura, K. *Catalysts*, *9*(12), 1016 (2019).

66. Shikata, S., Yamaguchi, K., Fujiwara, A., Tamenori, Y., Yahiro, J., Kunisu, M., & Yamada, T. *Applied Physics Letters*, *110*(7), 072106 (2017).

67. Isomura, N., Kataoka, K., Watanabe, Y., & Kimoto, Y. *Japanese Journal of Applied Physics*, *58*(5), 051007 (2019).

68. Isomura, N., & Kimoto, Y. *Journal of Synchrotron Radiation*, *28*(4), 1114-1118 (2021).

69. (a)Rehr,J. J., Kas, J. J.and Vila, F. D. TIMES Lecture Series, SIMES-SLAC-Stanford(2017),https://web.stanford.edu/group/times/images/IIntro_to_XAS_Theory_TIMES1-17.pdf;(b)https://web.stanford.edu/group/times/images/II-Real_spaceMSTheory_TIMES1-17.pdf.

70. Rehr, J. J., Kas, J. J., Vila, F. D., Prange, M. P., & Jorissen, K. *Physical Chemistry Chemical Physics*, *12*(21), 5503-5513(2010).

71. Rehr, J. J., & Albers, R. C. *Reviews of modern physics*, *72*(3), 621(2000).

72. Rehr, J. J.; Kas, J. J.; Prange, M. P.; Sorini, A. P.; Takimoto, Y.; Vila, F. C. R. Phys. 10, 548−559 (2009).

73. https://feff.phys.washington.edu/feff/Docs/feff9/feff90/feff90_users_guide.pdf

74. https://millenia.cars.aps.anl.gov/webatoms/?file=atoms.inp

75. Saha, B., & Chakraborty, P. (2013). *Energy Procedia*, *41*, 80-109.

76. Vickerman, J. C. *ToF-SIMS: surface analysis by mass spectrometry*, 1-40(2001).

77. Graham, D. J., & Castner, D. G. *Biointerphases*, *7*(1), 49 (2012).

78. Thirumavalavan, S., Mani, Y., & Suresh, S. S. *JOURNAL OF NANO- AND*

ELECTRONIC PHYSICS, Vol. 7 No 4, 04024(4pp) (2015).

79. https://d347awuzx0kdse.cloudfront.net/vicomaus/content-file/1kw-60641_van_der_pauw_resistivity_hall_voltage_4200a-scs_an_vicom.pdf
80. Castro, H., Galvis, J., & Castro, S. *IEEE Transactions on Instrumentation and Measurement*, *60*(1), 198-205(2010).
81. Rietveld, G., Koijmans, C. V., Henderson, L. C., Hall, M. J., Harmon, S., Warnecke, P., & Schumacher, B. *IEEE transactions on instrumentation and measurement*, *52*(2), 449-453(2003).
82. *Van der Pauw, L.J. Philips Research Reports.* ***13****: 1–9* (1958).
83. https://en.wikipedia.org/wiki/Van_der_Pauw_method
84. Coenen, T., & Haegel, N. M. *Applied Physics Reviews*, *4*(3), 031103 (2017).

Chapter 3 Direct Observation of Atomic Structure and Chemical State for Active Dopant Site in Mg-Doped GaN (0001)

3.1 Introduction.

GaN has many unique properties such as a wide direct band gap and high thermal conductivity.[1−10] GaN is used in high-temperature, high-power devices.[11−16] In such applications, proper doping is necessary to prepare GaN-based MOS-FET structures where carrier control of the source, drain, and the gate is crucial.[17−19] In order to prepare high-quality GaN-based MOS-FET structures, the atomic structures and chemical states in active and inactive dopant sites in GaN should be clarified. Once the atomic structures and the chemical states of inactive dopant sites are clarified, we can have a strategy that vanishes or reduces the inactive sites of dopants. In the case of n-type GaN, Si is widely used to form the shallow donor states in the band gap of GaN.

In the case of p-type GaN, Mg is usually used due to the formation of shallow acceptor levels in the band gap of GaN. For the atomic structures and the chemical states of the Mg dopant in Mg-doped GaN, various doping sites have been proposed in the previous studies.[20−26]Various approaches have been attempted to clarify the atomic structures and chemical states of the active and inactive dopant sites in Mg-doped GaN. In the case of X-ray diffraction, the atomic structures of dopants cannot be obtained due to the lack of periodicity with such dopants. Atom tomography shows the three-dimensional dopant distributions in the film.[27,28] However, the chemical information on a dopant cannot be detected. Nevertheless, in the case of extended X-ray absorption fine structure and X-ray absorption near edge structure, they could provide information about the coordination number, the bond length between Mg and the surrounding atoms, and the unoccupied states of the Mg-dopant.[29] However, the energy ranges of resonant

absorption for the Mg K-edge and Ga L-edge overlap each other, showing little information on the Mg-dopant. High-resolution scanning transmission electron microscopy (TEM) can clarify the atomic arrangement of the dopants in real space.[30] However, the detection of elements with a low atomic number is difficult. In addition, the chemical information on a dopant is hardly ever detected. TEM and electron energy loss spectroscopy (EELS) can be used to detect dopant atoms with surrounding local atomic structures in real space. However, the loss spectra of TEM-EELS exhibit average information on the electronic states as electrons pass through the samples.[31] In addition, since the loss spectra of TEM-EELS show a large background, the quantitative analysis is very difficult.[32,33] The cross sections of edge absorption on the electrons are very small.[34] Thus, high-density electrons are needed, which causes some damage to the sample.

Atomic structures and chemical states in active and inactive sites of the Mg dopants in GaN have not been directly clarified yet. Thus, a direct method is needed to clarify both of chemical states and atomic structures of the active and inactive dopant states in Mg-doped GaN.

PEH was employed to obtain the 3D local atomic structure of the Mg dopant in GaN. For PEH, photoelectrons of the target atoms (e.g., dopants) are excited under photoirradiation as the emitter, and then they are scattered by the surrounding atoms. Finally, the interference patterns are formed in the core-level photoelectron angular distribution.[35] PEH has a great advantage in which nonperiodic atomic structures are applicable. Additionally, since PEH is based on PES, the chemical-state-discriminated PEHs can be achieved. Therefore, the atomic structures and chemical states of the active and inactive dopant sites could be clarified. By adopting the experimental PEH and the

scattering pattern extraction algorithm (the maximum entropy method/L1 regularization (SPEA-MEM/ SPEA-L1) method),[36–42] it is possible to experimentally visualize the local 3D atomic structure around the dopant atoms. Using PES and PEH, one can obtain a direct method to analyze the atomic structure and chemical states of Mg dopants in Mg-doped GaN.

The schematic of this PEH is shown in Fig. 3.1. Here, the atomic structures and chemical states of the active and inactive Mg-dopant sites for Mg-doped GaN were investigated.

3.2 Experimental

3.2.1 Sample preparation.

Mg-doped GaN was prepared by the hydride vapor phase epitaxy method, the epitaxial layer with a thickness of 0.1 μm was grown on GaN (0001) substrates

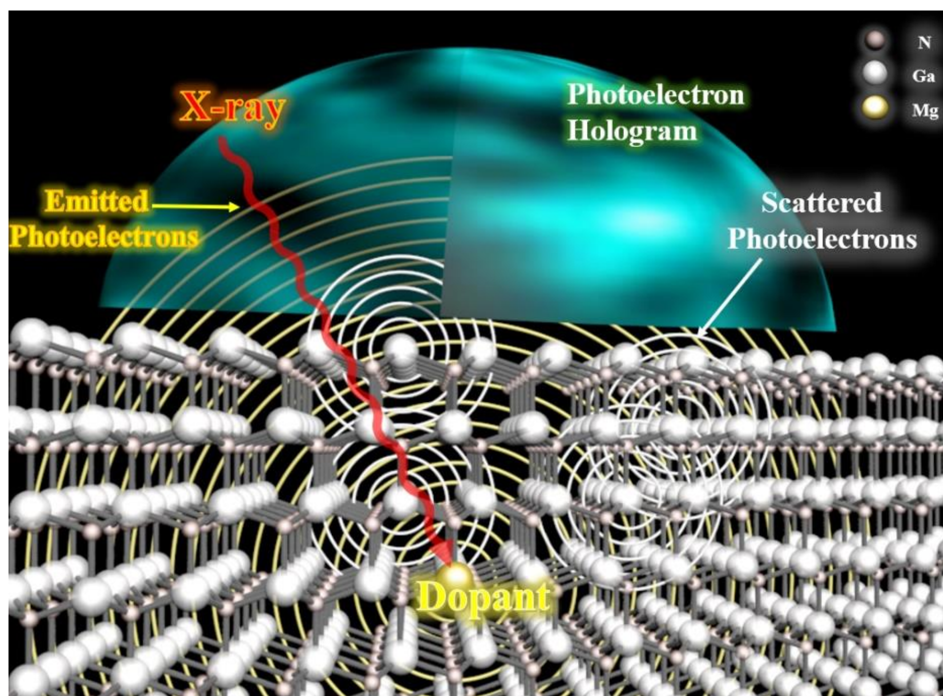

Figure 3.1: Schematic of PEH in the case of Mg-doped GaN. The yellow, white, and grey balls represent Mg, Ga, and N atoms, respectively.

(10^8 Ωcm) at 1100 °C; GaCl (HCl reacts with Ga), NH_3, and bis-cyclopentadienyl magnesium were used as Ga, N, and Mg sources, respectively. The epitaxial layer with a thickness of 0.1 μm was used because of its reproducibility of Mg concentration. According to the sample providers, Cl (impurity) was not detected by SIMS (below the detection limit of 10^{16} cm^{-3}). X-ray diffraction rocking curves of on-axis (0002) and off-axis ($10\bar{1}2$) exhibit 55 and 56 arcsec, respectively. The threading dislocation density (mixture of screw and edge) was estimated to be 1.0×10^6 cm^{-2}, which was evaluated by cathodoluminescence mapping based on scanning electron microscopy. Thus, the threading dislocation can be ignored in the present experiments. The depth profile of the carbon content in the film using Auger electron spectroscopy exhibited a value lower than the detection limit (0.01 at %). Thus, the carbon content in the film for the present sample is ignored.

3.2.2 Secondary-ion mass spectrometry (SIMS).

The relationship between the Mg dopants concentration and depth was analyzed by SIMS measurements. PHI-ADEPT1010 was used for SIMS measurements. Cs-positive ions with 3 keV were employed as the ion source. The elements concentration conversion is based on sensitivity in GaN. Charge compensation was not used during the measurements.

3.2.3 Hall effect measurements.

The Hall effect measurements with Van der Pauw method were performed to measure the mobility and carrier concentration. Four square-shaped gold sheets with a side length of about 2 mm are deposited on the four corners of the Mg-doped GaN as electrodes. The magnetic field strength was 0.48 or 0.55 Tesla.

3.2.4 Cathodoluminescence (CL).

CL was used to investigate the energy level of Mg-doped GaN. CL measurements were performed using a HORIBA MP32 CL system attached to a Hitachi SU6600 field-emission scanning electron microscope (FE-SEM). The accelerating voltages of 3 and 5 kV were used. CL measurements were performed at room temperature and 80K.

3.2.5 X-ray photoelectron spectroscopy (XPS) and Auger electron spectroscopy (AES).

XPS and AES measurements were performed using PHI Quantes (ULVAC-PHI). Monochromatic Al Kα (1486.7 eV) was used as the incident X-ray.

3.2.6 Photoelectron holography (PEH).

The PEH measurements were performed at the BL25SU in SPring-8.[36,42] The base pressure of the main chamber was 2.8×10^{-8} Pa. Scienta-Omicron DA30 was used as an electron analyzer.[43] The electron analyzer had a 2D detector which covered an azimuthal angle of ±15° and a polar angle of ±10°. The angle between the direction of the electron analyzer and the incident soft X-ray beam was 90°. The incident photon energies (910 and 854 eV for Ga 3p and Mg 2p, respectively) were selected so as to become kinetic energy of ~800 eV for the PEH simulations in the present PEH experiments. The PEH images were obtained by measuring the entire azimuth angles and the entire polar angle of the present sample. For the PEH simulations, the SPEA-L1 algorithm was used to obtain the atomic image reconstruction. Note that the information depth of the photoelectrons was estimated to be 4.8 nm, which was calculated by using a TPP-2M formula.[44] Thus, the present measurements exhibit relative near-surface information.

3.3 Results and discussion

3.3.1 SIMS measurements.

Figure 3.2 shows the SIMS for Mg dopant in Mg-doped GaN with lower and higher Mg concentrations. From the SIMS result in Fig. 3.2, the Mg concentration is estimated

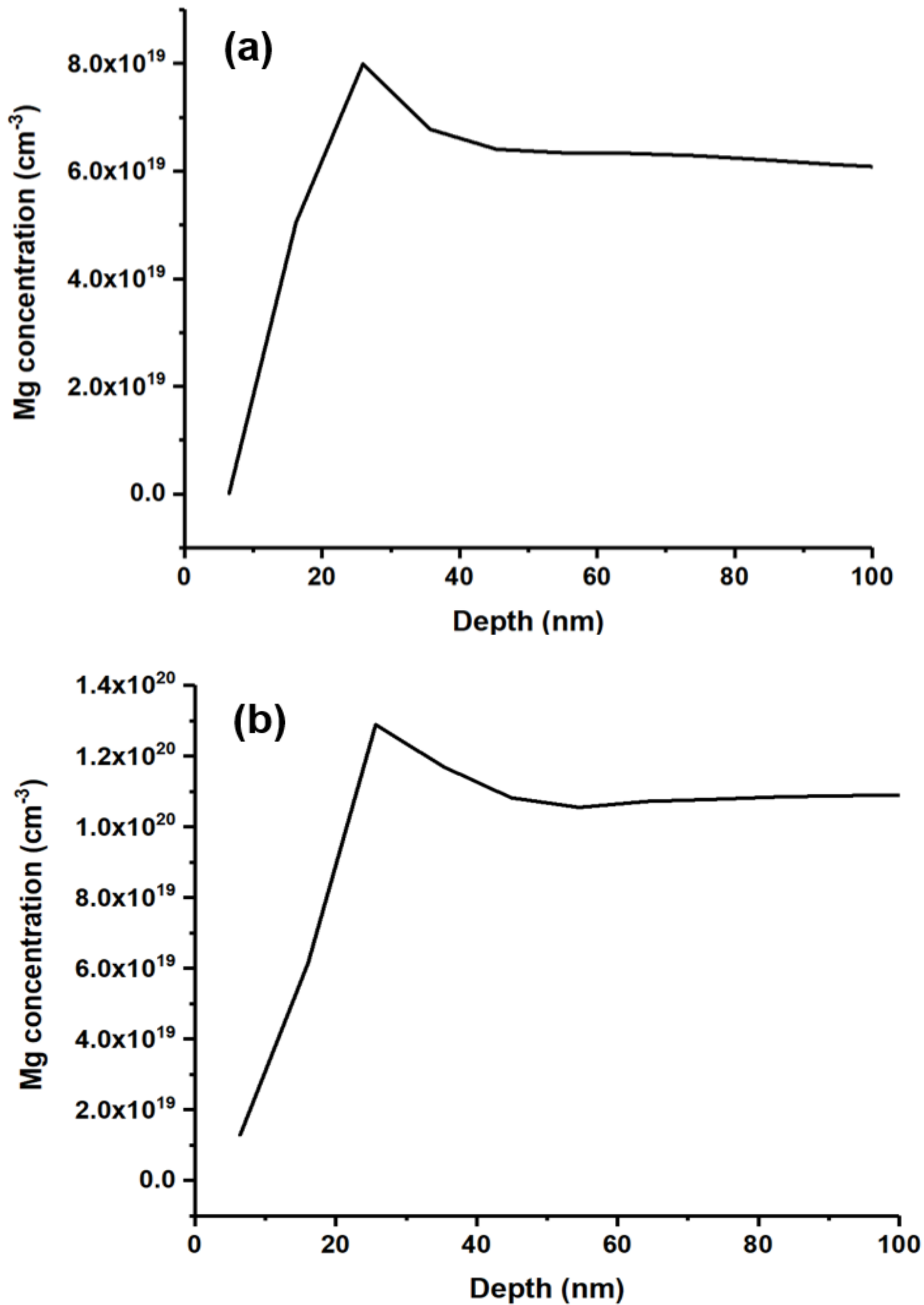

Figure. 3.2. SIMS for Mg-doped GaN (a) lower Mg dopant concentration; (b)higher Mg dopant concentration.

to be 6.0×10^{19} cm^{-3} in the case of the lower Mg concentration while in the case of the higher Mg concentration, the concentration is ~1.1×10^{20} cm^{-3}.

Hall effect measurements showed that the resistivity, mobility, and carrier concentration before annealing for Mg-dopant concentration of ~1.1 x10^{20} cm^{-3} was 1.2 Ω.cm, 1.2 cm^2/ V.s, and 4.6 × 10^{18} cm^{-3}, respectively. In the case of Mg-dopant concentration of ~1.1 x10^{20} cm^{-3} GaN after annealing, the resistivity, mobility, and carrier concentration are 4.47 x 10^{-1} Ω.cm, 5.34 cm^2 / V.s and 2.6 x 10^{19} cm^{-3}, respectively. In the case of Mg-dopant concentration of 6.0 x10^{19} cm^{-3}, on the other hand, the resistivity, mobility, and carrier concentration before annealing are 1.2 Ω.cm, 5.6 x 10 cm^2 / V.s, and 9.2 × 10^{16} cm^{-3}, respectively. After annealing, the resistivity, mobility, and carrier concentration are 2.1 Ω.cm, 7.1 x 10^{-1} cm^2 / V.s, and 4.1 × 10^{18} cm^{-3}, respectively.

3.3.2 AES measurements.

To analyze the chemical state of Mg dopants in Mg-doped GaN, AES measurements were performed. Figures 3.3 (a) and (b) show AES spectra for Mg dopants in Mg-doped GaN with the lower Mg concentration (6.0 x $10^{19}$$cm^{-3}$) and the higher Mg concentration (1.1 x 10^{20} cm^{-3}), respectively. As can be seen, AES spectrum for the lower Mg concentration does not show a sufficient S/N ratio to analyze. AES spectrum for the higher Mg concentration, on the other hand, shows a sufficient S/N ratio to analyze. Therefore, the higher Mg dopant concentration in GaN (1.1 x 10^{20} cm^{-3}) was only used in the present study.

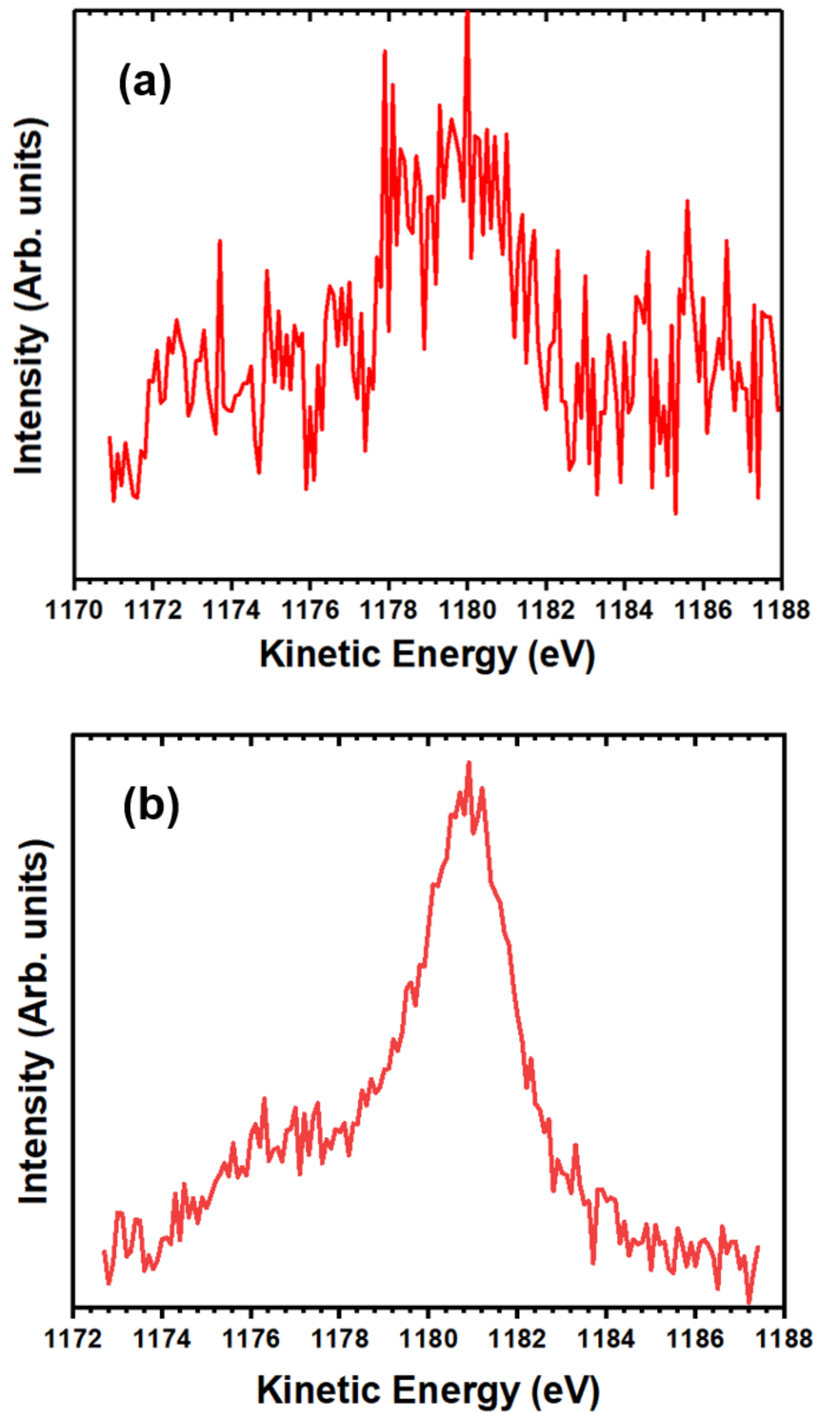

Figure. 3.3. AES spectra for (a) lower Mg dopant concentration; (b) higher Mg dopant concentration.

3.3.3 SEM and CL measurements.

Figure 3.4 shows SEM and CL for Mg-doped GaN. SEM image indicates that after annealing the surface of Mg-doped GaN is relatively flat and uniform. Figure 3.4 (b) shows CL mapping with 433 nm (2.86 eV) at the same location in SEM. The strong emission centered at 2.86 eV both at RT and low temperature is observed. This peak is attributed to the transition of Mg substituting Ga (Mg_{Ga}) to nitrogen vacancy (N_V).[45-47] This indicates that Mg_{Ga} and N_V are predominantly formed in the present samples.

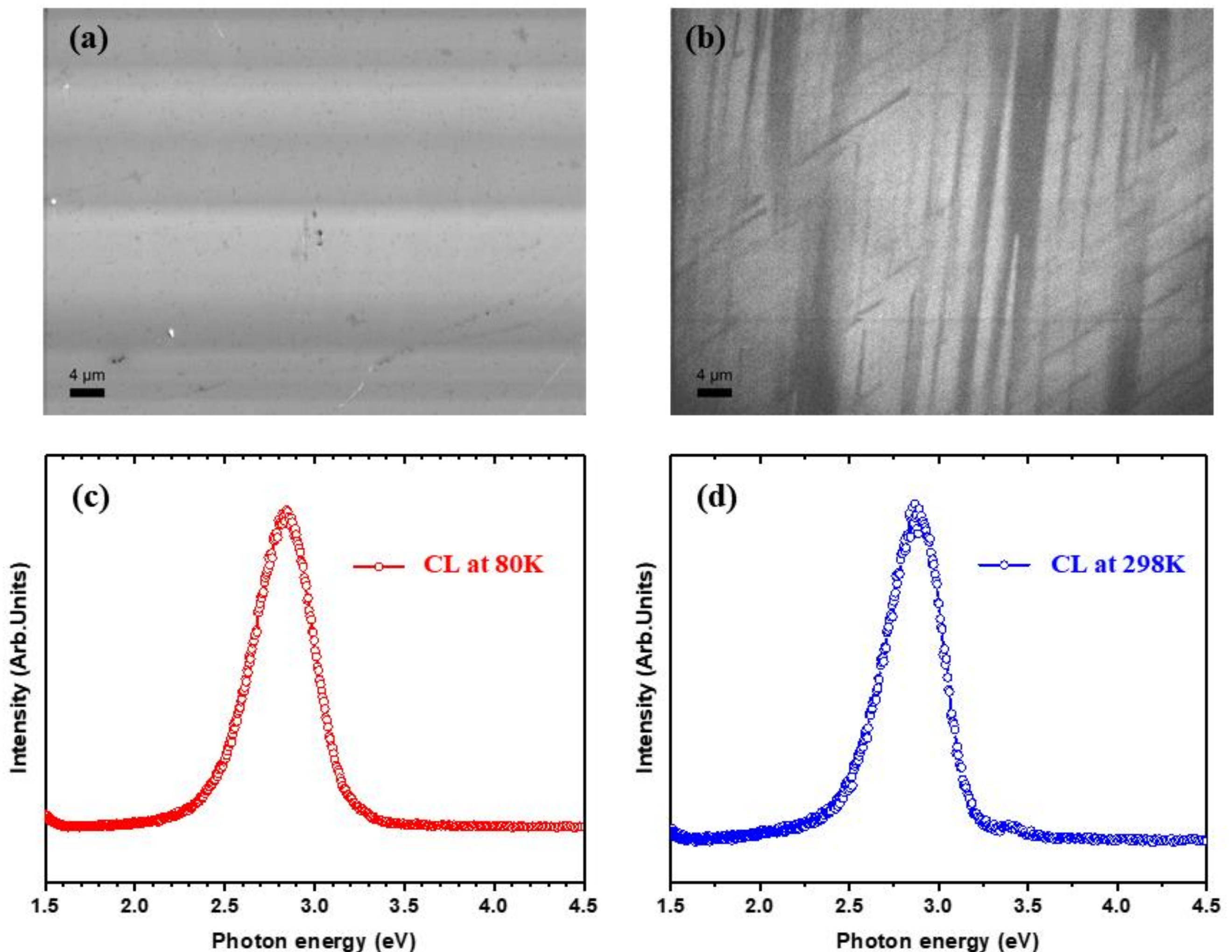

Figure 3.4: (a) SEM for Mg-doped GaN after annealing. (b) cathodoluminescence (CL) mapping with 433 nm (2.86 eV) at the same location in SEM. (c) low-temperature CL spectrum (~80 K) for the Mg-doped GaN with an emission centered at 2.86 eV d. (d) room-temperature CL spectrum (~298 K) for the Mg doped GaN. An emission centered at 2.86 eV can be also observed.

3.3.4 XPS and AES measurements.

Figure 3.5 (a) shows the Mg-KLL Auger spectra (AES) of Mg-doped GaN at room temperature (RT) and after annealing at 800 °C, the sample. In the AES spectra, two peaks are clearly observed; peak α and peak β. At RT, peak α is the major component. After annealing at 800 °C, the areal intensity of peak β increases while that of peak α decreases. According to previous studies, high-temperature annealing can activate a part of the inactive dopant sites, increasing the hole concentration. Therefore, peak β should be the active site of the Mg-dopant. Figure 3.5 (b) shows Mg 2p XPS spectra of Mg-doped GaN at room temperature (RT) and after annealing at 800 °C. In the spectra, two peaks are clearly observed; peak α and peak β. At RT, peak α is the major component. After annealing at 800 °C, the areal intensity of peak β increases while that of peak α decreases.

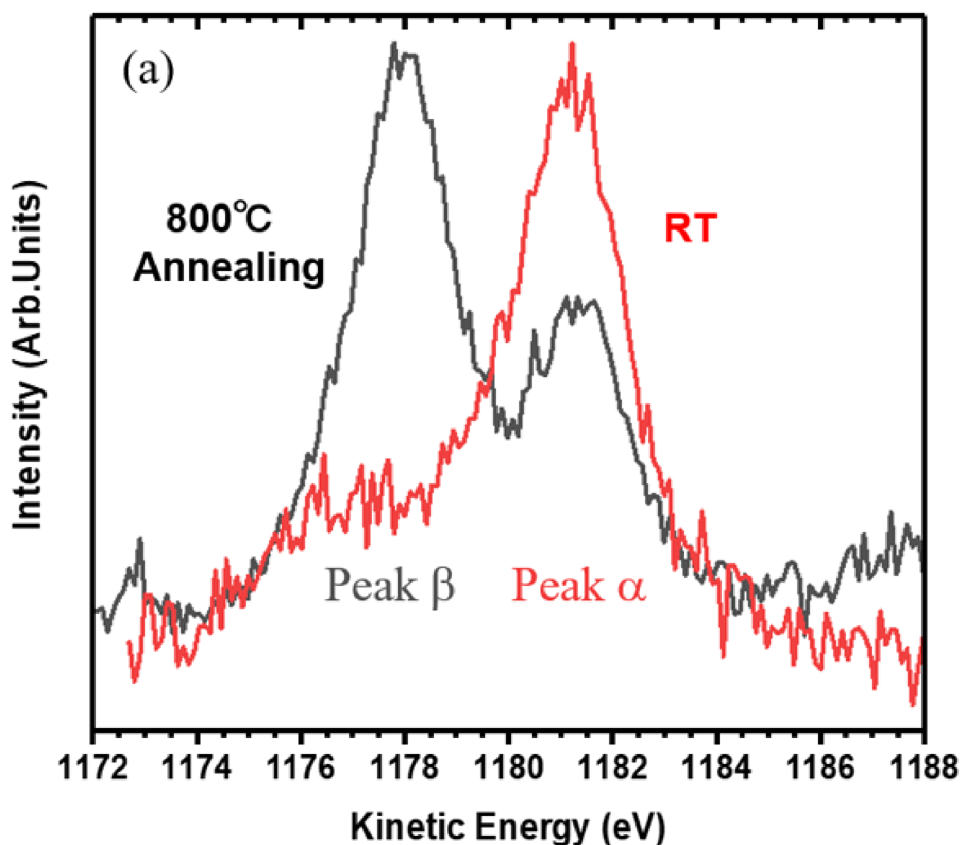

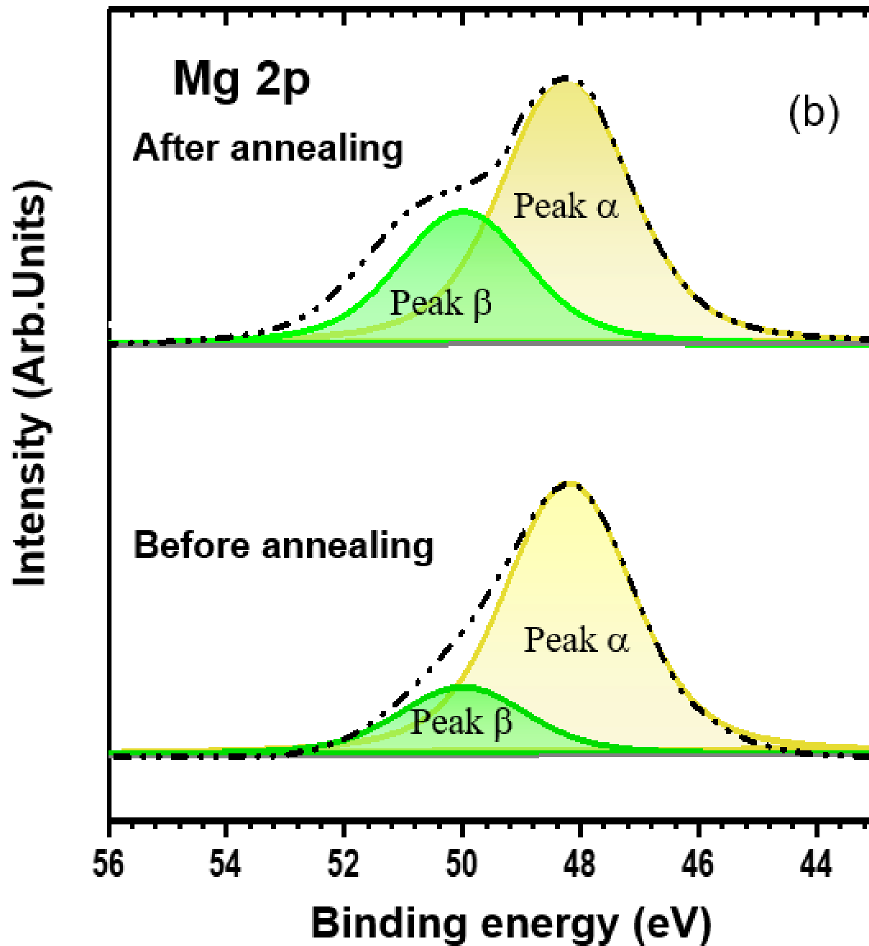

Figure 3.5: (a) Mg KLL Auger spectra of Mg-doped GaN at RT (red line) and after annealing 800 °C; (b) Mg 2p XPS spectra in Mg-doped GaN before and after the annealing at 800 °C.

According to previous studies, high-temperature annealing can activate a part of the inactive dopant sites, increasing the hole concentration.[21,22] This is consistent with present results in which the hole concentration is increased after annealing. According to a previous study, the peak position of components β is due to the active site because hole mobility became higher after annealing.[48] Therefore, peak β should be the active site of the Mg-dopant. The atomic structure and the chemical states of peak α is discussed later.

3.3.5 PEH.

Figure 3.6 (a) shows the experimental Ga 3p PEH measured at a kinetic energy of ~ 800 eV (left) and the simulated Ga 3p PEH (right) in GaN. Note that, for the simulated Ga 3p PEH, a clustered atomic structure for GaN with a 10 Å radius was employed. For the experimental Ga 3p PEH, the strong regions around specific portions are attributed to the M plane ($10\bar{1}0$ face) and A plane ($11\bar{2}0$ face) in the single-crystal GaN structure. The strong spots due to forward focusing correspond to the direction of scattered atoms. The Kikuchi lines can be clearly seen (Fig. 3.6 (a)). From these results, simulations reproduce the Ga 3p PEH quite well. Figure 3.6 (b) presents the crystal structure of GaN, where the emitter of Ga atoms is indicated. From the observed GaN PEH, slices in the atomic structure for various cross cross-sections on the distance to the emitter plane are prepared as shown in Fig. 3.6 (c). The reconstructed atomic images obtained from the planes are shown in Fig. 3.6(d)−(f). Since the reconstructed atomic images of the Ga atoms appear in the yellow circles of the figure's, the reconstructed atomic image should come from the Ga atom site. The same phenomena are observed in planes of 2.6 and 5.2 Å. Although there is some missing amplitude or reductions away from the center, this is mainly due to the attenuation of photoelectron waves with increasing distance.[44]

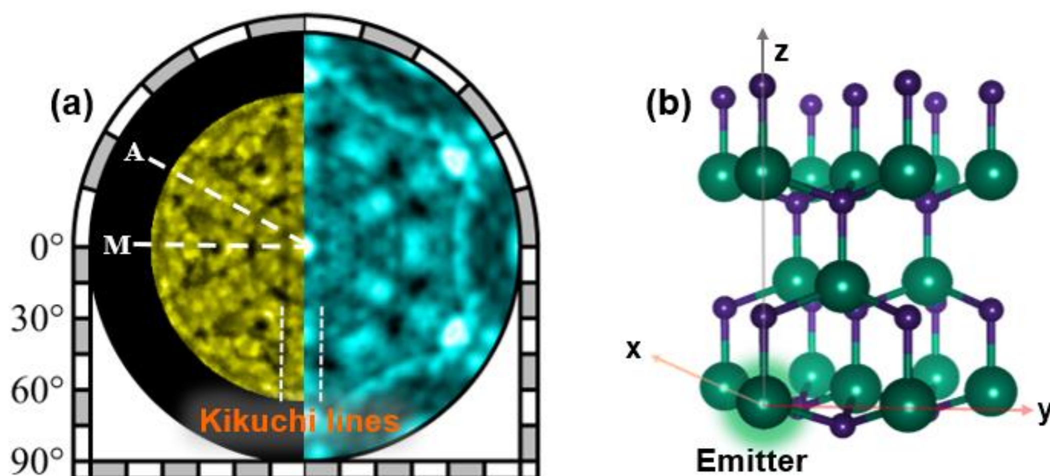

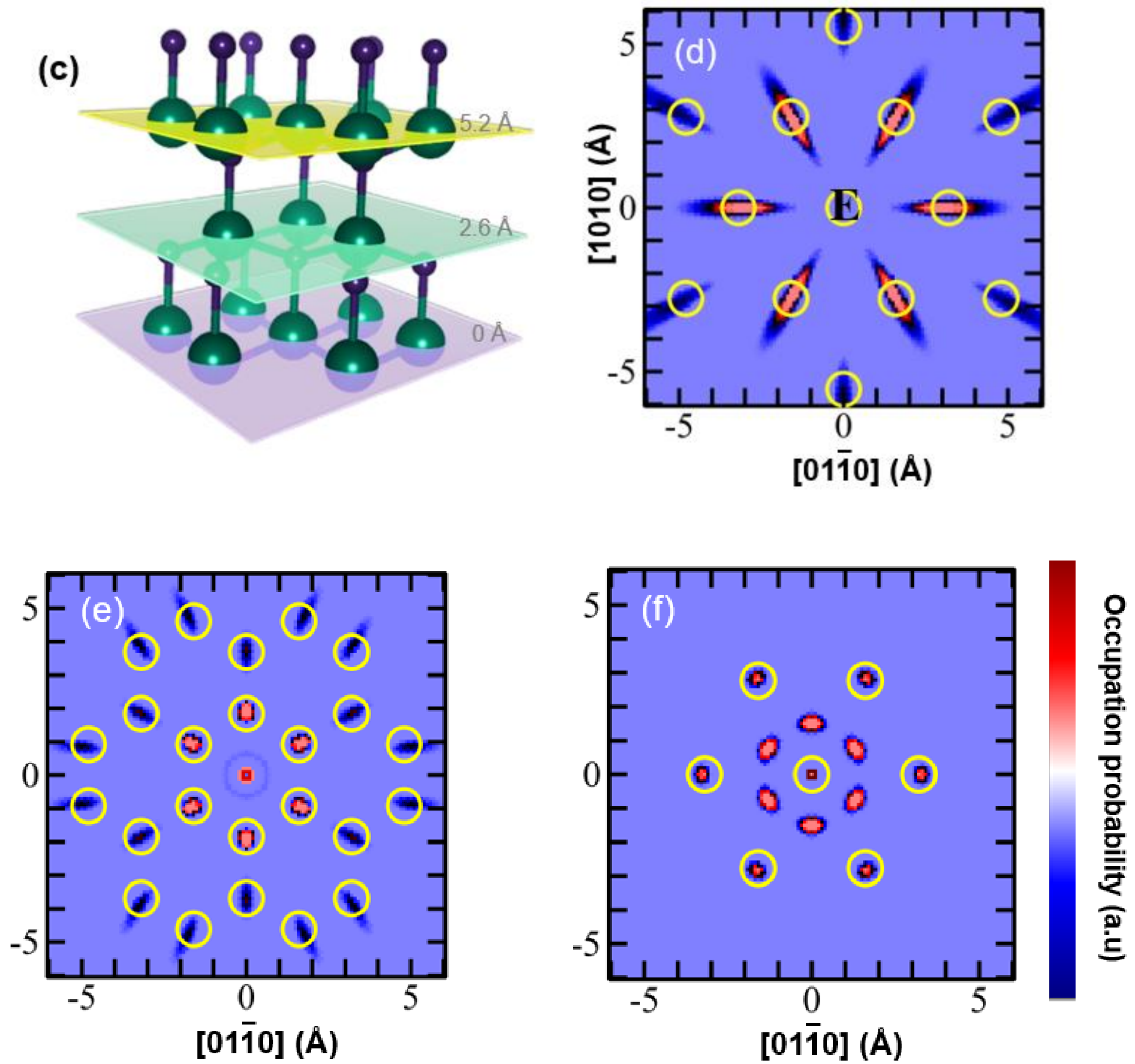

Figure 3.6: (a) experimental (left) and simulated (right) images of Ga 3p PEHs. (b) GaN atomic structure where Ga acts as an emitter. (c) slices of GaN structure with various distances (0, 2.6 and 5.2 Å) from the emitter plane. (d)-(f) slices of the reconstructed atomic images with various distances (0, 2.6 and 5.2 Å, respectively) from the emitter. The yellow circles indicate the expected position of Ga atoms.

Figure 3.7 shows the intensity as a function of the polar angle (from 0 to 63° in intervals of 7°). The intensity of the component β depends on the polar angle, indicating that the interference should be observed.

Figure 3.8 (a) shows the Mg 2p PES for the Mg-doped GaN after the annealing at 800 °C, where the incident photon energy is 854 eV. For the peak fitting of Mg 2p PES, the spin−orbit splitting of 0.28 eV was employed.[49,50] By measuring all azimuth angles and polar angles of components α and β, the corresponding PEHs are obtained as shown in Figs. 3.8 (b) and (c). The simulated PEH of an Mg atom substituting a Ga atom in the Mg-doped GaN structure (Mg_{Ga}) is also shown in Fig. 3.8(d).

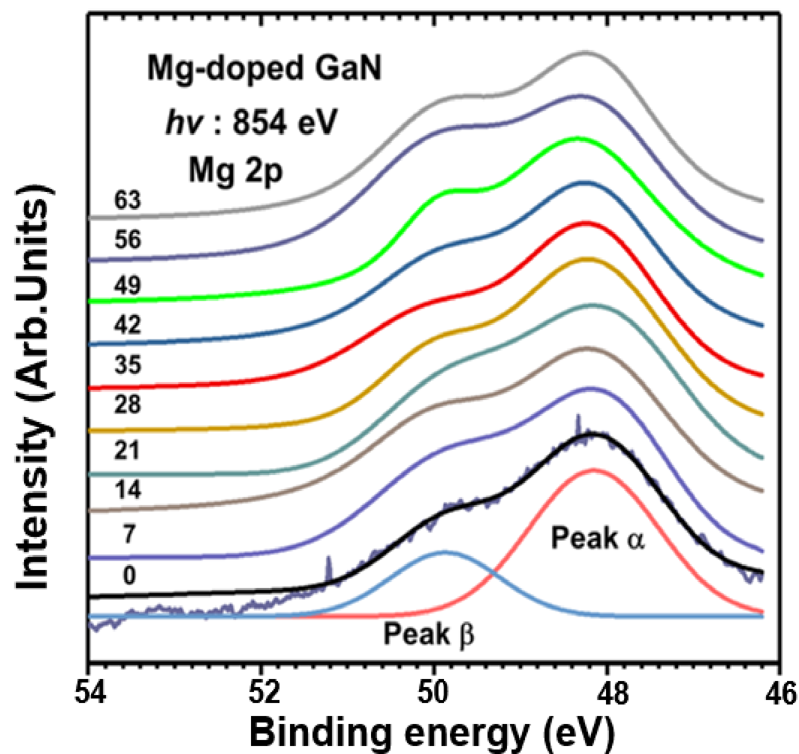

Figure.3.7: Photoelectron spectra of Mg 2p at azimuth angle 0°with respect to M plane in Mg-doped GaN, the interval is 7°. The observed two peaks in Mg 2p are labeled peak α and peak β, respectively.

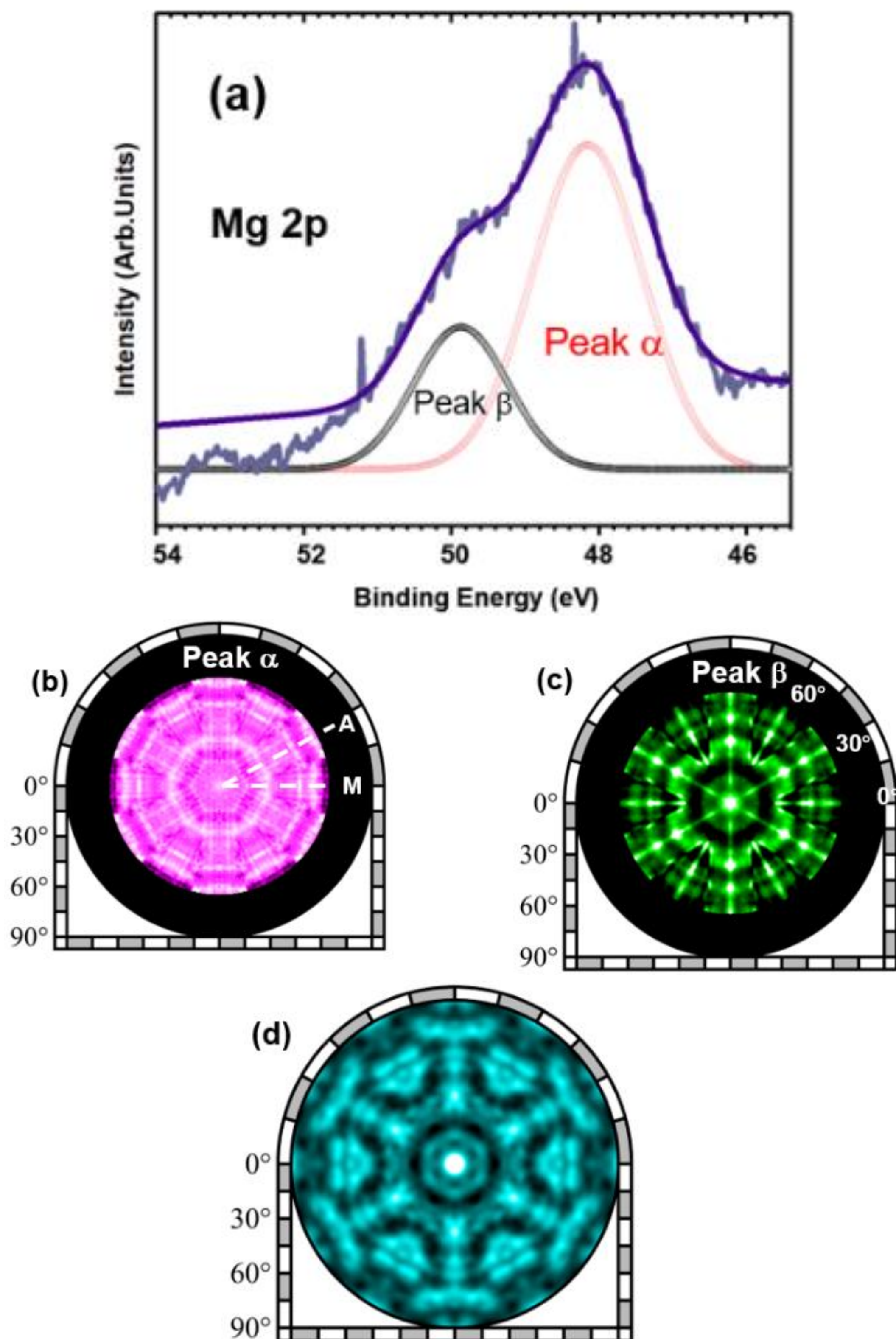

Figure 3.8: (a) Mg 2p PES. Experimentally observed Mg 2p PEHs for (b) component α and (c) component β, respectively. (d) simulated PEH of Mg_{Ga} in GaN.

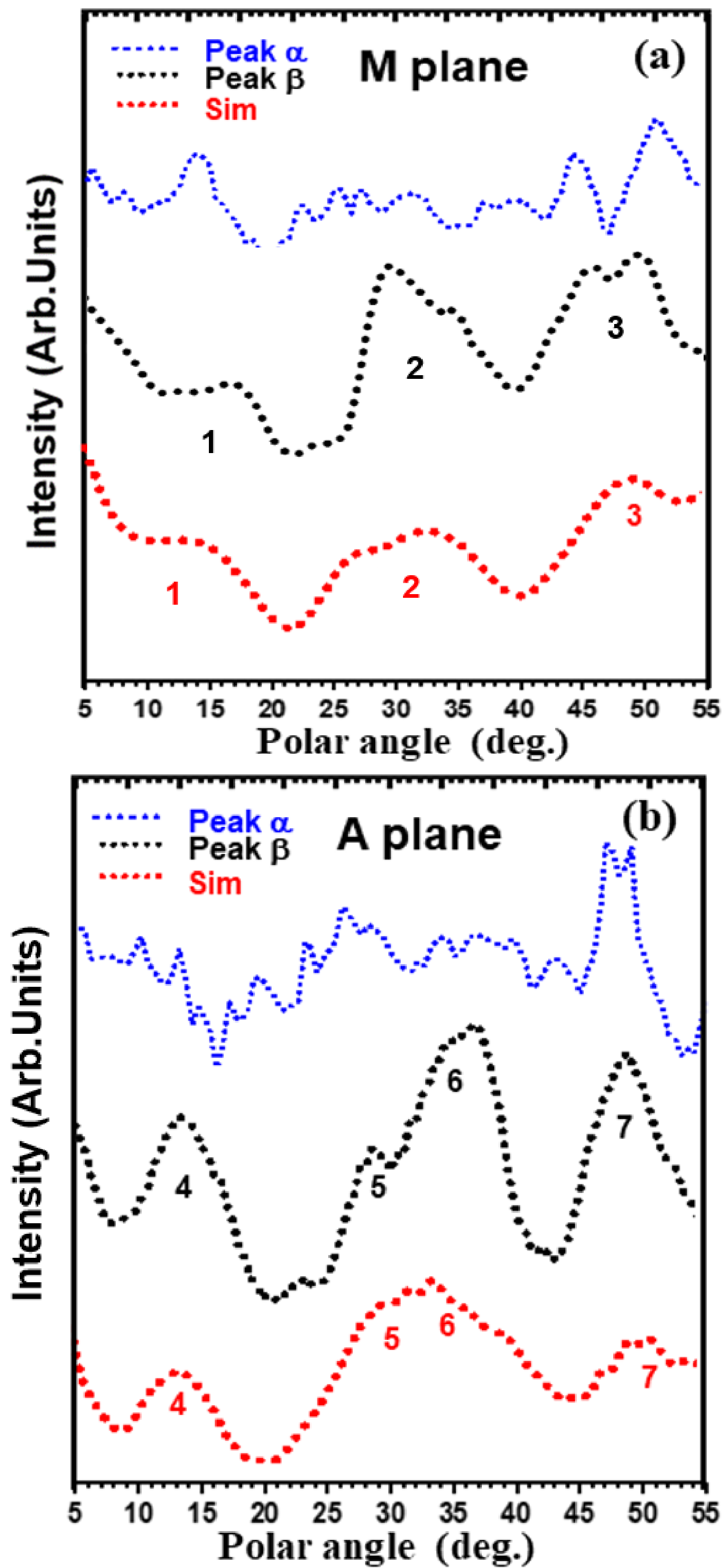

Figure.3.9: Line profiles in M and A planes for peak α, peak β, and simulated hologram of Mg_{Ga}.

Figure 3.9 shows the intensity of peak α, peak β, and simulated hologram of Mg-doped GaN as a function of polar angle for M and A planes. In the case of M plane (Fig. 3.9(a)), the intensity line profile of the component α exhibits only weak structures. For component β, on the other hand, three main peaks can be observed, namely peak 1(~15°), peak 2(31°), and peak 3 (~50°). The intensity line profile of simulated hologram (Mg substituting Ga in GaN) shows four peaks for A plane, which exhibits similar peak positions to the experimental one of label β.

Figure 3.10 shows the atomic structure of M plane where the arrows represent the forward scattering form the emitter (Mg in Ga site). The peak 1(1') (~15°) comes from forward scattering with the Ga and N atoms. Peak 2 (~31°) with a broad peak is mainly

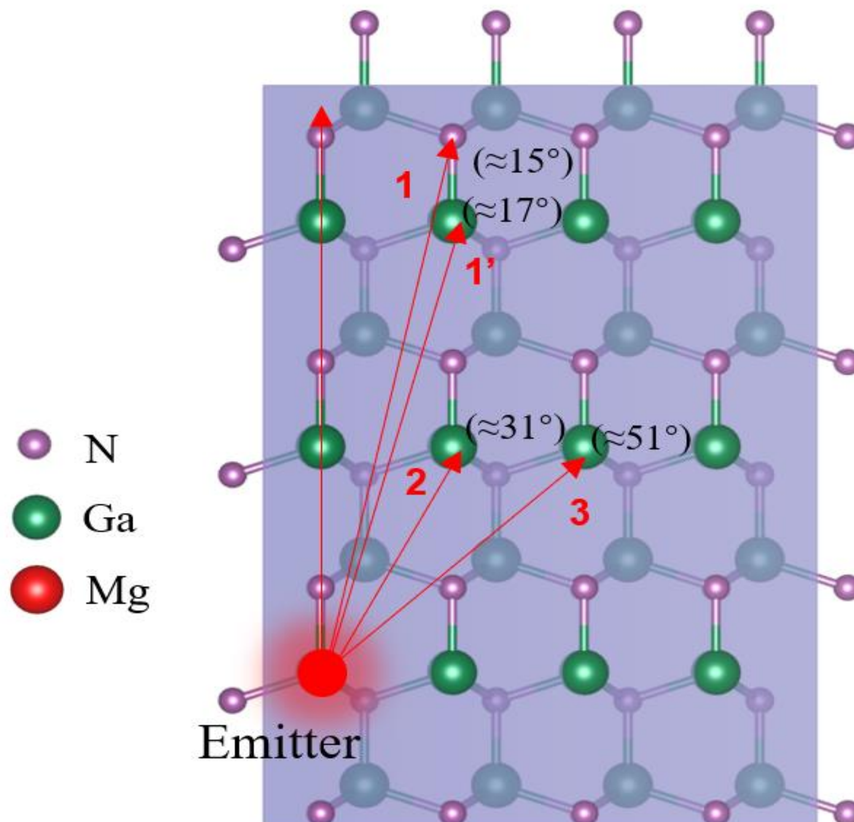

Figure.3.10: Atomic structure in the M-planes. The arrows indicate forward scattering to explain the observed photoelectron holograms.

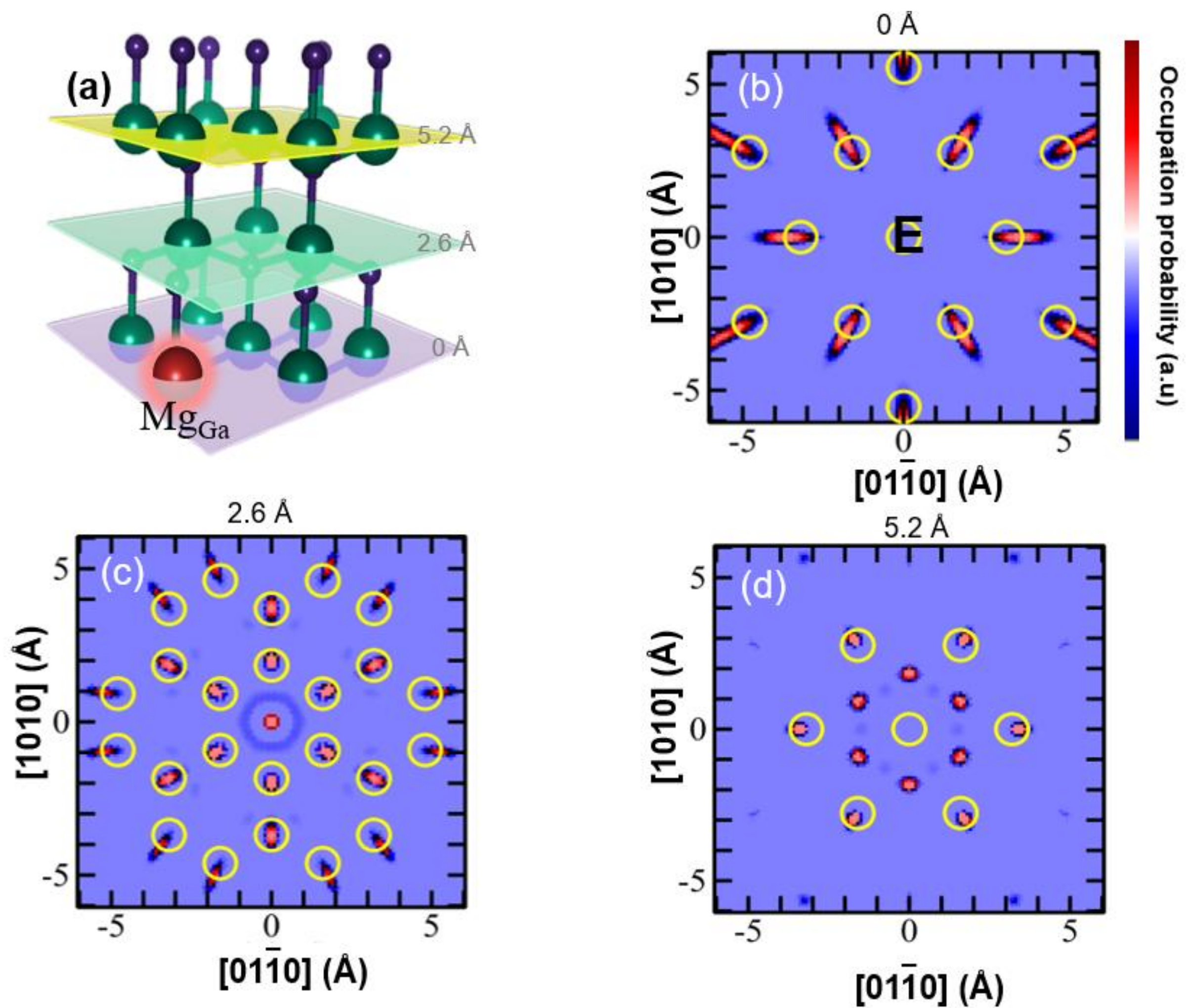

Figure 3.11: (a) slices of GaN structure with various distances (0, 2.6 and 5.2 Å) from the emitter plane. Mg (red ball) acts as an emitter. (b)-(d) slices of the reconstructed atomic images with various distances (0, 2.6 and 5.2 Å, respectively) from the emitter. The yellow circles indicate the expected position of Ga atoms.

from Ga atom scattering. The origin of peak 3 (~50°) is also marked in the Fig. 3.10. Thus, observed peaks in Fig. 3.9 are due to forward scattering form the Mg atom emitter.

Slices in the atomic structure for cross sections are shown in Fig. 3.11 (a). As can be seen, component α does not have any clear hologram patterns or Kikuchi lines, whereas component β exhibits clear hologram patterns and Kikuchi lines. Figures 3.11 (b)−(d)

show reconstructed atomic images of Mg_{Ga} obtained from the cross sections in Fig. 3.5 (a). The reconstructed atomic images of component β appear nearly inside those yellow circles obtained from the simulations for Mg_{Ga}. Since component β is the active site in Mg-doped GaN, Mg_{Ga} should be the active site in Mg-doped GaN.

Next, the atomic structure and the chemical state of the component α are discussed. Considering the reaction of this study, ammonia gas was used as one of the reactive substances. Thus, hydrogen atoms are introduced into the GaN substrates. In this case, H atom may bond with Mg_{Ga}, forming Mg_{Ga}−H complex. This conclusion is consistent with the previous studies.[20] In the present study, after annealing at 800 °C, the areal intensity of peak β increases while that of peak α decreases. Therefore, an H atom in Mg_{Ga}−H may be dissociated upon annealing, forming Mg_{Ga}. Thus, Mg-H may be an inactive component. This is consistent with peak position of the component α having lower binding energy because component α has less N bonds than the component β; N shows higher electronegativity than H. Based on these results, several possibilities are discussed for the atomic structures of component α: The first is a disordered structure. Mg_{Ga}−H structure with random rotation was used for the simulation where the PEH is shown in Fig.3.12(a).

The second is that according to previous reports,[23,52] H atoms can be located at a variety of positions. However, these structures did not represent the experimental PEH of the component α.

The third is that two H atoms are located at A or M plane where the atomic structure is shown in Fig. 3.12(b). The simulated PEH, which is shown in Fig. 3.12(c), is in relatively good agreement with the experimental PEH of the component α.

From these discussions describe above, one proposes the atomic structure of

component α Mg-H component where two H atoms are located at A or M plane.

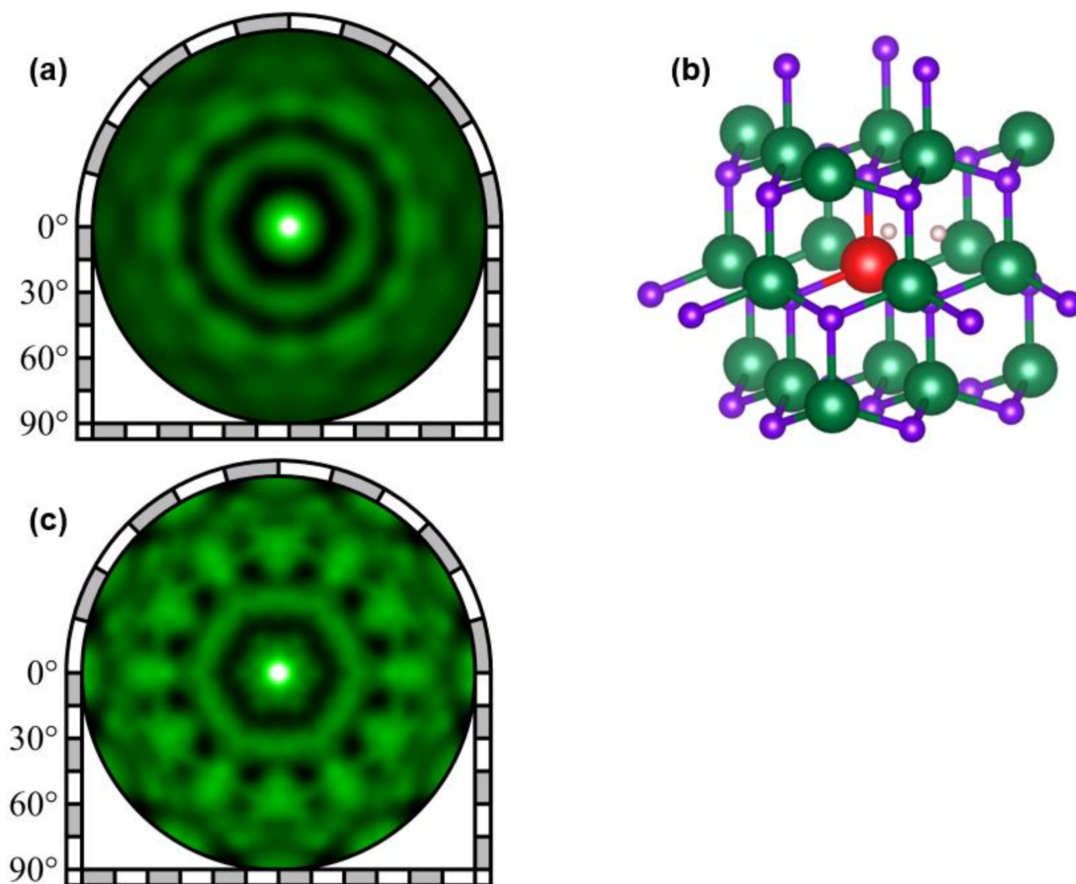

Figure 3.12: (a) simulated PEH of Mg_{Ga}−H structure with random rotation; (b) atomic structure in which two H atoms in Mg_{Ga}−H complex are located in A or M plane;(c) PEH of (b).

3.4 Conclusion

XPS, AES, PES, and PEH were used to clarify the atomic structures and chemical states in the active and inactive dopant states of Mg-doped GaN. Comparing Mg 2p XPS spectra in Mg-doped GaN before and after annealing, it was found that one chemical state was attributed to the active state in Mg-doped GaN while the other chemical state corresponded to the inactive state in it. Using PEH, the active state is attributed to Mg_{Ga} in the Mg-doped GaN structure. On the contrary, the inactive state originated from a Mg_{Ga}−H structure in the Mg-doped GaN.

Based on this study, a strategy is proposed to increase the carrier concentration. By adjusting the appropriate annealing temperature, the proportion of active doping can be increased to further increase the carrier concentration.

3.5 References

1. Pankove, J. I. *Mater. Sci. Eng., B*. 61, 305−309 (1999).

2. Morkoc, H.; Strite, S.; Gao, G. B.; Lin, M. E.; Sverdlov, B.; Burns, M. *J. Appl. Phys.*76, 1363−1398 (1994).

3. Kawashima, T.; Yoshikawa, H.; Adachi, S.; Fuke, S.; Ohtsuka, K. *J. Appl. Phys.* 82, 3528− 3535 (1997).

4. Pearton, S. J.; Zolper, J. C.; Shul, R. J.; Ren, F. *J. Appl. Phys.* 86, 1−78 (1999).

5. Huang, X.; Liu, Z.; Li, Q.; Lee, F. C. *IEEE T Power Electr.* 29, 2453−2461(2014).

6. Pearton, S. J.; Ren, F.; Zhang, A. P.; Dang, G.; Cao, X. A.; Lee, K. P.; Cho, H.; Gila, B. P.; Johnson, J. W.; Monier, C.; Abernathy, C. R.; Han, J.; Baca, A. G.; Chyi, J.-I.; Lee, C.-M.; Nee, T.-E.; Chuo, C.-C.; Chu, S. N. G. *Mater. Sci. Eng., B*. 82, 227−231(2001).

7. Liu, L.; Edgar, J. H. *Mater. Sci. Eng., R.* 37, 61−127(2002).

8. Cheng, Z. J.; Chen, X. Y.; San, H. S.; Feng, Z. H.; Liu, B. *J. Micromech. Microeng.* 22, 074011−074016 (2012).

9. Margalith, T.; Buchinsky, O.; Cohen, D. A.; Abare, A. C.; Hansen, M.; DenBaars, S. P.; Coldren, L. A. *Appl. Phys. Lett.* 74, 3930−3932 (1999).

10. Krost, A.; Dadgar, A. *Mater. Sci. Eng.*, B. 93, 77−84 (2002).

11. Yan, Z.; Liu, G.; Khan, J. M.; Balandin, A. A. *Nat. Commun.* 3, 827-XXX (2012).

12. Mashiko, H.; Oguri, K.; Yamaguchi, T.; Suda, A.; Gotoh, H. *Nat. Phys.*12, 741−745(2016).

13. Meneghini, M.; Trevisanello, L. R.; Meneghesso, G.; Zanoni, E. *IEEE T Device Mater. Re.* 8, 323−331(2008).

14. Chung, K.; Lee, C.; Yi, G. *Science.* 330, 655−657(2010).

15. Davis, R. F. *Proc. IEEE.* 79, 702−712 (1991).

16. Denbaars, S. P. *Proc. IEEE*. 1997, 85, 1740−1749 (1997).

17. Gupta, C.; Lund, C.; Chan, S. H.; Agarwal, A.; Liu, J.; Enatsu, Y.; Mishra, U. K. *IEEE Electron Device Lett.* 38, 353−355(2017).

18. Tanaka, R.; Takashima, S.; Ueno, K.; Matsuyama, H.; Edo, M.; Nakagawa, K. *Appl. Phys. Express.* 12, No. 054001(2019).

19. Takashima, S.; Ueno, K.; Matsuyama, H.; Inamoto, T.; Edo, M.; Takahashi, T.; Nakagawa, K. *Appl. Phys. Express.*10, 121004 (2017).

20. Götz, W.; Johnson, N. M.; Bour, D. P.; McCluskey, M. D.; Haller, E. E. *Appl. Phys. Lett.* 69, 3725−3727(1996).

21. Götz, W.; Johnson, N. M.; Walker, J.; Bour, D. P.; Street, R. A. *Appl. Phys. Lett.* 68, 667−669 (1996).

22. Nakamura, S.; Iwasa, N.; Senoh, M. S. M.; Mukai, T. M. T. *Jpn. J. Appl. Phys.* 1992, 31, 1258(1992).

23. Isomura, N.; Kimoto, Y. *J. Synchrotron Radiat.* 28, 1114−1118 (2021).

24. Bennett, S. E.; Ulfig, R. M.; Clifton, P. H.; Kappers, M. J.; Barnard, J. S.; Humphreys, C. J.; Oliver, R. A. *Ultramicroscopy.* 111, 207−211(2011).

25. Hautakangas, S.; Oila, J.; Alatalo, M.; Saarinen, K.; Liszkay, L.; Seghier, D.; Gislason, H. P. *Phys. Rev. Lett.* 90, 137402 (2003).

26. Romano, L. T.; Kneissl, M.; Northrup, J. E.; Van de Walle, C. G.; Treat, D. W. *Appl. Phys. Lett.* 79, 2734−2736 (2001).

27. Thompson, K.; Bunton, J. H.; Kelly, T. F.; Larson, D. J. *J Vac Sci Technol B.24*, 421-427 (2006).

28. Thompson, K.; Booske, J. H.; Larson, D. J.; Kelly, T. F. *Appl. Phys. Lett. 87*,

052108 (2005).

29. Tang, J.; Yamashita, Y. *ACS Appl. Electron. Mater.* 3, 4618−4622 (2021).

30. Ishikawa, R.; Lupini, A. R.; Findlay, S. D.; Taniguchi, T.; Pennycook, S. J. *Nano Lett.* 14, 1903−1908 (2014).

31. Muller, D. A.; Sorsch, T.; Moccio, S.; Baumann, F. H.; Evans-Lutterodt, K.; Timp, G. *Nature*. *399*, 758-761(1999).

32. Taguchi, N.; Kitta, M.; Sakaebe, H.; Kohyama, M.; Akita, T. *Journal of Electron Spectroscopy and Related Phenomena*. *203*, 40-44 (2015).

33. Braun, A.; Huggins, F. E.; Shah, N.; Chen, Y.; Wirick, S.; Mun, S. B.; Huffman, G. P. *Carbon*, *43*, 117-124 (2005).

34. Wu, Y.; An, Z.; Duan, Y. M.; Liu, M. T.; Ouyang, X. P. *Canadian Journal of Physics*, *90*, 125-130 (2012).

35. Barton, J. J. *Phys. Rev. Lett.* 61, 1356 (1988).

36. Tsutsui, K.; Matsushita, T.; Natori, K.; Muro, T.; Morikawa, Y.; Hoshii, T.; Kinoshita,T.; et al. *Nano Lett.* 17, 7533−7538 (2017).

37. Matsushita, T.; Guo, F. Z.; Suzuki, M.; Matsui, F.; Daimon, H.; Hayashi, K. *Phys. Rev. B.* 78, 144111 (2008).

38. Matsushita, T.; Matsui, F.; Daimon, H.; Hayashi, K. *J. Electron Spectrosc. Relat. Phenom.*178, 195−220 (2010).

39. Matsushita, T.; Matsui, F.; Goto, K.; Matsumoto, T.; Daimon, H. *J. Phys. Soc. Jpn.* 82 , 114005 (2013).

40. Matsushita, T.; Matsui, F. *J. Electron Spectrosc. Relat. Phenom.* 195, 365−374 (2014).

41. Matsushita, T. *e-Journal of Surface Science and Nanotechnology*. 14, 158−160

(2016).

42. Yokoya, T.; Terashima, K.; Takeda, A.; Fukura, T.; Fujiwara, H.; Muro, T.; Matsushita, T. *Nano Lett.* 19, 5915−5919 (2019).
43. Muro, T.; Senba, Y.; Ohashi, H.; Ohkochi, T.; Matsushita, T.; Kinoshita, T.; Shin, S. *J. Synchrotron Radiat.* 28, 1631−1638 (2021).
44. Tanuma, S.; Powell, C. J.; Penn, D. R. *Surf. Interface Anal.* 20, 77− 89 (1993).
45. Kaufmann, U.; Kunzer, M.; Maier, M.; Obloh, H.; Ramakrishnan, A.; Santic, B.; Schlotter, P. *Appl. Phys. Lett.* 72, 1326-1328 (1998).
46. Salviati, G.; Armani, N.; Zanotti-Fregonara, C.; Gombia, E.; Albrecht, M.; Strunk, H. P.; Gasparotto, A. *Materials Research Society Internet Journal of Nitride Semiconductor Research*, 5, 754-760 (2000).
47. Garcia, R.; Thomas, A. C.; Ponce, F. A. *J Cryst Growth*. 310, 3131-3134 (2008).
48. Fu, Y. K.; Tun, C. J.; Kuo, C. H. *Phys. Status Solidi C*. 5, 1499−1501 (2008).
49. Thompson, A.; Attwood, D.; Gullikson, E.; Howells, M.; Kim, K. J.; Kirz, J.; Winick, H. Lawrence Berkeley National Laboratory, Uiversity of California: Berkeley, CA, 2001.
50. Zakaznova-Herzog, V. P.; Nesbitt, H. W.; Bancroft, G. M.; Tse, J. S.; Gao, X.; Skinner, W. *Phys. Rev. B*. 2005, 72, 205113(2005).
51. Williams, J. R., Píš, I., Kobata, M., Winkelmann, A., Matsushita, T., Adachi, Y., Kobayashi, K. *J. Appl. Phys. 111*, 033525(2012).
52. Wright, A. F., Seager, C. H., Myers, S. M., Koleske, D. D., Allerman, A. A. *J. Appl. Phys. 94*, 2311-2318 (2003).

Chapter 4 Atomic Structures and Chemical States of Active and Inactive Dopant Sites in Si-Doped GaN

4.1 Introduction.

GaN shows many excellent physical properties such as a wide direct bandgap of ~ 3.4 eV, radiation resistance, high breakdown voltage, and thermal stability.[1–10] GaN is often applied to high-frequency and high-efficiency optoelectronics in the visible and ultraviolet range of the light spectrum [11–14], a converter in the high-voltage region [15], high-power devices, ionizing radiation detectors, and high electron mobility transistors [16–22]. Compared to Si and SiC, GaN has many advantages for high-temperature and high-mobility devices. For instance, GaN has a bandgap that is roughly 3 times that of Si, which is applicable to the higher-temperature region. Additionally, it exhibits superior electron mobility compared to SiC [23–25].

For GaN-based devices, Si and Mg are commonly used as n-type and p-type dopants, respectively. [26–29] These dopants are mainly ascribed to the shallow dopant property. [30,31]. However, the carrier concentration is much lower than the number of dopants. [29,32–34]. According to previous studies, the carrier concentration is about one order of magnitude less than the Si concentration. [29] In spite of many studies on dopants in GaN, the chemical states and the atomic structures of dopants in GaN have not been directly clarified yet. Kumar et al. investigated atomic structures in dopants for Mg-doped GaN using scanning transmission electron microscopy and atom probe tomography.[35] Renault et al. investigated the chemical states of dopants for Mg-doped GaN using XPS.[36] Transmission electron microscopy and electron energy loss spectroscopy (TEM-EELS) can be used to detect dopant atoms with surrounding local atomic structures in real space. However, the loss spectra of TEM-EELS exhibit average information on the electronic states as

electrons pass through the samples.[37] In addition, since the loss spectra of TEM-EELS show a large background, the quantitative analysis is very difficult.[38,39] The cross sections of edge absorption on the electrons are very small.[40] Thus, high-density electrons are needed, which causes some damage to the sample.

As described above, they could not directly clarify both atomic structures and chemical states in active and inactive sites of the dopants. Thus, one requires a method that directly allows us to clarify both of chemical states and atomic structures of the active and inactive dopant states in GaN. In addition, to gain knowledge about the carrier control in metal−oxide−semiconductor field effect transistors, it is crucial to clarify the atomic structures and chemical states of the active and inactive dopant sites in GaN.

Recently our group performed chemical state discriminated XANES and successfully clarified the atomic structures and the electronic states of the interface atoms at SiO_2/4H-SiC (0001) structures in with the SiO_2/4H-SiC (0001) structures were prepared by different oxidation methods.[41] In this chapter, this chemical state discriminated XANES is applied to Si dopants in GaN. Using this method, the atomic structures, and chemical states of active and inactive Si dopants sites in GaN would be directly clarified.

In this chapter, the atomic structures and chemical states of active and inactive Si-dopant sites in GaN were investigated.

4.2 Experimental.

4.2.1 Sample preparation

The Si-doped GaN was prepared by the HVPE method (doped layer with 0.1μm thickness) on free-standing GaN (0001) substrates (> 10^8 Ω cm) with a 1 μm thick epitaxial layer. Cl (impurity) was not detected by SIMS (below the detection limit of 10^{16} cm^{-3}). X-ray diffraction rocking curves of (002) and (102) are less than 100 arcsec, respectively. The surface roughness of GaN is less than 0.3 nm.

4.2.2 Secondary-ion mass spectrometry (SIMS).

SIMS measurements were performed to analyze the Si dopants concentration as a function of depth. PHI-ADEPT1010 was used for SIMS measurements. Cs-positive ions with 3 keV were employed as the ion source. The elements concentration conversion is based on sensitivity in GaN. Charge compensation was not used during the measurements.

4.2.3 Hall effect measurements.

Hall effect measurements with Van der Pauw method were performed to measure the mobility and carrier concentration. Four square-shaped gold sheets with a side length of about 2 mm were deposited on the four corners of the Si-doped GaN as electrodes. The magnetic field strength was 0.48 or 0.55 Tesla.

4.2.4 Cathodoluminescence.

Cathodoluminescence (CL) was used to investigate the energy level of Si doped GaN. CL measurements were performed using a HORIBA MP32 CL system attached to a Hitachi SU6600 field-emission scanning electron microscope (FE-SEM). The accelerating voltage of 3 keV was used. CL measurements were performed at t 80K.

4.2.5 Hard X-ray PES and XPS measurements

Hard X-ray PES measurements were performed using a PHI Quantes system with the X-ray source of Cr Kα (photon energies of 5414.8 eV). The energy resolution is less than 0.9 eV.

4.2.6 Synchrotron Experiments.

AES, PES, and XANES measurements of Si-doped GaN were performed at the BL1N2 and BL6N1 in the Aichi Synchrotron Radiation Center.[39-41] For the AES measurements, the photon energy was set to 1860 eV, whereas photon energies of 2300 and 3000 eV were employed for the PES measurements. For the Si KLL, AES, and Si 1s PES measurements, PHOIBOS 150 with a high-energy model (SPECS) was used as an electron analyzer. The takeoff angle was 90° (surface normal). For the Si K-edge XANES measurements, the Auger electron yield was employed where the energy range was from 1835 to 1855 eV with the energy step of 0.2 eV. XANES measurements for the N K-edge were performed with the total electron yield method and an energy range of 360−450 eV. A clean Au sample was used to calibrate the binding energy.

4.3 Results and discussion

4.3.1 SIMS and Hall effect measurements

Figure 4.1 shows the SIMS for higher and lower Si dopant concentrations in Si-doped GaN. In the case of higher Si dopant concentration, the concentration of Si dopant is very high at the surface and then the concentration drastically decreases with depth. Because the information depth of Auger yield XANES is around 5 nm,[44] the average Si concentration within the information depth is estimated to be 2.1 x 10^{20} cm^{-3}. In the case of lower Si dopant concentration, the average Si concentration within the information depth is estimated to be 5.5 x 10^{19} cm^{-3}.

In the case of higher Si dopant concentration (2.1 x 10^{20} cm^{-3}), Hall effect measurements showed that the resistivity, mobility, and carrier concentration were 7.2 x 10^{-5} Ω.cm, 9.0 x 10^{2} cm^2 / V.s, and 9.6 x 10^{19} cm^{-3}, respectively. In the case of lower Si dopant concentration (5.5 x 10^{19} cm^{-3}), the resistivity, mobility, and carrier concentration were 4.1x 10^{-4} Ω.cm, 2.5 x 10^{3} cm^2 / V.s, and 6.2 x 10^{18} cm^{-3}, respectively. Thus, the Si dopants in both Si dopant concentrations were not fully activated.

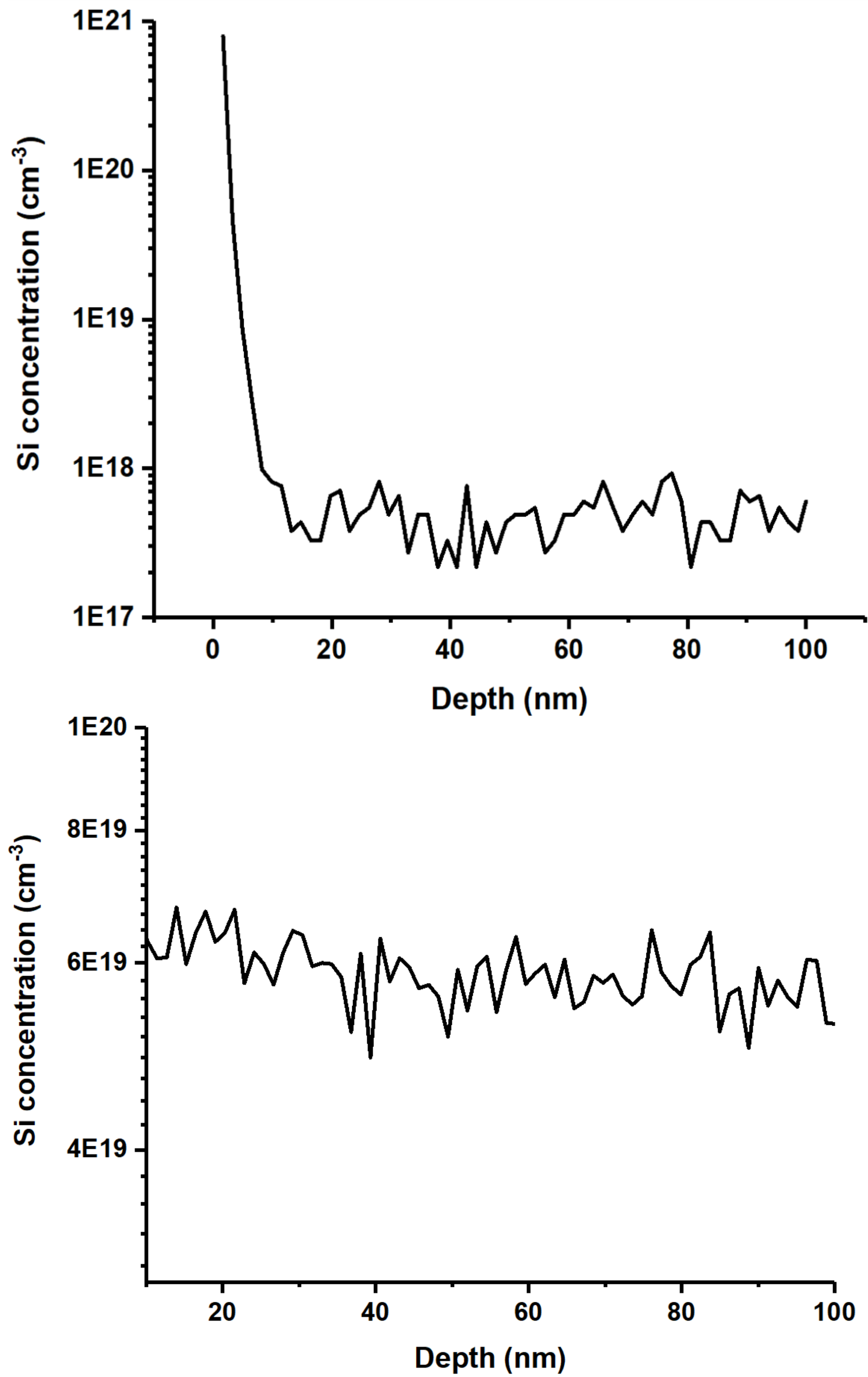

Figure. 4.1. SIMS for Si dopant in Si-doped GaN: (a) higher Si dopant concentration; (b) lower Si dopant concentration.

4.3.3 **Hard X-ray PES measurements**

Figure 4.2 (a) shows the Si 1s PES spectrum of Si-doped GaN (low concentration, $5.5 \times 10^{19} cm^{-3}$) measured with photon energies of 5414.8 eV. As can be seen, the S/N ratio is not good to analyze. Figure 4.2 (b) shows the Si 1s XPS spectrum of Si-doped GaN (high concentration, $2.1 \times 10^{20} cm^{-3}$) measured with photon energies of 3000 eV, showing that it has a sufficient S/N ratio to analyze. The hall effect measurements show active and inactive dopant sites exist in the case of Si dopant concentration, thus the high concentration of Si dopant in GaN sample was used to investigate the atomic structures and the chemical states of active and inactive Si dopant sites in GaN.

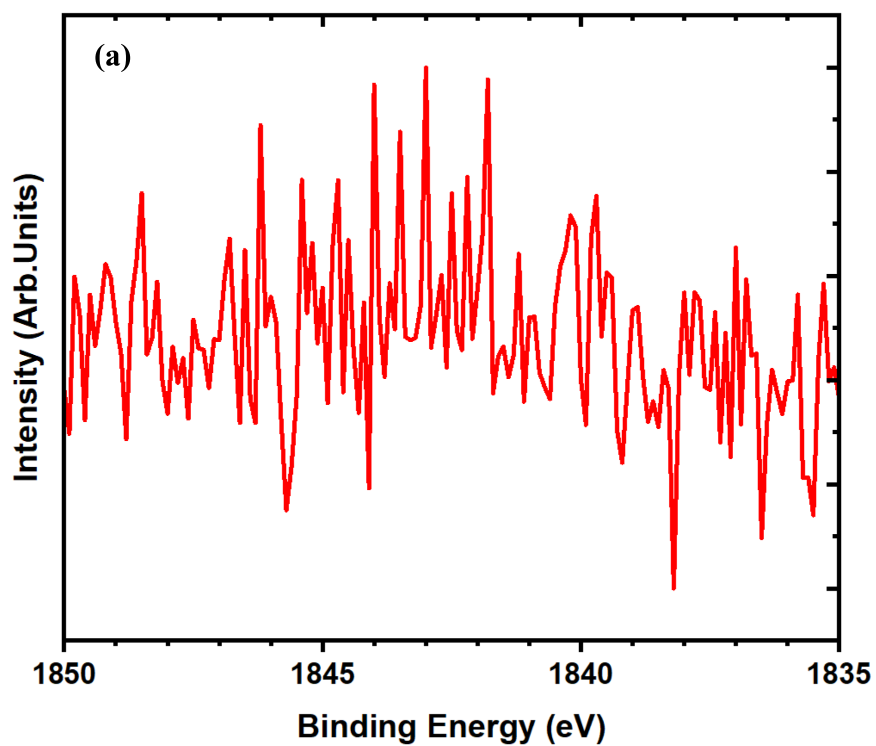

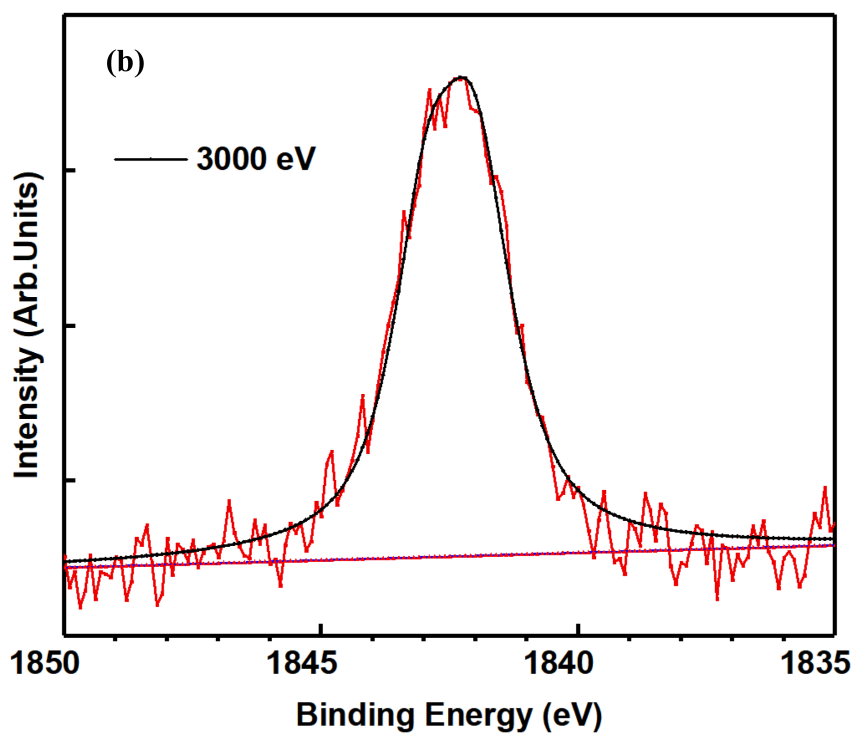

Figure. 4.2. (a)Si 1s hard x-ray PES spectrum for lower Si dopant concentration in Si-doped GaN where photon energy was 5414.8 eV;(b) Si 1s PES spectrum for higher Si dopant concentration in Si-doped GaN. The incident photon energy was 3000 eV.

4.3.2 **CL measurements**

Figure 4.3 shows SEM images and CL spectrum for Si-doped GaN (concentration of 2.1×10^{20} cm^{-3}). Uniform surface is observed form SEM images, as shown in Fig. 4.3

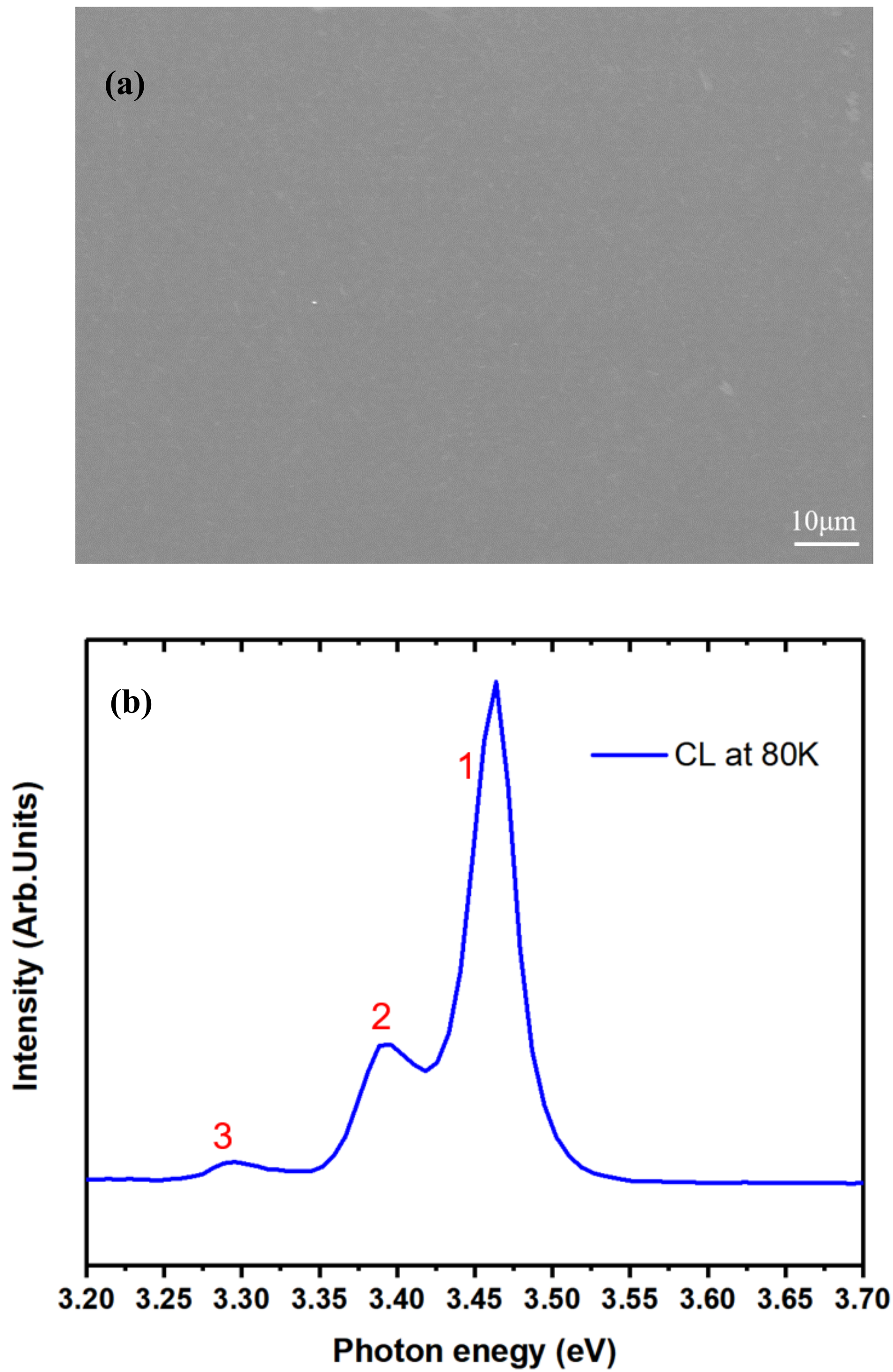

Figure. 4.3 (a) SEM images of Si doped GaN; (b) CL spectrum of Si-doped GaN at 80 K.

(a). It can be found that the strong emission (peak 1) centered at 3.46 eV is attributed to donor-bound excitons, as shown in Fig. 4.3 (b). The peaks 2 and 3 in CL spectrum are ascribed 1st, and 2nd LO-phonon replica.[45,46]

4.3.4 **AES and PES**

Figure 4.4 shows the Si KLL AES of Si-doped GaN measured with an incident photon energy of 1860 eV. The two components observed at the higher and lower kinetic energies are assigned to Si_3N_4 and SiNx (x > 1.33), respectively.[47,48] Figure 4.5 shows Si 1s PES spectra of Si-doped GaN measured with photon energies of 2300 and 3000 eV. The two peaks observed at 1842.0 and 1843.0 eV are attributed to Si_3N_4 and SiNx, respectively.[47–49] The areal intensities of Si_3N_4 and SiNx depend on the photon energies. For a photon energy of 2300 eV (surface sensitive), the areal intensity ratio (I_{Si3N4} /I_{SiNx})

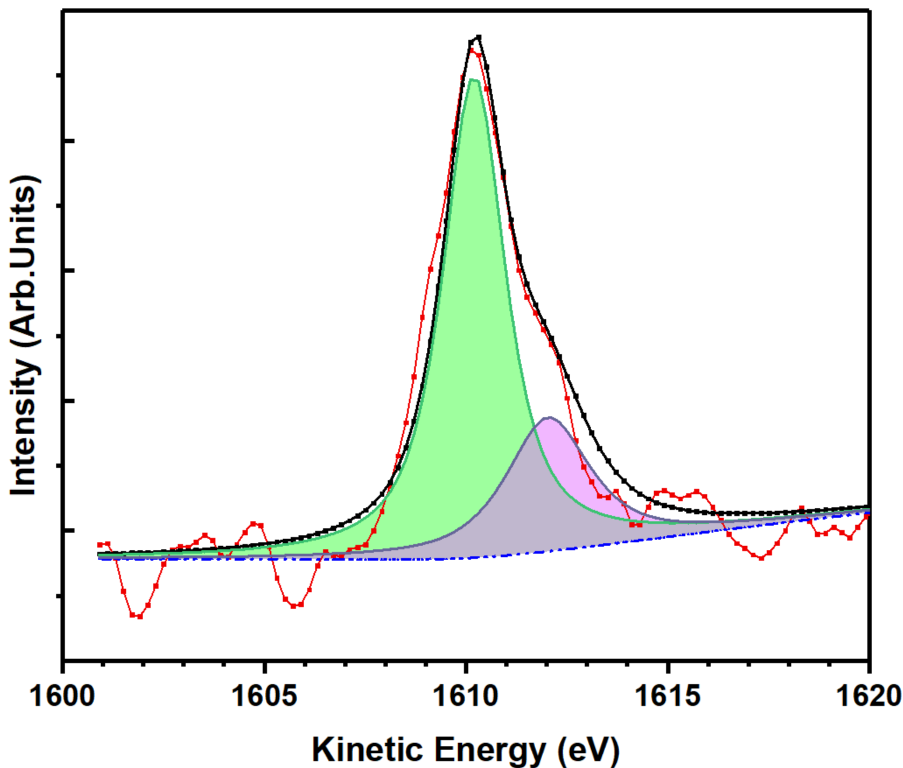

Figure. 4.4. Si KLL Auger spectrum of Si-doped GaN with a photon energy of 1860 eV.

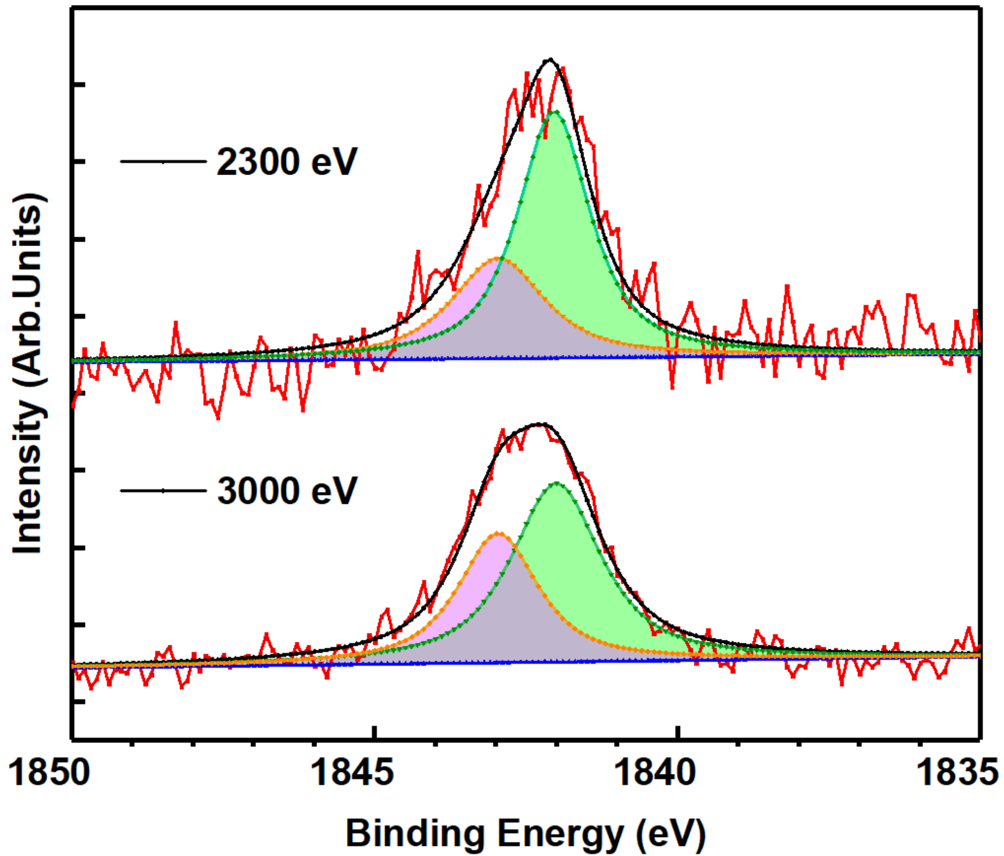

Figure 4.5. Si 1s PES spectra for Si-doped GaN with photon energies of 2300 and 3000 eV.

is 1.95 but decreases to 1.45 for a photon energy of 3000 eV (more bulk sensitive). This indicates that Si_3N_4 is predominantly formed near the surface.

Figure 4.6 shows the XANES spectra for Si_3N_4 and SiNx. The XANES was performed using the Auger electron yield (AEY) at Auger structures of 1610.1 eV (SiNx) and 1612.2 eV (Si_3N_4) (see Fig. 4.4). Since AES distinguishes the chemical states of the Si dopants in Si-doped GaN, chemical state discriminated XANES can be performed to clarify the atomic structures and the chemical states of active and inactive Si dopant sites in GaN.

The structure around 1845 eV XANES is attributed to the Si 3p unoccupied states

due to the golden selection rule of photoexcitation of the core level. [50] The spectrum of SiNx exhibits a lower onset of the edge structure while Si_3N_4 does not have one.

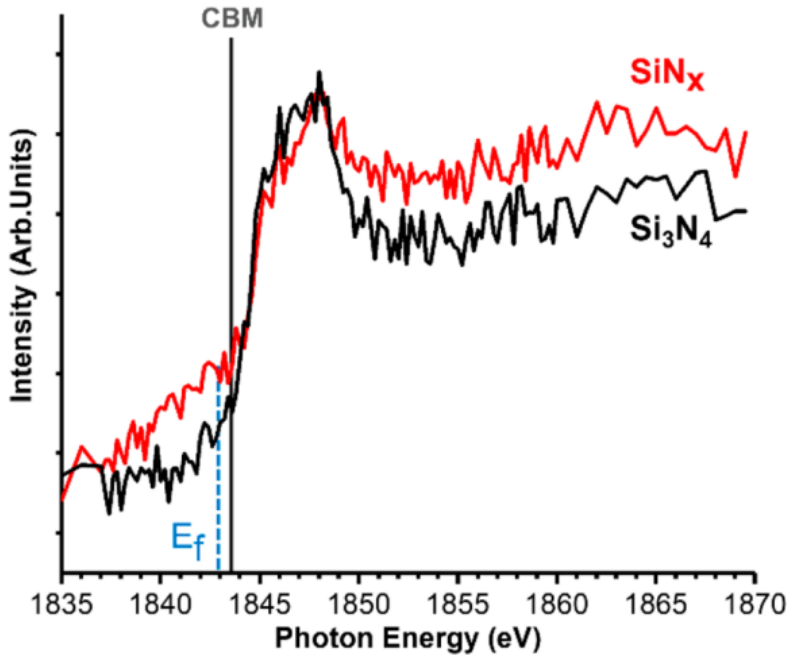

Figure 4.6. XANES spectra for Si-doped GaN. Black solid and red solid lines indicate XANES spectra recorded by AEY where Auger components are 1612.2 and 1610.1 eV, respectively.

Figure 4.7 (a) shows the N K-edge XANES spectrum for the non-doped GaN. The edge at 399.85 eV is attributed to the conduction band minimum (CBM) of GaN. Figure 4.8 (b) shows the N 1s of GaN measured at a photon energy of 800 eV. The main peak observed at 398.23 eV is originated from GaN. [49–51]

The N K-edge XANES spectrum of undoped GaN exhibits an absorption edge of 398.7 eV (Fig. 4.8 (a)), which is attributed to the N 1s to CBM transition of GaN. For the N 1s PES spectrum, the binding energy at 398.2 eV is the energy from the Fermi level (E_f).[52] Note that in photoelectron spectroscopy the binding energy of 0 eV is the Fermi level, while in XANES the absorption edge is CBM since XANES shows unoccupied states in GaN. Because the energy difference between the CBM and E_f is 0.5 eV in GaN,

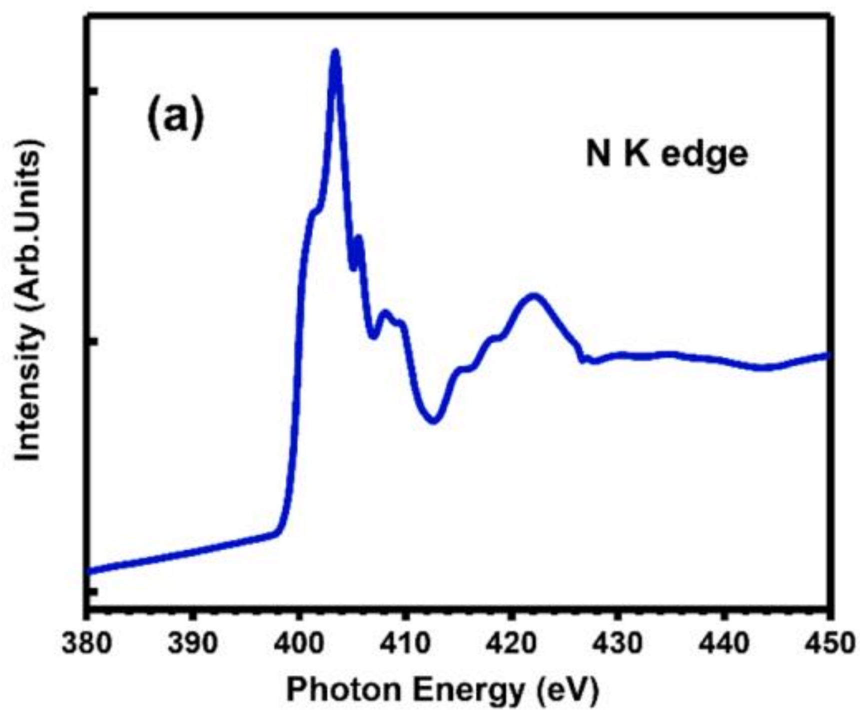

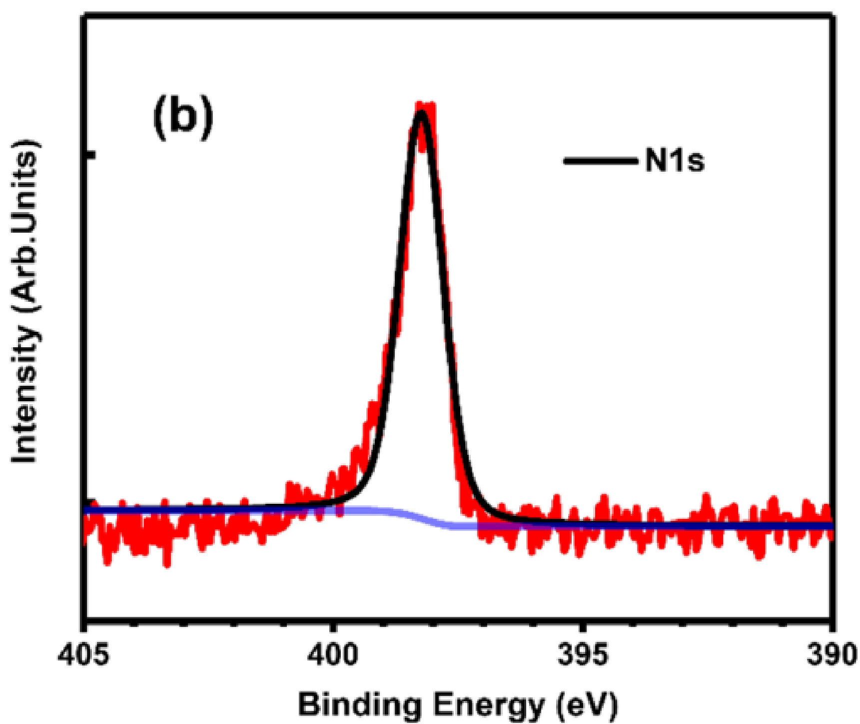

Figure 4.7. (a) N K-edge XANES spectrum for undoped GaN;(b) PES spectrum of N 1s of undoped GaN.

E_f is located 0.5 eV below the CBM. For the Si dopant, the Si 1s binding energy of SiNx at 1843 eV is the energy from E_f. Thus, the CBM of GaN is estimated to be1843.5 eV in the Si K-edge XANES spectrum. From these results, the CBM and E_f were added in Fig. 4.6. In the spectra, Si_3N_4 does not form an electronic state in the bandgap. On the other hand, SiNx shows a bandgap state. In general, active dopants have the energy levels in a bandgap. [53] Thus, SiNx may be an active dopant site in GaN.

To clarify the atomic structure of active state in the Si dopant, the simulations of XANES spectra were performed using FEFF9 (XANES simulation software).[54–56] According to the previous studies, substitutional site (Si replacing Ga) (Sub) and interstitial site (Si is located between Ga atom and N atom) (Inter) were reported as the Si dopant structures in Si-doped GaN. [32,36,57,58] Therefore, the XANES spectra for the Sub and Inter sites were simulated. Each simulation employed ~350 atoms and the final-state effect; that is, the Z + 1 approximation was used in the present simulations.[59,60]

The XANES simulations with different atoms and dopant sites are shown in Fig. 4.8. When the number of atoms is less than 200 atoms, XANES spectrum changes with the size of a cluster. However, when the number of atoms is more than 200 atoms, the XANES spectra show similar. Therefore, the cluster size having ~350 atoms was used for the XANES simulations in the present study.

Figure 4.9 shows the SiNx experimental XANES spectrum, simulated Si K-edge XANES of the Sub and Inter sites in Si doped GaN. From the simulated spectrum for Sub, the simulated XENES spectrum exhibits similar to the SiNx experimental XANES spectrum, as noted by the arrows in Fig. 4.10. By contrast, the simulated XANES spectrum for the Inter site does not explain the experimental result. Therefore, the active site for Si-doped GaN is the Sub state (the Si−N−Ga structure in the Sub state).

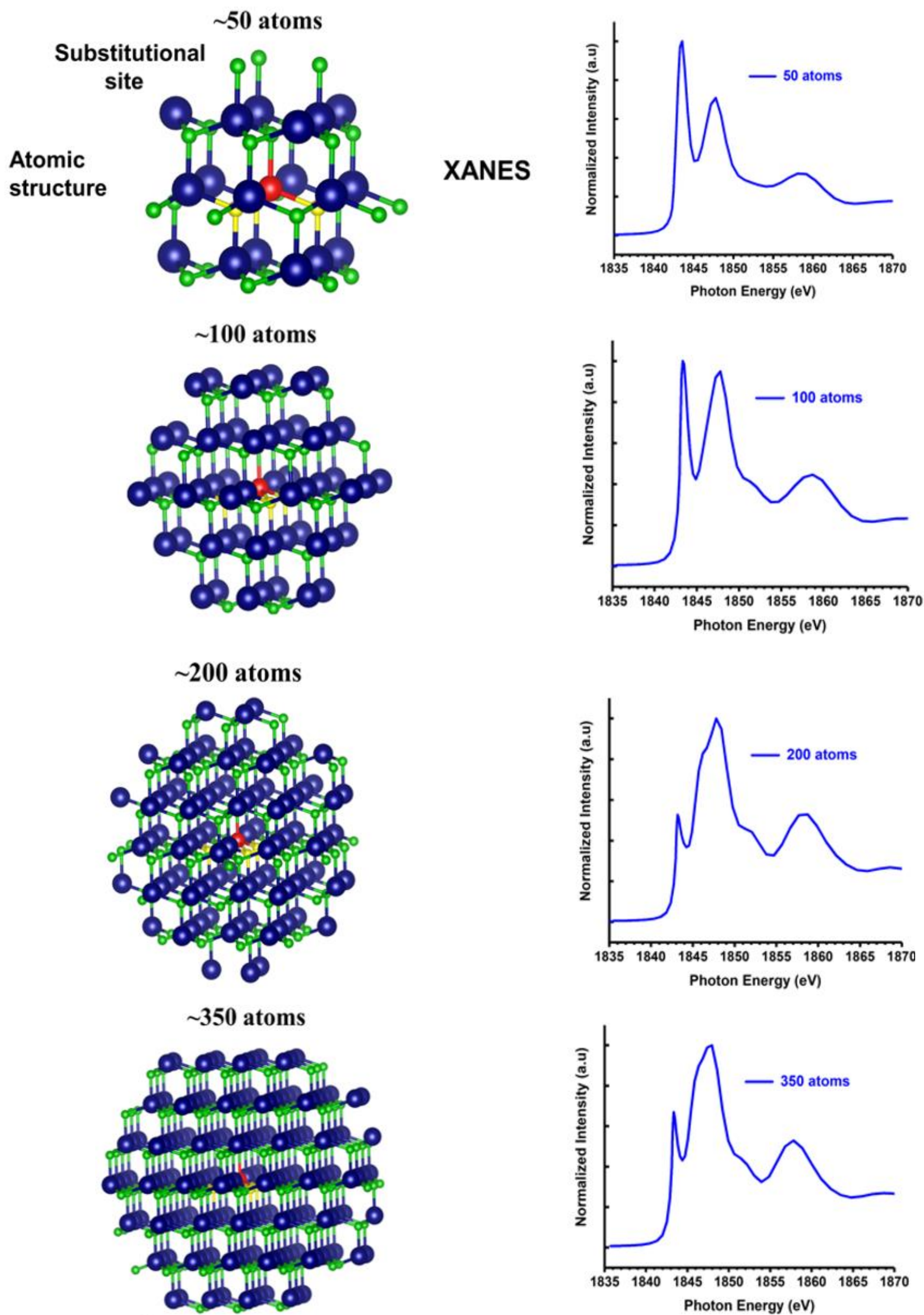

Figure 4.8. XANES simulation spectra as a function of number of atoms in a GaN cluster with one Si atom of Si substitutional (Sub) sites. In the GaN cluster, dark blue balls, light green and yellow balls, and red balls indicate Ga, N, and Si, respectively. FEFF9 was used for the simulations.

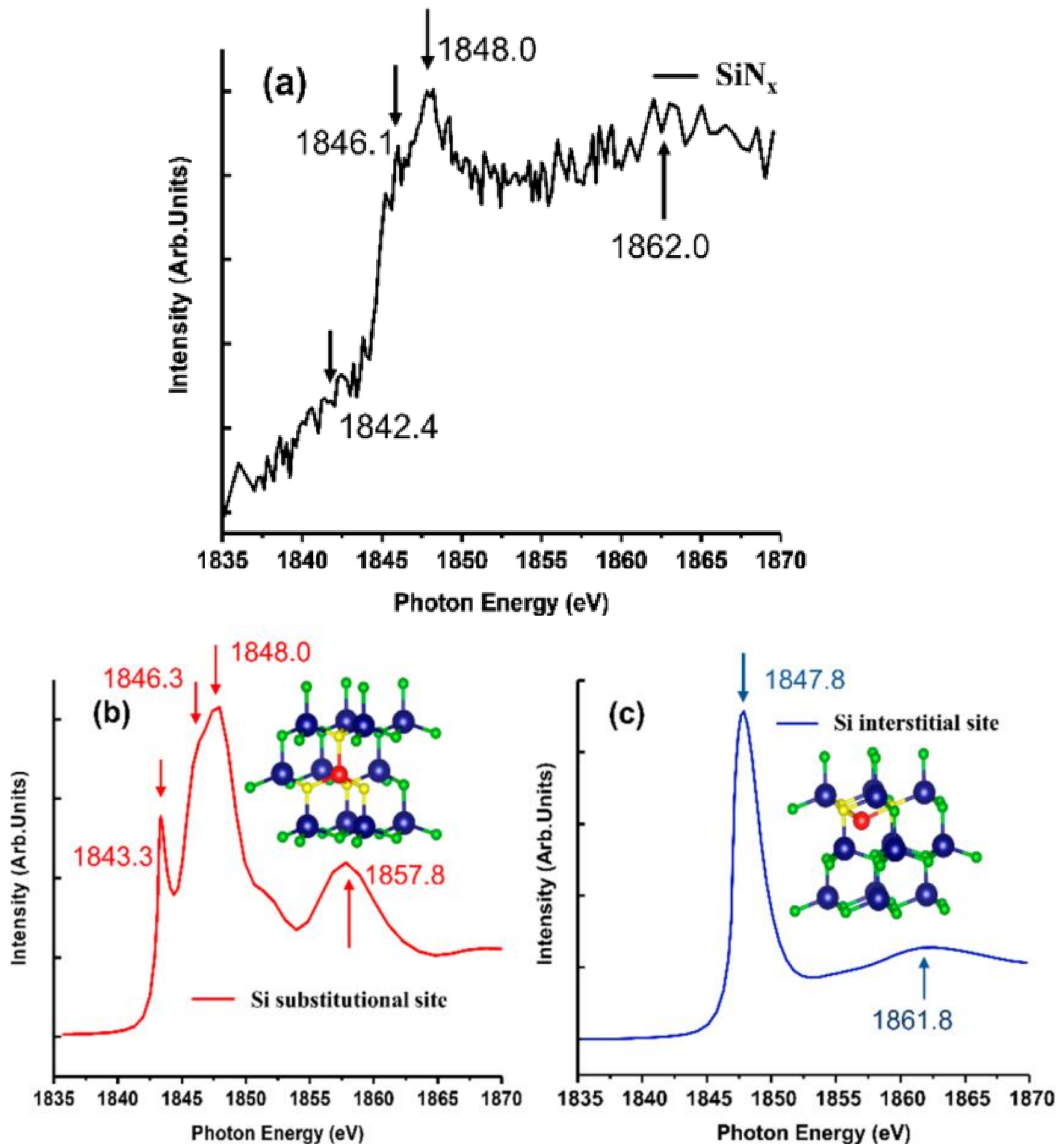

Figure 4.9 (a) Experimental XANES spectrum of the SiNx, (b) simulated XANES spectrum of the Sub site, and (c) simulated XANES spectrum of the Inter site. The inset shows each local atomic structure of Si atom in GaN. Dark blue, light green and red circles indicate Ga, N, and Si, respectively. For FEFF9 simulations, the many-body amplitude reduction factor was set to 1.0. The cluster size of Sub and Inter states is 9.5 Å, which includes ~350 atoms. Self-consistent field potentials and full multiple scattering were performed on a cluster size with a 9.5 Å radius to contain all atoms. The final state effect was employed. Angular momentum density of states is from −30 to 20 eV with a 0.1 eV step.

Next the formation of Si_3N_4 is discussed as described below. According to the previous studies,[61] Ga vacancies are formed near the surface in GaN, as shown in Fig.4.10 (a). In this situation, when Si dopant atoms migrate to the surface, the Si atom may occupy the Ga vacancy site. After that, the thermodynamically stable Si_3N_4 would be formed near the surface as shown in Fig. 4.10 (b). Once stable Si_3N_4 is formed near the surface, the stable Si_3N_4 may be present near the surface. Thus, Si_3N_4 is predominantly formed near the surface.

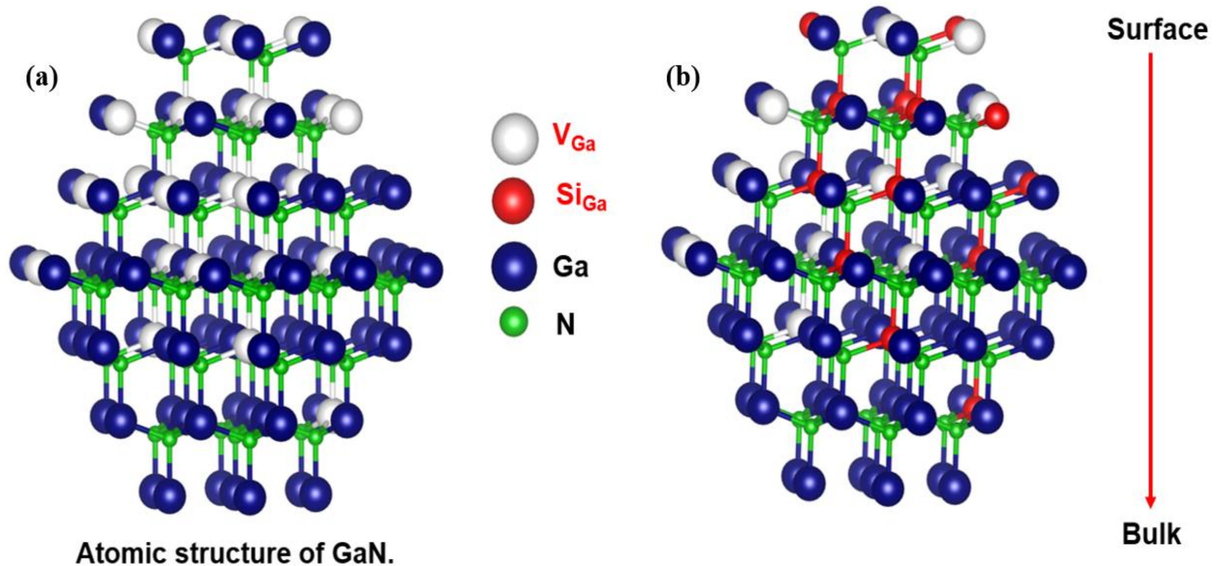

Figure 4.10. (a) Atomic structure of GaN with Ga vacancies; (b) Si_3N_4 is formed near the surface of GaN.

Then the atomic structures of Si_3N_4 of the inactive dopant site is discussed. Figure 4.11 (left in the figure) shows the structures of crystals of poly types Si_3N_4, namely trigonal α-Si_3N_4, hexagonal β-Si_3N_4, and cubic γ-Si_3N_4, respectively. Based on the structure of hexagonal β-Si_3N_4, the corresponding simulated XANES spectrum is obtained, as shown in Fig. 4.11 (right in the figure). Simulated XANES spectrum shows

a main absorption peak at ~1847 eV, and a shape resonance at~1863 eV(as indicated by the arrow in Fig.4.11(b)). Compared to the experimental results of Si_3N_4 XANES spectrum in Fig. 4.11(d), the experimental Si_3N_4 XANES spectrum exhibits similar result to the simulated β-Si_3N_4 XANES spectrum. Therefore, the atomic structure of the inactive state may be β-Si_3N_4. In Si-doped GaN, the Ga vacancies would be formed near the surface. During the doping process into GaN, Si dopants would occupy these vacancies and bond with N atoms to form Si_3N_4, stable β-GaN.

Based on these described above, the atomic structures of active and inactive sites are shown in Fig. 4.12. For the active dopant site, the atomic structure is Si in substitution site in GaN. In the case of inactive dopant site, the atomic structure is β- Si_3N_4.

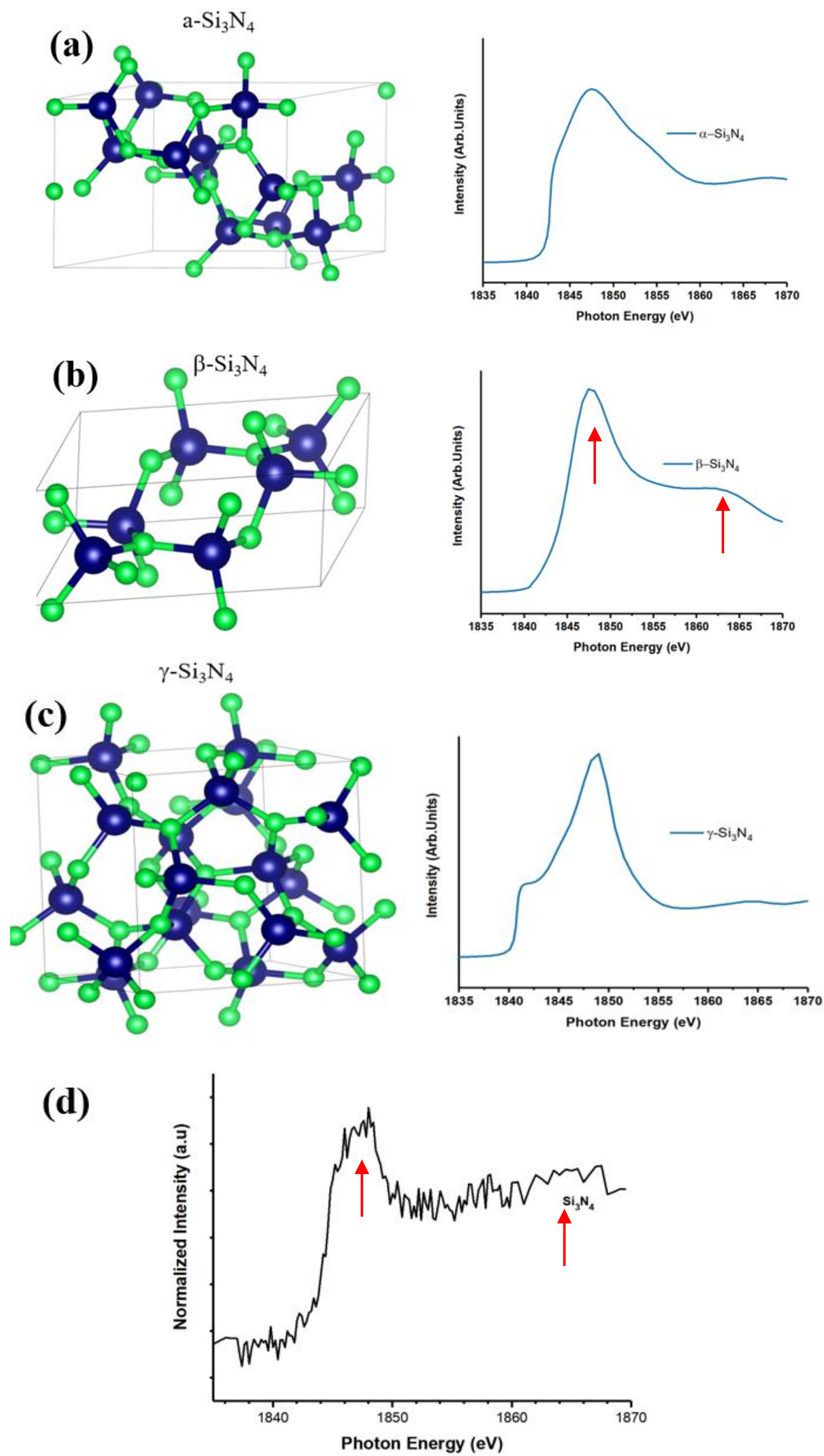

Figure 4.11: Crystal structures and corresponding simulated XANES spectrum of (a) trigonal α-Si_3N_4, (b) hexagonal β- Si_3N_4, and (c) cubic γ- Si_3N_4;(d) experimental of Si_3N_4 XANES spectrum.

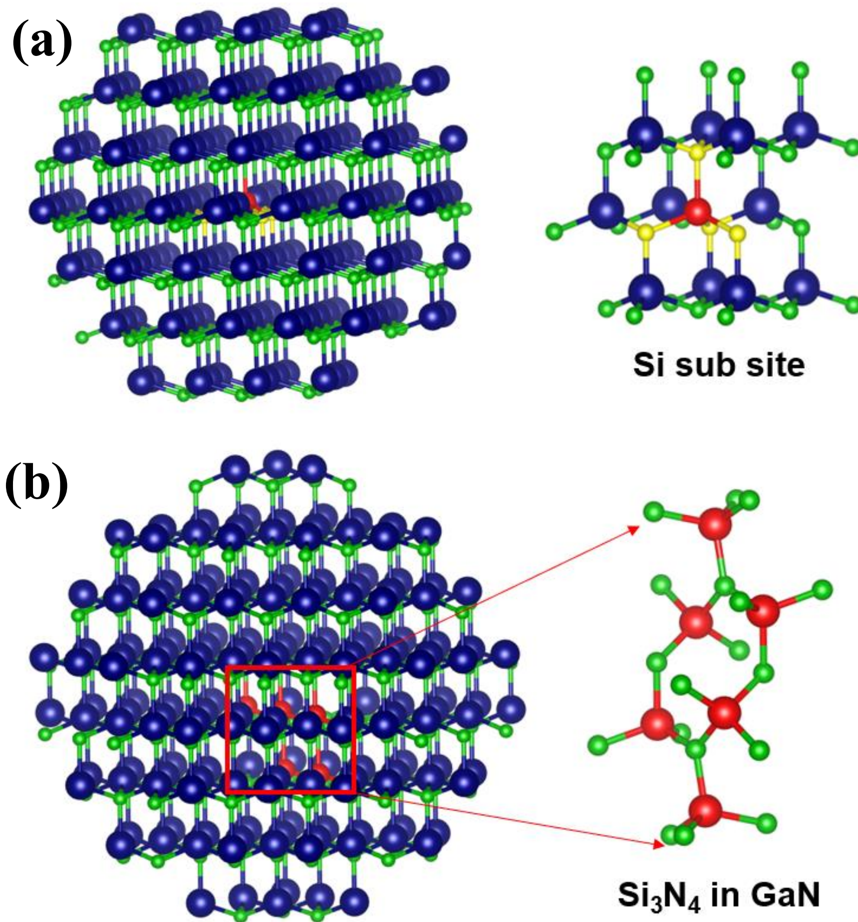

Figure 4.12: (a) the atomic structure for the active dopant state of Si doped in GaN structure (left), the local structure of active dopant state (right); (b) the atomic structure for the inactive dopant state of Si doped in GaN structure (β-Si_3N_4) (left), the local structure of inactive state (right).

4.4 Conclusion

XANES and synchrotron-based AES and PES were employed to investigate the atomic structures and chemical states for Si dopant sites in GaN. Two dopant states were observed. Si_3N_4 can acted as an inactive dopant because it did not have an electronic state in the bandgap. By contrast, SiNx should be the active dopant site as it forms an electronic state in the GaN bandgap. To clarify the atomic structure of the active site for the Si dopant, the XANES spectra were simulated using the FEFF9. The simulated XANES spectrum of Sub site in Si-doped GaN represented the experimental one, suggesting that the active dopant site in Si-doped GaN was Si in Sub site. In the case of the inactive dopant site, the atomic structure is β-Si_3N_4. Thus, the atomic structures and chemical states of active and inactive dopant sites were directly clarified using chemical discriminated AES yield XANES.

Based on the present study, it would be possible to increase the concentration of the active dopant site n by properly adjusting the Ga pressure near the surface. This inhibits the formation of the inactive dopant site, which would increase carrier concentration.

I present the approach using chemical discriminated AES yield XANES which successfully observes the atomic structure and the chemical states of active and inactive dopants in GaN. The present approach is therefore widely applicable to the active and inactive dopant sites of various systems of semiconductors and will be indispensable for evaluating the atomic scale properties of dopants of semiconductors and designing new semiconductor materials.

4.5 References

1. Pankove, J. I. *Mater. Sci. Eng., B*. 61, 305−309 (1999).
2. Morkoc, H.; Strite, S.; Gao, G. B.; Lin, M. E.; Sverdlov, B.; Burns, M. *J. Appl. Phys.*76, 1363−1398 (1994).
3. Manna, S.; Ashok, V. D.; De, S. K. *ACS Appl. Mater. Interfaces*. 2, 3539−3543 (2010).
4. Mohammad, S. N.; Salvador, A. A.; Morkoc, H. *Proc. IEEE*. 83, 1306−1355 (1995).
5. Leszczynski, M.; Teisseyre, H.; Suski, T.; Grzegory, I.; Bockowski, M.; Jun, J.; Porowski, S.; Pakula, K.; Baranowski, J. M.; Foxon, C. T.; Cheng, T. S. *Appl. Phys. Lett.* 69, 73−75 (1996).
6. Pearton, S. J.; Ren, F.; Zhang, A. P.; Dang, G.; Cao, X. A.; Lee, K. P.; Cho, H.; Gila, B. P.; Johnson, J. W.; Monier, C.; Abernathy, C. R.; Han, J.; Baca, A. G.; Chyi, J.-I.; Lee, C.-M.; Nee, T.-E.; Chuo, C.-C.; Chu, S. N. G. *Mater. Sci. Eng., B*. 82, 227−231(2001).
7. Liu, L.; Edgar, J. H. *Mater. Sci. Eng., R.* 37, 61−127(2002).
8. Cheng, Z. J.; Chen, X. Y.; San, H. S.; Feng, Z. H.; Liu, B. *J. Micromech. Microeng.* 22, 074011−074016 (2012).
9. Arakawa, Y.; Ueno, K.; Imabeppu, H.; Kobayashi, A.; Ohta, J.; Fujioka, H. *Appl. Phys. Lett.* 110, 042103 (2017).
10. Margalith, T.; Buchinsky, O.; Cohen, D. A.; Abare, A. C.; Hansen, M.; DenBaars, S. P.; Coldren, L. A. *Appl. Phys. Lett.* 74, 3930−3932 (1999).
11. Davis, R. F. *Proc. IEEE.* 79, 702−712 (1991).
12. Denbaars, S. P. *Proc. IEEE.* 85, 1740−1749 (1997).
13. Chung, K.; Lee, C.; Yi, G. *Science.* 2010, 330, 655−657 (2010).
14. Ye, Z.; Lei, Y.; Liao, Z.; Pilawa-Podgurski, R. C. *IEEE 18th Workshop Control*

Modeling Power Electron. (COMPEL). pp 1−7 (2017).

15. Meneghini, M.; Trevisanello, L. R.; Meneghesso, G.; Zanoni, E. *IEEE Trans. Device Mater. Reliab.* 8, 323−331 (2008).
16. Pant, R.; Shetty, A.; Chandan, G.; Roul, B.; Nanda, K. K.; Krupanidhi, S. B. *ACS Appl. Mater. Interfaces*.10, 16918− 16923 (2018).
17. Journot, T.; Bouchiat, V.; Gayral, B.; Dijon, J.; Hyot, B. *ACS Appl. Mater. Interfaces* 10, 18857− 18862 (2018).
18. Reddeppa, M.; Nam, D. J.; Bak, N. H.; Pasupuleti, K. S.; Woo, H.; Kim, S. G.; Oh, J. E.; Kim, M. D. *ACS Appl. Mater. Interfaces.*13, 30146−30154 (2021).
19. Nakamura, S.; Mukai, T.; Senoh, M. *Appl. Phys. Lett.* 64, 1687−1689 (1994).
20. Trivellin, N.; Meneghini, M.; Zanoni, E.; Orita, K.; Yuri, M.; Meneghesso, G. *IEEE Int. Reliab. Phys. Symp. Proc.* 8, 1−6 (2010).
21. del Alamo, J. A.; Joh, J. *Microelectron. Reliab.* 49, 1200−1206 (2009).
22. Nord, J.; Nordlund, K.; Keinonen, J.; Albe, K. *Nucl. Instrum. Methods Phys. Res., Sect. B.* 202, 93−99 (2003).
23. Flack, T. J.; Pushpakaran, B. N.; Bayne, S. B. GaN technology for power electronic applications: A review. J. Electron. Mater. 2016, 45, 2673−2682.
24. Wang, J.; Mulligan, P.; Brillson, L.; Cao, L. R. *Appl. Phys. Rev.* 2, 031102 (2015).
25. Schubert, E. F.; Goepfert, I. D.; Grieshaber, W.; Redwing, J. M. *Appl. Phys. Lett.* 71, 921− 923 (1997).
26. Nakamura, S.; Fasol, G. *Springer: Heidelberg*, (1997).
27. McCarthy, L. S.; Kozodoy, P.; Rodwell, M. J. W.; DenBaars, S. P.; Mishra, U. K. *IEEE Electron Device Lett.* 20(6), 277−279 (1999).
28. Romano, L. T.; Kneissl, M.; Northrup, J. E.; Van de Walle, C. G.; Treat, D. W. *Appl.*

Phys. Lett. 79, 2734−2736 (2001).

29. Iwinska, M.; Sochacki, T.; Amilusik, M.; Kempisty, P.; Lucznik, B.; Fijalkowski, M.; Litwin-Staszewska, E.; Smalc-Koziorowska, J.; Khapuridze, A.; Staszczak, G.; Grzegory, I.; Bockowski, M. J. Cryst. Growth, 456, 91−96 (2016).
30. Halidou, I.; Benzarti, Z.; Chine, Z.; Boufaden, T.; El Jani, B. Microelectron. J, 32, 137−142 (2001).
31. Irokawa, Y.; Fujishima, O.; Kachi, T.; Nakano, Y. J. Appl. Phys, 97, 083505 (2005).
32. Wagner, C. D.; Passoja, D. E.; Hillery, H. F.; Kinisky, T. G.; Six, H. A.; Jansen, W. T.; Taylor, J. A. J. Vac. Sci. Technol, 21, 933−944 (1982).
33. Fellows, J. A.; Yeo, Y. K.; Hengehold, R. L.; Johnstone, D. K. Appl. Phys. Lett, 80, 1930−1932 (2002).
34. Ueno, K.; Kobayashi, A.; Fujioka, H. AIP Adv, 9, 075123 (2019).
35. Kumar, A.; Uzuhashi, J.; Ohkubo, T.; Tanaka, R.; Takashima, S.; Edo, M.; Hono, K. J. Appl. Phys, 126, 235704 (2019).
36. Renault, O.; Morin, J.; Tchoulfian, P.; Chevalier, N.; Feyer, V.; Pernot, J.; Schneider, C. M. Ultramicroscopy, 159, 476− 481 (2015).
37. Muller, D. A., Sorsch, T., Moccio, S., Baumann, F. H., Evans-Lutterodt, K., & Timp, G. *Nature*. *399*(6738), 758-761(1999).
38. Taguchi, N., Kitta, M., Sakaebe, H., Kohyama, M., & Akita, T. *Journal of Electron Spectroscopy and Related Phenomena*. *203*, 40-44 (2015).
39. Braun, A., Huggins, F. E., Shah, N., Chen, Y., Wirick, S., Mun, S. B., & Huffman, G. P. *Carbon*, *43*(1), 117-124 (2005).
40. Wu, Y., An, Z., Duan, Y. M., Liu, M. T., & Ouyang, X. P. *Canadian Journal of Physics*, *90*(2), 125-130 (2012).

41. Yamashita, Y., Nara, J., Indari, E. D., Yamasaki, T., Ohno, T., & Hasunuma, R. *J appl phys. 131*(21), 215303 (2022).

42. Handbook of Semiconductor Wafer Cleaning Technology: Science, Technology and Applications; Kern, W., Ed.; Noyes Publications: Park Ridge, NJ, (1993).

43. Kern, W.; Puotinen, D. A. RCA Rev. 1970, 31, 187−206 (1970).

44. Liu, J., Hembree, G. G., Spinnler, G. E., & Venables, J. A. *Ultramicroscopy*. *52*(3-4), 369-376 (1993).

45. Li, S., Fündling, S., Sökmen, Ü., Merzsch, S., Neumann, R., Hinze, P., & Waag, A. *physica status solidi c*, *7*(1), 84-87(2010).

46. Dıaz-Guerra, C., Piqueras, J., Castaldini, A., Cavallini, A., & Polenta, L. *J appl phys*. *94*(4), 2341-2346 (2003).

47. Dupuie, J. L.; Gulari, E.; Terry, F. *J. Electrochem. Soc*. 139, 1151 (1992).

48. Chourasia, A. R.; Hood, S. J.; Chopra, D. R. *J. Vac. Sci. Technol., A*. 14, 699−703 (1996).

49. Naumkin, A. V.; Kraut-Vass, A.; Gaarestroom, S. W.; Powell, C. J. NIST X-ray Photoelectron Spectroscopy Database 20, ver. 4.1; U.S. Department of Commerce.

50. Rehr, J. J.; Ankudinov, A. L. Coord. Chem. Rev, 249, 131−140 (2005).

51. Yang, Y. G.; Ma, H. L.; Xue, C. S.; Hao, X. T.; Zhuang, H. Z.; Ma, J. Phys. B, 325, 230−234 (2003).

52. Kahn, A. Mater. Horiz, 3, 7−10 (2016).

53. Sze, S. M. Physics of Semiconductor Devices, 2nd ed.; John Wiley & Sons: 1981.

54. Rehr, J. J.; Kas, J. J.; Vila, F. D.; Prange, M. P.; Jorissen, K. Phys. Chem. Chem. Phys, 12, 5503−5513 (2010).

55. Rehr, J. J.; Kas, J. J.; Prange, M. P.; Sorini, A. P.; Takimoto, Y.; Vila, F. C. R. Phys,

10, 548−559 (2009).

56. Rehr, J. J.; Albers, R. C. Rev. Mod. Phys, 72, 621−654 (2001).

57. Tsai, Y. C.; Bayram, C. Comput. Mater. Sci, 190, 110283 (2021).

58. Zakharov, D. N.; Liliental-Weber, Z.; Gao, Y.; Hu, E, 35, 1543-1546 (2006).

59. Johansson, B.; Martensson, N. Phys. Rev. B: Condens. Matter Mater. Phys. 1980, 21, 4427- 4457 (1980).

60. Nilsson, A. J. Electron Spectrosc. Relat. Phenom, 126, 3−42 (2002).

61. Oila, J., Kivioja, J., Ranki, V., Saarinen, K., Look, D. C., Molnar, R. J., & Han, J. Y. *Appl phys lett*, 82, 3433-3435(2003).

Chapter 5 Conclusions

5.1 Conclusions

In this doctoral thesis, the atomic structures and chemical states of the dopants in Mg/Si-doped GaN were investigated. For the Mg-doped GaN, the chemical states were evaluated by Mg-KLL AES, PES, and PEH. Mg-KLL AES and PES revealed that two components existed in Mg-doped GaN; The active dopant site is attributed to Mg in the substitution site in GaN. The other is an inactive dopant site where it is originated from a disordered structure, an amorphous structure, defects, and/or a Mg_{Ga}−H complex in the Mg-doped GaN.

For Si-doped GaN, AES, PES, and XANES were used to clarify the atomic structure and the chemical states of the active and the inactive dopant sites. From AES and PES, two chemical states existed; one is Si_3N_4 and the other is SiN_x(x >1.33). From the XANES and the XANES simulations, SiN_x should be an active state where the atomic structure is due to Si in the substitution site in GaN (Si replaces Ga in GaN). In addition, from depth distribution analysis based on PES, the inactive site, Si_3N_4, is predominantly formed near the surface.

The methods mentioned above clarified the atomic structures and the chemical states of the active and the inactive states for dopants in GaN. The present approach is therefore widely applicable to the active and inactive dopant sites of various systems of semiconductors and will be indispensable for evaluating the atomic scale properties of dopants of semiconductor and designing new semiconductor materials.

5.2 Outlook.

In the present methods used in the doctor course study, the atomic structures and the chemical states of the active and the inactive dopant states of GaN were able to be clarified. Thus, one has a strategy that vanishes or reduces the inactive sites of dopants. For examples, in the case of Si-doped GaN, Si_3N_4 is predominantly formed near the surface because the formation driving force should be Ga vacancies near the surface. Therefore, when preparing the surface, gas pressure of the Ga source should be increased to reduce the Ga vacancies. In this case, the amounts of the inactive sites, Si_3N_4, may be reduced. In the case of Mg-doped GaN, after annealing at 800 °C, the amount of inactive dopant sites was reduced. The amount of inactive dopant may be further reduced by optimizing the temperature and the annealing time. Therefore, the results in the present doctor course study will help to improve the doping efficiency and performance of doped GaN in the future.

Supplementary information.

S.1 Aichi Synchrotron Radiation Center

The electron storage ring in Aichi Synchrotron Radiation Center has electron energy of 1.2 GeV, and a current of 300 mA. It has a circumference of 72 m and currently has 10 beamlines in operation. [1,2]

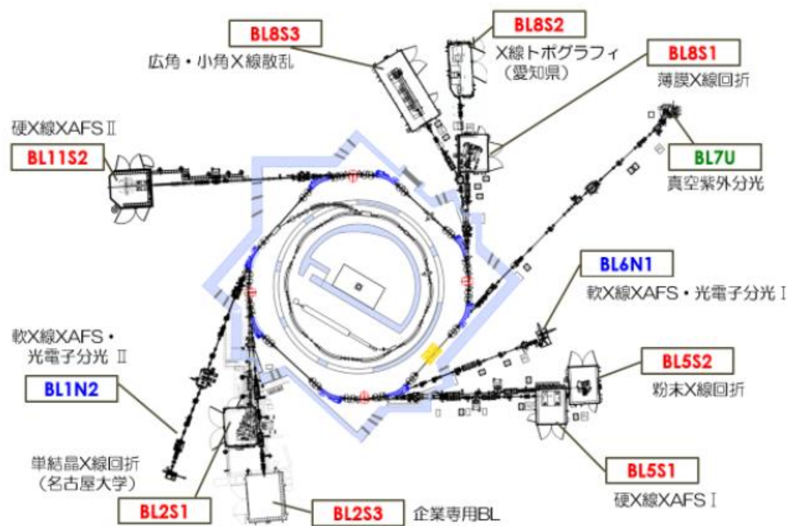

Figure S1: Layout of beamlines in Aichi Synchrotron Radiation Center.[1]

Figure S2: Photos of apparatus at BL1N2 (left) and BL6N1(right).

In the present study, beamlines of the BL1N2 and BL6N1 were used to perform AES, PES, and XANES.

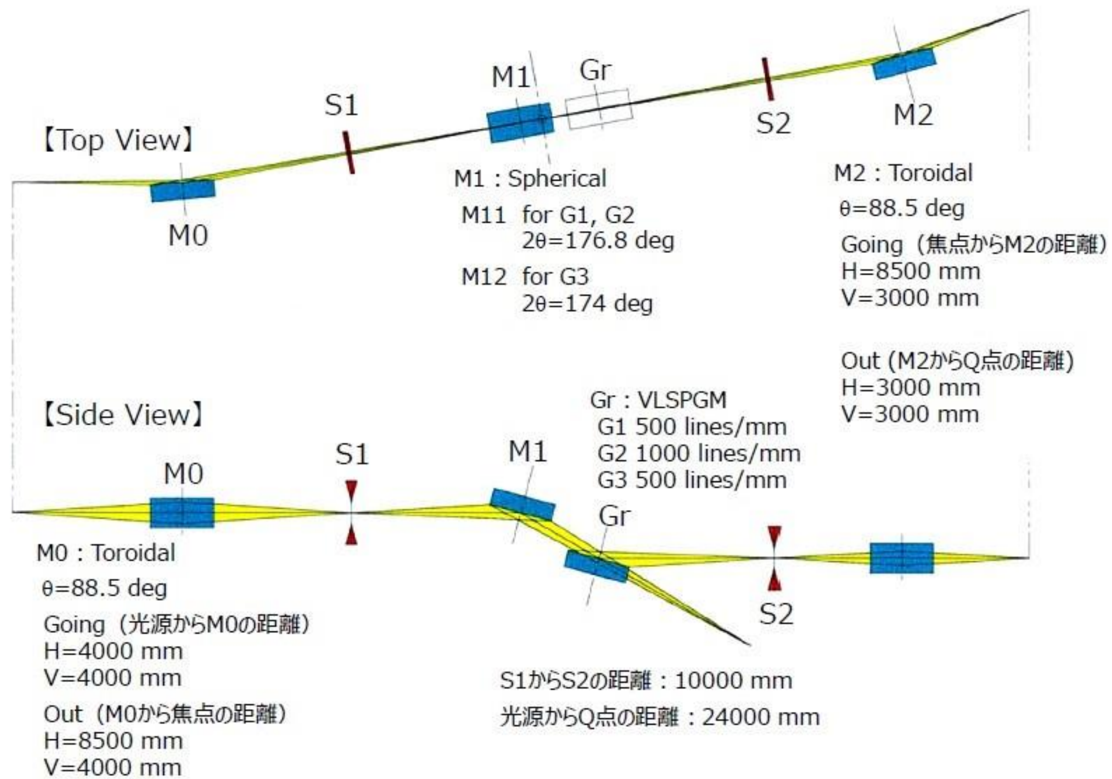

Figure S3. Beamline layout of BL1N2.[3]

S.2 Super photon ring 8 GeV (SPring-8)

SPring-8 is one of the largest synchrotron radiation facilities in the world. The electron energy is 8 GeV. The brightness of the synchrotron radiation at SPring-8 shows 1 billion higher than the sun. The circumference is 1436 m and currently 62 beamlines are in operation. [4] Beamline of the BL25SU in SPring-8 was used to perform PEH experiments in the present study.

Figure S4: SPring-8 facility.[5]

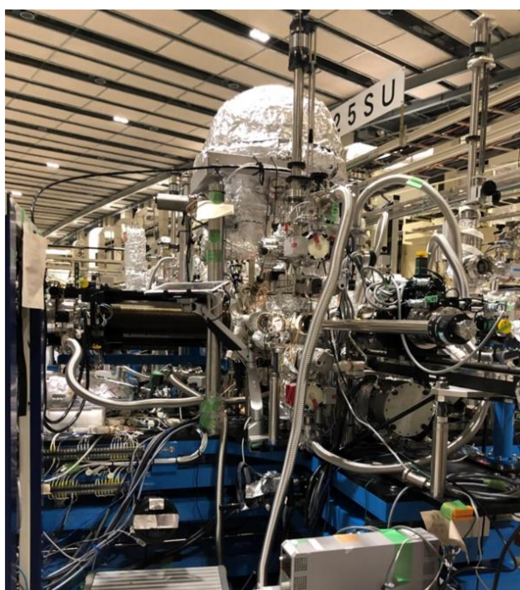

Figure S5: Photo apparatus at BL25SU.

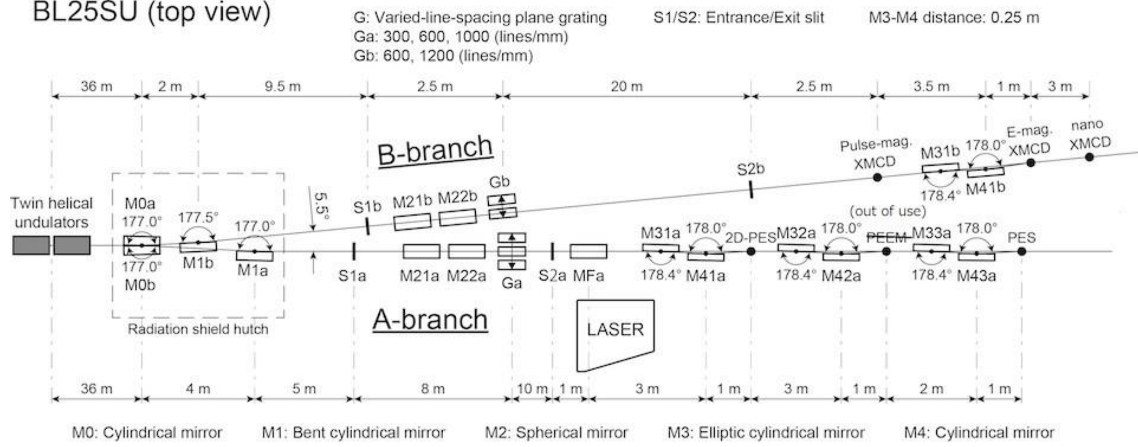

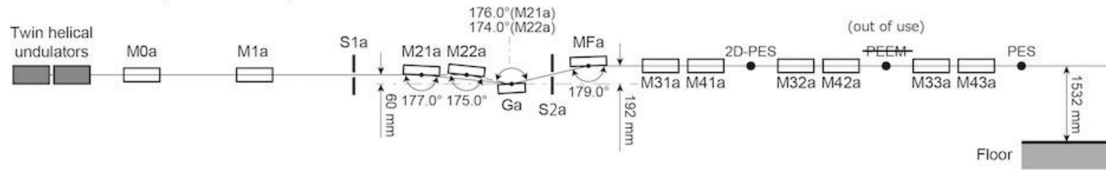

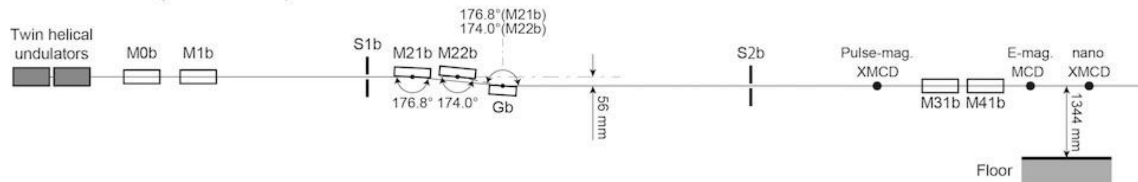

Figure S6: Beamline layout of BL25SU.[6]

S.3 References

1. https://www.aichisr.jp/about/4.html
2. Hosaka, M., Takashima, Y., Watanabe, Y., & Takeda, Y. *Kasokuki*, *13*(1), 18-24 (2016).
3. https://www.aichisr.jp/userguide/beamline_lists/BL1N2.html
4. http://www.spring8.or.jp/ja/
5. http://www.spring8.or.jp/ja/about_us/whats_sp8/
6. http://www.spring8.or.jp/wkg/BL25SU/instrument/lang-en/INS-0000000337/view

Acknowledgment

Here, I would like to express my sincere thanks to my supervisor, Professor Yoshiyuki Yamashita. He not only provided me with an excellent research platform but also his careful teaching will be of great help to my future career. His patience and professionalism continued throughout my Ph.D.

I would like to express my heartfelt thanks to Professor Tatsumi Ishihara and Professor Katsuro Hayashi (Faculty of Engineering, Kyushu University). They gave me a lot of guidance and help for my doctoral thesis as vice chairs in my dissertation defense.

I would like to thank my collaborators during my Ph.D. course; Dr. Takahiro Nagata, Dr. Jun Chen, Dr. Efi Dwi Indari, Mrs. Ayako Ogawa (National Institute for Materials Science), Professor Tomohiro Matsushita (Nara Institute of Science and Technology & Japan Synchrotron Radiation Research Institute), Mr. Soichiro Takeuchi, Mr. Masaki Tanaka, Mr. Hiroto Tomita (Nara Institute of Science and Technology), Dr. Yusuke Hashimoto (Nara Institute of Science and Technology), Dr. Takuo Ohkochi and Dr. Yoshinori Kotani (Japan Synchrotron Radiation Research Institute), Dr. Hiroshi Oji and Dr. Harue Sugiyama (Aichi Synchrotron Radiation Center). They gave me a lot of help and guidance.

I would like to express my gratitude to the secretary of our group, Mrs. Michiyo Matsushita, she is very patient and careful to help me with many things, and thanks to the members of room 531 in MANA for keeping me in a harmonious atmosphere. Also, I would like to thank Miss. Fang Xian for helping me.

Finally, thanks to my friends and family for always encouraging and helping me.